Self-Assembly of Plasmonic Nanoclusters for Optical Metafluids

Self-Assembly of Plasmonic Nanoclusters for Optical Metafluids

A dissertation presented
by

Nicholas Benjamin Schade

to
The Department of Physics

in partial fulfillment of the requirements
for the Degree of
Doctor of Philosophy
in the subject of
Physics

Harvard University
Cambridge, Massachusetts

May 2015

Dissertation Advisor: Vinothan N. Manoharan Nicholas Benjamin Schade

Self-Assembly of Plasmonic Nanoclusters for Optical Metafluids

Abstract

I discuss experimental progress towards developing a material with an isotropic, negative index of refraction at optical frequencies. The simplest way to make such a material is to create a metafluid, or a disordered collection of subwavelength, isotropic electromagnetic resonators. Small clusters of metal particles, such as tetrahedra, serve as these constituents. What is needed are methods for manufacturing these structures with high precision and in sufficient yield that their resonances are identical.

Jonathan Fan *et al.* [*Science*, 328 (5982), 1135-1138, 2010] demonstrated that colloidal self-assembly is a means of preparing electromagnetic resonators from metal nanoparticles. However, the resonances are sensitive to the separation gaps between particles. Standard synthesis routes for metal nanoparticles yield crystals or nanoshells that are inadequate for metafluids due to polydispersity, faceting, and thermal instabilities. To ensure that the separation gaps and resonances are uniform, more monodisperse spherical particles are needed. An additional challenge is the self-assembly of tetrahedral clusters in high yield from these particles. In self-assembly approaches that others have examined previously, the yield of any particular type of cluster is low.

In this dissertation I present solutions to several of these problems, developed in collaboration with my research group and others. We demonstrate that slow chemical etching can transform octahedral gold crystals into ultrasmooth, monodisperse

nanospheres. The particles can serve as seeds for the growth of larger octahedra which can in turn be etched. The size of the gold nanospheres can therefore be adjusted as desired. We further show that in colloidal mixtures of two sphere species that strongly bind to one another, the sphere size ratio determines the size distribution of self-assembled clusters. At a critical size ratio, tetrahedral clusters assemble in high yield. We explain the experimentally observed 90% yield with a nonequilibrium "random parking" model based on irreversible binding. Simulations based on this model reveal that 100% yield of tetrahedra is possible in principle. Finally, we combine these results and present methods for the self-assembly and purification of tetrahedral plasmonic nanoclusters, the simplest building blocks for isotropic metafluids.

Contents

List of Figures

List of Tables

Prior Publications

This thesis is primarily based on the following publications:

- Chapter 2: You-Jin Lee, **Nicholas B. Schade**, Li Sun, Jonathan A. Fan, Doo Ri Bae, Marcelo M. Mariscal, Gaehang Lee, Federico Capasso, Stefano Sacanna, Vinothan N. Manoharan, and Gi-Ra Yi, "Ultrasmooth, Highly Spherical Monocrystalline Gold Particles for Precision Plasmonics." *ACS Nano* **7** (12), 11064–11070 (2013).

- Chapter 3: **Nicholas B. Schade**, Miranda C. Holmes-Cerfon, Elizabeth R. Chen, Dina Aronzon, Jesse W. Collins, Jonathan A. Fan, Federico Capasso, and Vinothan N. Manoharan, "Tetrahedral Colloidal Clusters from Random Parking of Bidisperse Spheres." *Physical Review Letters* **110** (14), 148303 (2013).

Other works to which the author has contributed in graduate school include:

- Jonathan A. Fan, Yu He, Kui Bao, Chihhui Wu, Jiming Bao, **Nicholas B. Schade**, Vinothan N. Manoharan, Gennady Shvets, Peter Nordlander, David R. Liu, and Federico Capasso, "DNA-Enabled Self-Assembly of Plasmonic Nanoclusters." *Nano Letters* **11** (11), 4859–4864 (2011).

Other publications relating in part to work discussed in this thesis are in preparation.

Acknowledgments

I am grateful to many people for their assistance and encouragement prior to and throughout my time in graduate school. My success with research is in no small part due to their input and feedback on many occasions.

First, I thank my advisor, Vinny Manoharan, for giving me the opportunity to work on such an exciting project. I have learned a lot from Vinny and some of the most important lessons have had little to do with the details of soft matter physics and the design of experiments. Vinny has shown me the value of setting ambitious goals and striving toward them in a way that I did not previously have the confidence to appreciate. He also taught me, through instruction and example, the importance of motivation and storytelling in science communication and teaching.

My other committee members, Federico Capasso and David Nelson, have also been helpful and supportive over the last several years. It has been a pleasure to collaborate with Federico on manuscripts and he has always raised important questions about our work that led to deeper scientific understanding. I thank David for giving me such a strong background in electromagnetic theory during my first year of graduate school. In his course, he offered to include topics related to aspects of my research, such as negative refraction and metamaterials, and these lessons were invaluable to me when I was new to this field.

I am fortunate to have had the opportunity to collaborate on my research with brilliant people both at Harvard and around the world. My work built on research by Jon Fan and Dina Aronzon, who helped me determine which experiments to try by sharing their experiences with me. Jon has been particularly helpful to me throughout my graduate studies whenever I have had questions about electromagnetic theory,

electron microscopy, and spectroscopy techniques. Jesse Collins taught me how to do basic things when I was new in the lab, like pipetting and washing colloidal particles, and remained a helpful resource for thinking about science and geometry over the next several years. In my first year of graduate school, Jesse introduced me to a 1996 paper by Mansfield *et al.*, "The random parking of spheres on spheres" [13], which led to a new interpretation of my experiments and our publication in *Physical Review Letters* a few years later. For this work, Miranda Holmes-Cerfon and Beth Chen simulated random sphere parking and helped us understand our experiments and their implications.

I can't thank Gi-Ra Yi enough for giving me the opportunity to collaborate with him and his colleagues, You-Jin Lee, Gaehang Lee, Doo Ri Bae, and Stefano Sacanna. They shared their colloidal gold samples with me and were supportive and patient as we tried to understand how their spherical particles had formed. Our ongoing collaboration with Seungwoo Lee has been productive, as he has helped us explore methods of labeling these particles with DNA strands. Li Sun has been a wonderful collaborator on dark-field spectroscopy and electromagnetic simulations and helped me interpret the spectra that we measured. Marcelo Mariscal was gracious to help us with the embedded atom method calculations for this project. I thank H. Baik at KBSI for high-resolution TEM imaging. My discussions with Frans Spaepen were fruitful, as he suggested experiments that we could try with these particles which produced evidence that they were indeed out of equilibrium.

Many people have helped me with experimental methods and data interpretation over the course of my Ph.D. I was fortunate to have the opportunity to visit

Brookhaven National Laboratory and learn from Oleg Gang and Dazhi "Peter" Sun about how to functionalize gold nanoparticles with DNA. Peter has been especially helpful to me over the years as he has always replied promptly to my questions about the details of experimental protocols, even after he became a professor at SUSTC in China. In Harvard's Center for Nanoscale Systems, David Bell, Carolyn Marks, Adam Graham, and David Lange taught me how to do many types of electron microscopy and sample preparation with several different instruments over the years. I can't thank them enough for their patience and thoughtful suggestions. Ken Crozier and Marco Lončar taught me how to perform finite-difference time-domain simulations in their nanophotonics courses. These led to some important predictions that are relevant for my most recent experimental results. Ben Rogers has been helpful on innumerable occasions over the last several years with tasks from fiber coupling of lasers to DNA sequence design. The entire Manoharan group has benefited from his various areas of expertise and has been fortunate to have him as a colleague.

More recently, Arthur McClelland has helped me design and set up a dark-field spectroscopy instrument which may solve some of our ongoing experimental challenges. John Crocker and James McGinley have offered suggestions and kindly shared their laboratory procedures, which have proven beneficial to me in troubleshooting my experiments. The graduate students that I mentored in the lab, Emily Gehrels and Nabila Tanjeem, helped me frame problems, conducted numerous experiments, and explored a variety of ways in which our project could be extended. Nabila has been particularly resourceful over the past year as she developed a nanoparticle tracking analysis system for the lab and raised important questions about protocols that

strengthened our understanding of our experiments.

I have been fortunate to have several sources of financial support for my graduate research. I was supported from 2010 to 2013 by the US Department of Energy Office of Science Graduate Fellowship Program, administered by ORISE-ORAU under Contract No. DE-AC05-06OR23100. This fellowship enabled me to visit several of the DOE National Labs and to work with Oleg Gang and Peter Sun at Brookhaven. Various individuals at the DOE, particularly Ping Ge and Cayla Stephenson, were instrumental in arranging these visits. From 2013 to 2014 I received support from the Graduate Consortium on Energy and Environment, administered by the Harvard University Center for the Environment. I thank Mike Aziz, Dan Schrag, Joe Aldy, and Eric Simms for making this possible. Since 2014 I have been supported in part by the Derek Bok Center for Teaching and Learning at Harvard as the Departmental Teaching Fellow in Physics. Virginia Maurer and Jacob Barandes gave me this opportunity and helped me succeed in this role. The Department of Physics also supported me with the Purcell Fellowship, the An Wang Fellowship, the Wallace-Noyes Fellowship, and the Gertrude and Maurice Goldhaber Prize.

Our work has also been supported by the National Science Foundation NIRT program (Grant No. ECCS-0709323) and the Harvard Materials Research Science and Engineering Center (DMR-0820484, DMR-143-5964). Our work was supported in part by grants from the National Research Foundation of Korea (2009-0082451, 2010-0029409, 2010-1AAA001-0029018). My work was performed in part at the Center for Nanoscale Systems (CNS), a member of the National Nanotechnology Infrastructure Network (NNIN), which is supported by the National Science Foundation under NSF

Award No. ECS-0335765. CNS is part of Harvard University.

I thank the many members of the Manoharan group, past and present, whose patience, creativity, and camaraderie made the lab a wonderful place to work. Dave Kaz, Ryan McGorty, Kosta Ladavac, and Guangnan Meng taught me a lot about soft matter physics and always offered me practical advice about working in the lab. It was a pleasure to work with and learn from Jerome Fung, whose brilliant mind and boundless enthusiasm for physics and teaching were nothing short of inspirational. Becca Perry has always been a supportive colleague and thoughtful friend as we have followed parallel paths through graduate school. I will miss her good spirits and frequent advice that I should stop worrying and "bask" instead. I can't thank Tom Dimiduk enough for all his help, especially with issues related to programming, version control, and other aspects of computing. Our musings together on problems like the maximum possible height of snow in Boston kept work entertaining. Barbara Drauschke kept administrative matters running smoothly for the lab and was a life saver when I got stranded by an airline in Houston and needed to rent a car to drive to a conference in San Antonio.

I am grateful to the many people who joined the Manoharan lab after me for all that I have learned from them as well. Anna Wang helped me understand how to implement light scattering calculations and has always been an encouraging colleague and understanding friend. Jin-Gyu Park has been an invaluable expert on chemistry techniques and has prepared polymeric nanoparticles for my experiments that would not have been available without his help. Daniel Kunz, İrep Gözen, and Rees Garmann taught me several experimental techniques as well and became good friends of

mine. I thank Maddy Corbett and Aaron Goldfain for their help with optical instruments and computing in the lab and for being spirited ultimate teammates. I have always enjoyed conversations with Yoav Lahini about life and research and I have learned from his boundless enthusiasm for experimental science. Viva Horowitz has been an eager volunteer to assist with teaching and various tasks in the lab, and her optimistic attitude has made the lab a fun place to work. Ellen Klein was a terrific partner in adventure on our long and winding journey to San Antonio for March Meeting 2015. Manhee Lee, Reza Keshavarzi, Victoria Hwang, Andrew Bergman, Da-Young Kang, and Cyril Chomette were also great colleagues during the brief time that we worked together.

Additionally, I thank Sofia Magkiriadou, my closest friend from my time in the Manoharan group and my enthusiastic partner in scheming. Sofia has been a tremendous help to me in learning how to work with experimental optics and on many occasions she helped me refine my manuscripts and presentations. Most importantly, she has been a limitless source of good spirit, both in Cambridge and from Chicago, whether research was going well or not, and for this I can't thank her enough.

Many mentors, colleagues, and friends outside of the lab helped make my experience in graduate school an enjoyable one. I thank Melissa Franklin for being an encouraging mentor throughout my time at Harvard. Markus Greiner, Rob Hart, and Joe Peidle gave me valuable advice and a great experience with laboratory teaching in Physics 15c. David Morin, Sheila Ferguson, Dayle Maynard, Maggie McFee, Anne Trubia, and Lisa Cacciabaudo helped me sort out logistical, computing, and administrative situations and gave me useful advice on topics from Teaching Fellow

appointments to thesis defense scheduling. From my cohort in Harvard physics, Elise Novitski, Jean Anne Currivan, Alex Frenzel, Anna Klales, Kasey Phillips, Mike Yee, and Tony Pan helped me with innumerable tricky problem sets and became some of my best friends. Jonathan Nyquist, Michael Tang, Danny Hausmann, Jonathan Chong, Caitlin Fisher, Deborah Targoff, Novem Auyeung, On Tsang, the Ramgopals, and the Leiters always offered encouragement and a refreshing sense of humor about the trials and tribulations of being a graduate student.

I may not have ever begun a Ph.D. in physics without having learned from some exceptional physics teachers. Ron Francis introduced me to physics as a high school student, encouraged me to pursue physics and teaching, and ignited my passion for the field. At Brown, Jim Valles's enthusiasm for physics was contagious and he gave me my first opportunity to join a lab and see what real research was like. Bob Pelcovits showed me how fascinating electricity and magnetism can be and always encouraged me in my career and graduate research, even giving me the opportunity to present my first invited condensed matter seminar.

Lastly, I thank my family for always supporting me and my interest in math and science. I inherited the attitude of an engineer and scientist from my grandparents, particularly Bert Rosen and Ken Schade. I am especially grateful to my uncle, Ned Rosen, for encouraging me to think about all sorts of interesting ideas in math, even when I was very young. My brother, Steve Schade, has always been an enthusiastic partner in exploring innumerable topics in science and science fiction, from manned missions to Mars to giant monsters spawned from radioactive waste.

Finally and most importantly, I thank my parents, Mike and Lynn Schade, for

encouraging me and for giving me the opportunity to pursue these and other creative interests throughout my life. Thanks to them, I had my first microscope at home when I was not even ten years old, I had the opportunity to take summer courses in middle school at Boston's Museum of Science, and I had the chance to go to college at Brown and study physics and mathematics. I dedicate this dissertation to them.

Chapter 1

Introduction

The limits of technology are frequently determined by physical constraints. For instance, the fundamental limit on the speed of information transfer is the speed of light in vacuum, a physical constant. Transistors are limited in size by the sizes of atoms, and this imposes a constraint on the operational speed of conventional computers. Revolutionary technologies arise when a new technique or a new material makes it possible to reach beyond constraints that had once been considered fundamental.

Another example of such a limit is the range of indices of refraction accessible in materials at optical frequencies. The index of refraction is the ratio of the velocity of light in vacuum to its phase velocity in a particular material. It is a measure of how light slows down in the material and is therefore related to how that material interacts with light. Substances like glass and water have refractive indices greater than 1 because light travels more slowly in them than in vacuum. Metals and other materials that do not transmit light have complex indices of refraction with substantial imaginary parts, which are related to absorption. The ability to engineer a

material with a refractive index close to or less than zero can significantly broaden the range of material properties available. A negative index at optical frequencies could enable completely new optical devices, from wave guides to perfect lenses and perhaps even technologies that until now have sounded like science fiction, such as invisibility cloaks.

In this dissertation, I present experimental work aimed at reaching beyond conventional limits on refractive index in the visible. In particular, I examine the possibility of isotropic negative refraction and demonstrate solutions to several of the experimental obstacles that have kept it beyond reach.

1.1 Negative Refraction

A material with a negative index of refraction would be quite different from the materials people encounter in everyday life. Typically, the propagation direction of light changes at the interface between two dielectric media such that the light bends toward or away from the normal, as illustrated in Figure 1.1(a). If instead light travels from a material with a positive index to one with a negative index, it bends so that its Poynting vector $\mathbf{S}$ points toward the opposite side of the normal, as shown in Figure 1.1(b). In this case, the law of refraction (equation 1.1) is still satisfied at the interface,

$$n_1 \sin\theta_1 = n_2 \sin\theta_2, \tag{1.1}$$

but the angle of refraction is negative.

For centuries after Ibn Sahl, Willebrørd Snell, and others independently discovered

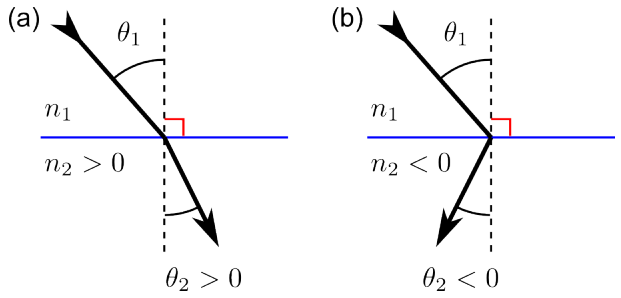

Figure 1.1: Light refracts at the interface (blue) between two media. (a) In conventional refraction, light bends toward or away from the normal as it crosses the interface. (b) Changing the sign of the refractive index results in the new propagation direction pointing toward the opposite side of the normal.

this law [14], there were no materials shown to have a refractive index less than zero. The idea of negative refractive index was considered physically impossible until Veselago showed otherwise, in a theoretical argument, nearly fifty years ago [1].

1.1.1 Theory

Veselago began by pointing out how the refractive index arises in the dispersion equation. For an isotropic substance and a monochromatic wave of frequency ω, the wave vector $\mathbf{k}$ and material properties are related by

$$k^2 = \frac{\omega^2}{c^2}\varepsilon_r\mu_r. \tag{1.2}$$

Here ε_r is the relative electric permittivity or dielectric constant of the material and μ_r is the relative magnetic permeability, defined by the usual constitutive relations

for non-chiral materials [15]:

$$\mathbf{D} = \varepsilon\mathbf{E} = \varepsilon_0\varepsilon_r\mathbf{E} \tag{1.3}$$

$$\mathbf{B} = \mu\mathbf{H} = \mu_0\mu_r\mathbf{H}. \tag{1.4}$$

Their product defines the refractive index n:

$$n^2 = \varepsilon_r\mu_r. \tag{1.5}$$

The sign of the refractive index appears at first to be ambiguous if the product of ε_r and μ_r is real:

$$n = \pm\sqrt{\varepsilon_r\mu_r}. \tag{1.6}$$

Furthermore, according to this equation, the refractive index is real as long as ε_r and μ_r are both positive or both negative. Under what circumstances is n negative and real? To answer this question, one must reexamine several fundamental results of electromagnetism and carefully trace how ε_r and μ_r propagate through them.

Left-Handed Materials

I begin with Maxwell's Equations in macroscopic media,

$$\nabla \cdot \mathbf{D} = \rho_{\text{free}}$$

$$\nabla \cdot \mathbf{B} = 0$$

$$\nabla \times \mathbf{E} = -\frac{\partial \mathbf{B}}{\partial t} \tag{1.7}$$

$$\nabla \times \mathbf{H} = \mathbf{J}_{\text{free}} + \frac{\partial \mathbf{D}}{\partial t}. \tag{1.8}$$

If one assumes monochromatic plane waves, the electric and magnetic fields can be written in the form

$$\mathbf{E} = \mathbf{E}_0 \mathrm{e}^{i(\mathbf{k}\cdot\mathbf{r} - \omega t)}$$

$$\mathbf{B} = \mathbf{B}_0 \mathrm{e}^{i(\mathbf{k}\cdot\mathbf{r} - \omega t)}.$$

Taking derivatives of these expressions and substituting into Faraday's Law (1.7), it can be shown that

$$\mathbf{k} \times \mathbf{E} = \omega \mathbf{B}.$$

If one takes the cross product of $\mathbf{E}$ with each side of this equation and employs vector identities, one finds

$$E^2 \mathbf{k} - (\mathbf{E}\cdot\mathbf{k})\,\mathbf{E} = \omega\,(\mathbf{E}\times\mathbf{B})\,. \tag{1.9}$$

Since $\mathbf{E}\cdot\mathbf{k} = 0$, the wave vector $\mathbf{k}$ must point in the same direction as $\mathbf{E}\times\mathbf{B}$.

Next I show that the wave vector does not necessarily point in the direction of en-

ergy flow. Poynting's Theorem [16, 17] states that energy flow in the electromagnetic wave is determined by the Poynting vector **S**:

$$\mathbf{S} = \mathbf{E} \times \mathbf{H}. \tag{1.10}$$

The Poynting vector and the wave vector point in the same direction when **B** and **H** point in the same direction, but this holds only when μ is positive, per equation 1.4. When μ is negative, the energy flow and phase velocity are in opposite directions. In a material where $\varepsilon < 0$ and $\mu < 0$, the vectors **E**, **H**, and **k** therefore do not obey the usual right hand rule (which still applies to **S** but not to **k**). Veselago thus coined the term "left-handed" for substances with negative ε and μ [1].

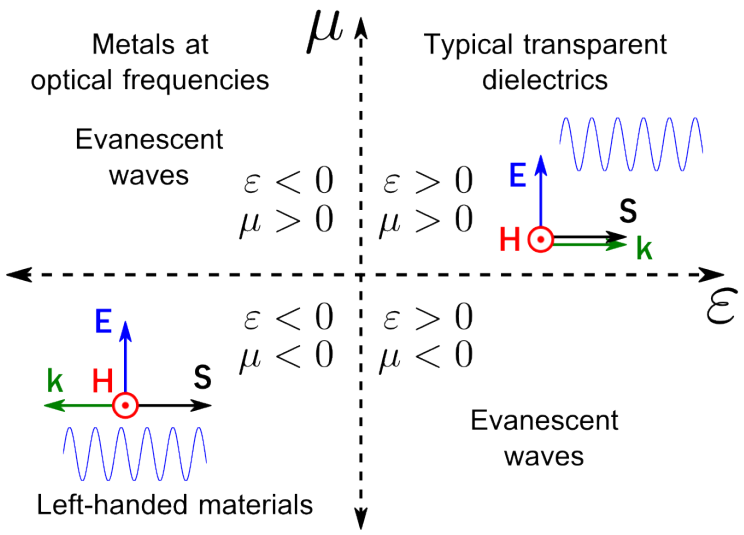

Figure 1.2: Light of frequency ω can propagate through a material only if the product of $\varepsilon(\omega)$ and $\mu(\omega)$ is positive. Common transparent dielectrics are in the upper right quadrant and metals occupy the upper left at optical frequencies. Left-handed materials are in the lower left quadrant. This figure is based on Figure 7 in Veselago [1], Figure 1 in Ramakrishna [2], and Figure 1.2 in Cai and Shalaev [3].

Figure 1.2 illustrates the space of conceivable materials in terms of permittivity and permeability [1, 2, 3]. In general this picture is incomplete because ε and μ can have substantial imaginary parts, which are related to absorption and impact the refractive index and attenuation loss in a material. Here I assume they are negligible to illustrate key features of the parameter space. Most materials have positive μ, which confines them to the upper half of this diagram. In the upper right quadrant, $(\varepsilon\mu) > 0$, so the refractive index is real, and the phase velocity and Poynting vector point in the same direction. Dielectrics like plastic, glass, and water are in this quadrant. In the upper left and lower right quadrants, $(\varepsilon\mu) < 0$, so the refractive index is imaginary, according to equation 1.5, and fields decay exponentially inside the material. Metals at optical frequencies are in the upper left quadrant. Some natural magnetic materials up to GHz frequencies occupy the lower right [1, 2, 3]. Left-handed materials are found in the lower left quadrant, where light can propagate but the phase velocity direction is reversed.

Refractive Index of Left-Handed Materials

I have not yet clarified whether one should choose the plus sign or minus sign for the refractive index of a left-handed material in equation 1.6. To resolve this question, I consider refraction of light at an interface. Two scenarios are illustrated in Figure 1.3. In Figure 1.3(a), light impinges at normal incidence on a left-handed material from a right-handed one. Causality and symmetry require that the Poynting vector points in the same direction in both media. In the left-handed medium, however, $\mathbf{k}$ points opposite to $\mathbf{S}$, so it follows that the phase velocity is reversed and

the wave vector points toward the interface in both media.

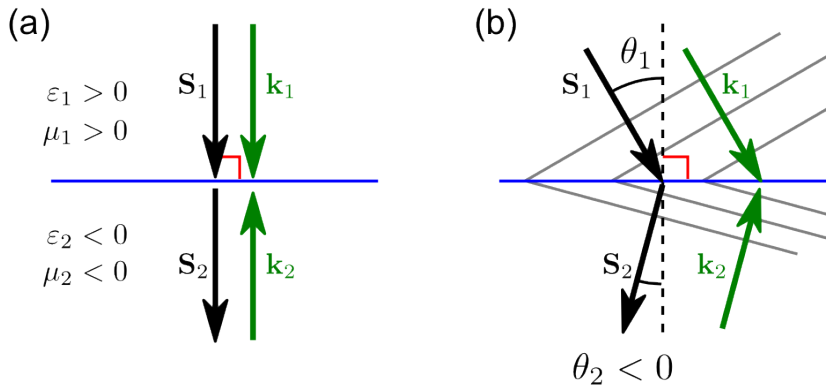

Figure 1.3: Refraction at an interface between right- and left-handed media. (a) At normal incidence, causality requires that the Poynting vector direction (black) remain constant across the interface, which means the wave vector (green) must change directions. (b) When the angle of incidence is nonzero, the wave must be refracted at a negative angle. Wave fronts are shown in gray.

Now I examine the case when the angle of incidence is nonzero, as shown in Figure 1.3(b). Causality requires that light transmitted into the left-handed material must have the vertical component of its Poynting vector $\mathbf{S}$ pointing downward, just as in the right-handed medium. The wave vector must therefore have an upward component, as in Figure 1.3(a). Also, the phase must be continuous across the interface in order to satisfy the electromagnetic boundary conditions (assuming that the interface has not been engineered to introduce phase discontinuities [18]). Owing to the horizontal component of the wavevector in the right-handed medium, lines of constant phase travel horizontally along the interface. The wave vector in the left-handed medium must therefore have a horizontal component in the same direction as its right-handed counterpart. Accordingly, the Poynting vector points down and to the left. The refracted ray must lie on the side of the normal opposite to where

one would ordinarily expect to find it, and the angle of refraction is negative.[1] Thus the left-handed material must have a negative refractive index to satisfy the law of refraction (equation 1.1).

1.1.2 Potential Applications

Negative refractive index remained a theoretical curiosity until John Pendry predicted a practical application [19]. Pendry extended Veselago's work by considering image formation by a flat slab with isotropic $\varepsilon_r = -1$ and $\mu_r = -1$, surrounded by vacuum. Veselago had pointed out that such a slab could behave like a lens because light from an object close to the slab is brought to a focus on the other side [1], as illustrated in Figure 1.4. In a plane parallel to and close to the slab, Pendry argued,

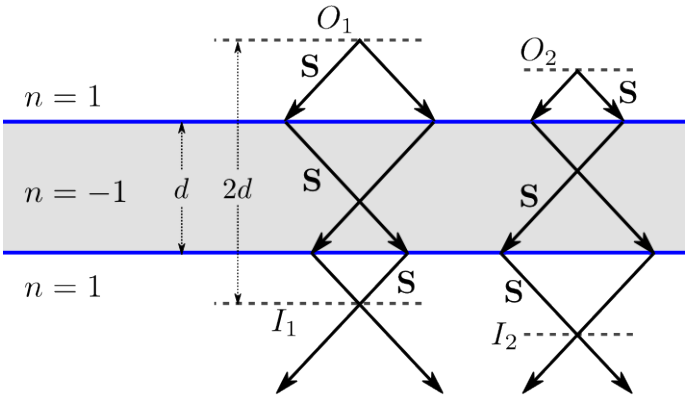

Figure 1.4: A flat slab of thickness d with $n = -1$ can bring light from a nearby object to a focus on the opposite side. Two example "object planes" O_1 and O_2 correspond to different "image planes" I_1 and I_2. Each object is a distance $2d$ away from its image.

[1] Veselago analyzed refraction at the interface between right- and left-handed media by invoking boundary conditions on **E** and **H**, rather than causality and phase continuity, but reached the same conclusion [1].

the electric field can be expressed in terms of a Fourier expansion,

$$\mathbf{E}(\mathbf{r},t) = \sum_{k_x,k_y} \mathbf{E}(k_x,k_y)\, \mathrm{e}^{i(\mathbf{k}\cdot\mathbf{r}-\omega t)}. \tag{1.11}$$

In vacuum, the dispersion equation (1.2) requires that

$$k_z = \sqrt{\omega^2 c^{-2} - \left(k_x^2 + k_y^2\right)}. \tag{1.12}$$

This expression gives a real value for the transverse wave vector k_z as long as $k_x^2 + k_y^2 < \omega^2 c^{-2}$. For high spatial frequencies corresponding to $k_x^2 + k_y^2 > \omega^2 c^{-2}$, however, k_z is imaginary. These Fourier components of the electric field would normally be lost to the image plane as evanescent waves.

Pendry calculated the Fresnel coefficients for transmission through and reflection from this slab and concluded that the reflection coefficient is 0, and the transmission coefficient is

$$T = \mathrm{e}^{-ik_z d}. \tag{1.13}$$

These evanescent waves are amplified in the negative-index slab. Pendry thus came to the surprising conclusion that flat sheets of negative-index material can be used as "perfect lenses," in that they recover all Fourier components of the electric field in the image plane. The conventional Abbe diffraction limit [20] does not apply to such a lens because information about subwavelength structure, which is ordinarily carried in the evanescent waves, is propagated to the image plane.

It is important to note that Pendry's perfect lens does not magnify. Instead, if an object is placed close to the slab, it forms a real image on the opposite side that

is exactly the same size as the object. Practical implementation of such a device would require a camera with subwavelength pixels. Alternative "hyperlens" designs can magnify but have more complex geometry and material requirements [21, 22]. Nevertheless, if researchers could fabricate a negative-index material and engineer a suitable way to record images, it would be a revolutionary technology. Biological samples might be imaged at nanoscale resolution without damage by electron beams, and photolithography techniques could reach a new regime for nanofabrication [3].

More generally, however, the availability of negative-index materials would give scientists and engineers far greater control over the optical properties of materials. Maxwell Garnett's theory [23] and Effective Medium Theory [24, 25, 3] explain how tunable effective optical properties emerge from combining materials with different refractive indices. Negative-index materials would make it possible to create new classes of composites and optical devices and may lead to new designs for anisotropic materials as well. For example, the technique of transformation optics [26] enables devices in which light travels along arbitrary, pre-programmed paths, but it requires precise control over ε_r and μ_r anisotropically at all points. The ability to engineer these material properties with precision could permit a practical implementation of this strategy for new technologies like invisibility cloaks [8] or light harvesters [27, 28].

1.2 Metamaterials

Metamaterials are artificial substances designed to exhibit physical properties that are not found in naturally occurring materials. No materials are known to exhibit $\mu < 0$ naturally at optical frequencies [3], and thus there are no known natural

substances that exhibit a negative index of refraction. The design of metamaterials with negative index requires a deeper understanding of how the electric permittivity and magnetic permeability of a given material are determined and how they can be manipulated.

1.2.1 Theory

To understand how to make a material with negative μ_r, one might first ask how to make a negative ε_r. Negative ε_r occurs in noble metals like gold and silver at optical frequencies [4]. One can explain this phenomenon using the Drude model.

Drude Model for the Permittivity of Metals

I begin by noting that the relative dielectric function ε_r is related to the electric field $\mathbf{E}$ and the polarization density $\mathbf{P}$ through the relationship

$$\mathbf{D} = \varepsilon_0 \mathbf{E} + \mathbf{P} = \varepsilon_0 \varepsilon_r \mathbf{E} = \varepsilon \mathbf{E}. \tag{1.14}$$

The polarization density $\mathbf{P}$ is the average electric dipole moment per unit volume, by definition [3]. In a metal, it can be expressed as

$$\mathbf{P} = -ne\mathbf{r}\left(t\right), \tag{1.15}$$

where n is the free electron density, $-e$ is the electron charge, and $\mathbf{r}\left(t\right)$ is the change in position of free electrons as a function of time. When monochromatic light impinges on a metal, the electric field varies sinusoidally in time and exerts a driving force on

free electrons at the surface of the metal. The equation of motion for an electron can be expressed as [5, 3]

$$m_e \frac{\partial^2 \mathbf{r}(t)}{\partial t^2} + m_e \Gamma \frac{\partial \mathbf{r}(t)}{\partial t} = -e\mathbf{E}_0 \mathrm{e}^{-i\omega t}, \tag{1.16}$$

where m_e is the mass of the electron and $\mathbf{E}_0 \mathrm{e}^{-i\omega t}$ is the incident electric field. Γ is a damping constant, related to viscous friction from inelastic collisions between electrons, electron-phonon coupling, and inelastic scattering from impurities [29]. This model assumes that all inelastic collisions may be treated with the same damping constant and it neglects long-range interactions between electrons or between the electron and bound ions [30]. It also says nothing about electrons within the ions.

The equation of motion has the solution

$$\mathbf{r}(t) = \frac{e\mathbf{E}_0}{m_e(\omega^2 + i\omega\Gamma)} \mathrm{e}^{-i\omega t}. \tag{1.17}$$

This equation describes collective oscillations in the free electron gas in the metal, associated with quasiparticles called plasmons. If one uses this result to substitute for $\mathbf{r}(t)$ in equation 1.15 and then substitute the resulting expression for $\mathbf{P}$ in equation 1.14, one finds an expression for the relative dielectric function:

$$\varepsilon_r(\omega) = 1 - \frac{\omega_p^2}{\omega^2 + i\Gamma\omega}, \tag{1.18}$$

where ω_p is the metal's plasma frequency,

$$\omega_p = \sqrt{\frac{ne^2}{\varepsilon_0 m_e}}. \tag{1.19}$$

Impact of Electric Dipole Resonances on Permittivity

Equation 1.18 only accounts for free electrons, but bound electrons contribute to the dielectric functions of metals as well. At optical frequencies, some bound electrons in noble metals can transition between bands. For instance, electrons can transition from the 5d to the 6sp state in gold when excited by light [31]. Since these electrons are bound, they are effectively subject to a restoring force $-k_b \mathbf{r}_b(t)$, and their equation of motion is

$$m_e \frac{\partial^2 \mathbf{r}_b(t)}{\partial t^2} + m_e \Gamma_b \frac{\partial \mathbf{r}_b(t)}{\partial t} + k_b \mathbf{r}_b(t) = -e\mathbf{E}_0 \mathrm{e}^{-i\omega t}. \tag{1.20}$$

Here Γ_b is the damping coefficient for bound electrons. The solution to this differential equation has a form similar to equation 1.17, but with a characteristic frequency $\omega_b = \sqrt{k_b/m_e}$ due to the restoring force:

$$\mathbf{r}_b(t) = \frac{e\mathbf{E}_0}{m_e(\omega^2 - \omega_b^2 + i\omega\Gamma_b)} \mathrm{e}^{-i\omega t}. \tag{1.21}$$

If one includes the bound electrons in the expression for the polarization density (equation 1.15), the result for the dielectric function becomes

$$\varepsilon_r(\omega) = \varepsilon_b(\omega) - \frac{\omega_p^2}{\omega^2 + i\Gamma\omega}, \tag{1.22}$$

where

$$\varepsilon_b(\omega) = 1 - \frac{\omega_{pb}^2}{\omega^2 - \omega_b^2 + i\Gamma_b\omega}. \tag{1.23}$$

Here Γ_b is the damping coefficient for bound electrons and ω_{pb}, the equivalent of a plasma frequency for bound electrons, is related to their number density in the same way that ω_p depends on the number density of free electrons (equation 1.19). Because the relative dielectric function is complex, it can be written in terms of a real part and an imaginary part:

$$\varepsilon_r(\omega) = \varepsilon_r' + i\varepsilon_r'', \tag{1.24}$$

where

$$\varepsilon_r'(\omega) = 1 - \frac{\omega_p^2}{\omega^2 + \Gamma^2} - \frac{\omega_{pb}^2(\omega^2 - \omega_b^2)}{(\omega^2 - \omega_b^2)^2 + \omega^2\Gamma_b^2} \tag{1.25}$$

$$\varepsilon_r''(\omega) = \frac{\omega_p^2\Gamma}{(\omega^2 + \Gamma^2)\omega} + \frac{\omega_{pb}^2\omega\Gamma}{(\omega^2 - \omega_b^2)^2 + \omega^2\Gamma_b^2}. \tag{1.26}$$

The last terms in equations 1.25 and 1.26 come from the bound electrons. These electrons contribute a Lorentzian resonance to the dielectric function, evident from equation 1.23 and shown in Figure 1.5. Here the real (ε_b') and imaginary (ε_b'') parts have been plotted using the values $\hbar\omega_b = 2.8$ eV, $\hbar\omega_{pb} = 3.0$ eV, and $\hbar\Gamma_b = 0.6$ eV for gold [3], obtained by fitting to measured optical properties. The peak in (ε_b''), centered at about 450 nm, corresponds to increased absorption for blue and green light, which gives gold its signature color. Near this resonance, the real part (ε_b') varies substantially, and even drops below zero.

The free electron contribution to the dielectric function may be included as well to

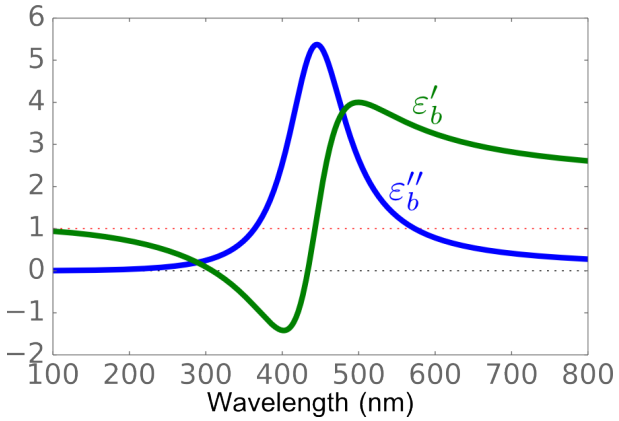

Figure 1.5: Contribution of bound electrons to the real (green) and imaginary (blue) parts of the relative dielectric function of gold, calculated using equation 1.23. This plot is based on Figure 2.5 in Cai and Shalaev [3].

calculate the refractive index of gold using equation 1.22 and assuming that $\mu_r = 1$ at optical frequencies. The refractive index in this case has both real (n) and imaginary (k) components, both of which are plotted as a function of wavelength in figure 1.6. Here I use the values $\hbar\omega_p = 9.1$ eV and $\hbar\Gamma = 0.072$ eV, based on the experimental data of Johnson and Christy [4], which are widely used [3]. The model and data agree well, particularly at wavelengths longer than 500 nm and far into the infrared.

This analysis reveals that electric dipole resonances affect the bulk permittivity and refractive index of a material. Moreover, because ε_r is a material property that is meaningful only at length scales on the order of a wavelength or longer, subwavelength components of a composite material [24, 25, 3] can also alter the effective permittivity of the material if they introduce electric dipole resonances.

How can one introduce electric dipole resonances into a transparent dielectric? One way is to dope it with metallic nanoparticles. If an electromagnetic wave illuminates a subwavelength metal particle, the free electrons at the surface of the

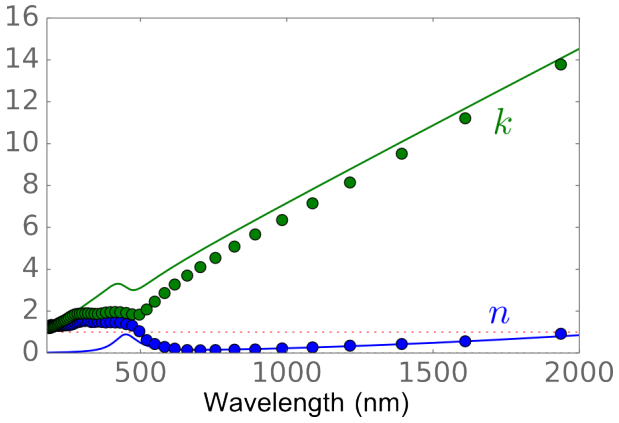

Figure 1.6: Refractive index (blue) and extinction (green) for gold. Solid curves are calculated using equation 1.22. Data (circles) are from Johnson and Christy [4].

metal are subject to the same forces as the free electrons described by equation 1.16. However, the fact that they are constrained to a small volume introduces a restoring force $-K\mathbf{r}(t)$, where the spring constant K depends on the size and geometry of the particle.

$$m_e \frac{\partial^2 \mathbf{r}(t)}{\partial t^2} + m_e \Gamma \frac{\partial \mathbf{r}(t)}{\partial t} + K\mathbf{r}(t) = -e\mathbf{E}_0 \mathrm{e}^{-i\omega t} \tag{1.27}$$

Equation 1.27 has the same form as equation 1.20, the equation of motion for the bound electrons, a damped harmonic oscillator model. It shows that the free electrons in a nanoparticle have a resonant frequency $\omega_0 = \sqrt{K/m_e}$. The oscillation of the free electron gas in response to the external field is illustrated in Figure 1.7.

Unlike the resonance of the bound electrons, the resonance of the free electrons in the nanoparticle can be tuned geometrically since the spring constant K is related to the particle size. The spring constant and resonance frequency both increase with decreasing particle radius. Spectroscopy measurements have confirmed that the electric dipole resonance redshifts with increasing particle size [32, 33]. Effective

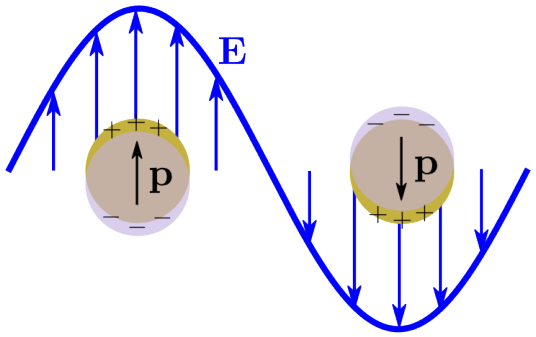

Figure 1.7: Electromagnetic waves drive oscillations in the free electrons at the surface of a metal nanoparticle, creating an electric dipole resonance. This figure is based on Figure 1 of Moores and Goettmann [5].

Medium Theories [23, 24, 25, 3] relate the optical properties and volume fraction of metal nanoparticles to the macroscopic permittivity of the metamaterial. Thus, adjusting the size and shape of subwavelength metal particles in a dielectric makes it possible to engineer a metamaterial with controlled ε_r and index of refraction.

Achieving $\varepsilon_r < 0$ requires a narrow resonance. This means that absorption must be small relative to scattering, or, equivalently, the scattering cross section σ_{scatt} of the nanoparticle must exceed its absorption cross section σ_{abs}. These parameters are different functions of the particle radius R [34, 35]:

$$\sigma_{\text{scatt}} \propto R^6$$

and

$$\sigma_{\text{abs}} \propto R^3$$

for $R \ll \lambda$. Thus, larger nanoparticles have sharper resonances. For gold nanoparticles, the scattering cross section exceeds the absorption cross section when the particle

diameter is larger than 80 nm [36].

Manipulation of Permeability with Magnetic Dipole Resonance

Since the electric permittivity of a metamaterial can be tuned with electric dipole resonances, it follows that the magnetic permeability can be tuned with magnetic dipole resonances. The relative permeability μ_r is related to the magnetic field $\mathbf{H}$ and magnetization $\mathbf{M}$ in the same way that the relative permittivity ε_r is related to the electric field $\mathbf{E}$ and polarization $\mathbf{P}$. The relationship between $\mathbf{B}$, $\mathbf{H}$, $\mathbf{M}$, and μ [17, 3],

$$\mathbf{B} = \mu_0 \left(\mathbf{H} + \mathbf{M}\right) = \mu_0 \mu_r \mathbf{H} = \mu \mathbf{H}, \tag{1.28}$$

parallels that between $\mathbf{D}$, $\mathbf{E}$, $\mathbf{P}$, and ε (equation 1.14). However, magnetic dipole resonances are more difficult to engineer at optical frequencies than electric dipole resonances because, above GHz frequencies, the magnetic permeability of all known naturally occurring materials is always close to the permeability of vacuum. This is a consequence of the fact that the magnetic field in light interacts with atoms much more weakly than the electric field does due to the absence of magnetic charge [37]. This asymmetry between electric and magnetic phenomena even led the authors of a widely used electromagnetism textbook to suggest that magnetic susceptibility is meaningless at optical frequencies and above [38].

Pendry and colleagues [6] found a solution to this problem: the split-ring resonator. A split-ring resonator is a planar subwavelength device consisting of concentric, incomplete loops of metal embedded in a dielectric. Incident electromagnetic waves can couple strongly to circulating current modes that can be engineered through the

geometry of the device. The concentric rings of metal give the device inductance L, while the gaps in the metal and the close proximity of concentric rings provide capacitance C. Thus, a split-ring resonator is essentially an LC circuit [Figure 1.8(a)]. The resonant frequency of the LC circuit, $\omega = (LC)^{-1/2}$, can be tuned by changing the rings and gaps.

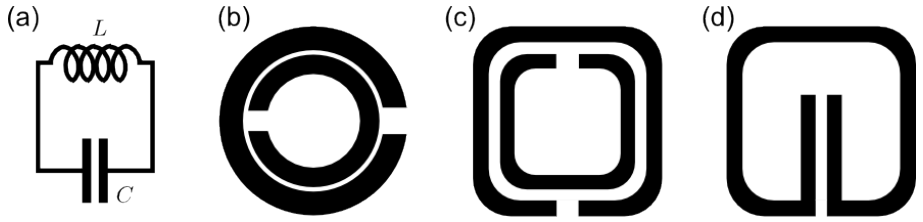

Figure 1.8: A split-ring resonator uses external electromagnetic waves to establish a circulating current resonance, like that found in an LC circuit (a), in order to manipulate μ_r in a metamaterial. Examples include (b) the original design by Pendry *et al.* [6], (c) the first design for which negative refraction was observed [7], and (d) the resonator used in the first realization of electromagnetic cloaking [8].

Because its current circulates in the plane, a split-ring resonator produces a magnetic dipole pointing out of the plane. Thus, light can drive the structure to resonate magnetically, rather than just electrically. A metamaterial with tunable μ_r can be constructed from dense arrays of split-ring resonators. Figure 1.8(b) shows the original proposed split-ring resonator [6], and Figure 1.8(c)-(d) show designs from some of the first successful implementations of these devices [7, 8].

With this theoretical framework in place, the basic requirements for fabricating metamaterials with exotic optical properties are clear. A metamaterial can be made from a positive-index material containing a high density of subwavelength structures whose geometry affords them both electric and magnetic dipole resonances. The electric resonances control ε_r and the magnetic resonances control μ_r. The geometry

and number density of the structures, along with the materials from which they are made, determine the effective permittivity and permeability.

1.2.2 Conventional Fabrication Routes

Since metamaterials require subwavelength components, the first ones were designed for macroscopic wavelengths so that they could be built using printed circuit board technology. Shelby *et al.* [7] built a metamaterial by printing two-dimensional arrays of copper split-ring resonators and wires on interlocking circuit-board material. They showed that resonators on the millimeter scale, with the design shown in Figure 1.8(c), led to a negative ε_r and μ_r for wavelengths on the order of centimeters. The measured index of refraction of their metamaterial was $n = -2.7 \pm 0.1$. Other examples of metamaterials at microwave frequencies, made using similar schemes, soon followed [8].

Making metamaterials for optical frequencies, however, is a nanotechnological challenge, because the resonators must be on the order of 100 nm or smaller. The first candidate techniques for making such structures were top-down methods such as electron-beam lithography [39, 10] and focused ion beam milling [9, 40]. In both methods, a beam of charged particles is focused to a small spot on a sheet of material in order to carve a nanostructure. Although these methods can be used to build split-ring resonators, they have significant drawbacks. First, they are serial techniques in which one nanostructure is made at a time, and thus manufacturing bulk quantities of metamaterial by these methods is slow and expensive. Second, they are limited in precision and resolution by the spot size, which is typically about 10 nm [3]. While

this size is much smaller than the resolution limit of techniques like photolithography, it limits the gap sizes and conductor spacing in the resonator, making it impossible to use certain designs.

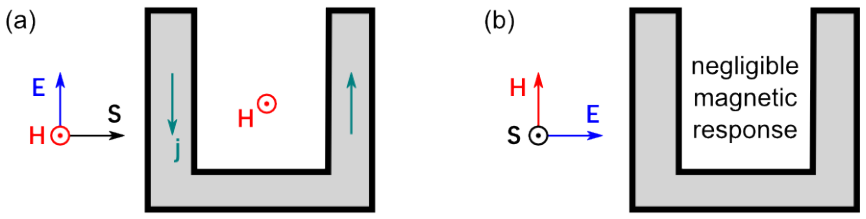

Figure 1.9: Planar split-ring resonator design used for optical metamaterials [9, 10]. (a) Light propagation within the plane can excite a strong magnetic dipole response for one polarization, since the electric field can drive currents **j** in the arms of the resonator. (b) At a different orientation, the magnetic response is much weaker.

Most problematically, these methods produce nanostructures that are inherently two-dimensional. Split-ring resonators are designed to couple to an electromagnetic wave coming from a specific direction and having specific polarization. If the resonator rotates with respect to the source, its electromagnetic response can differ dramatically, as illustrated in Figure 1.9. Thus, two-dimensional arrays of split-ring resonators are inherently anisotropic metamaterials. While it is possible to build interlocking arrays of millimeter-scale split-ring resonators [7] to partially compensate for the anisotropy of a single two-dimensional array, this is not a straightforward process with their nanoscale counterparts. It is possible to stack the arrays to create a three-dimensional lattice of resonators [10, 40] but such lattices are still anisotropic.

1.3 Metafluids

Many applications, such as perfect lensing [19], require metamaterials with an isotropic response. Such materials are best fashioned from subwavelength elements whose resonances are themselves isotropic. Isotropic resonances require nanostructures of a geometry different from that of planar split-ring resonators.

If isotropic subwavelength resonators could be made, their orientations relative to one another and relative to the incident light would have no effect on the optical properties of the metamaterial. Even if the structures were dispersed randomly in a fluid, where they could translationally and rotationally diffuse, they would still respond to incident light. Thus, a concentrated colloidal suspension of isotropic electromagnetic resonators would be a fluid metamaterial, also known as a metafluid [41].

A metafluid could enable additional technologies that are impossible with solid metamaterials. For instance, they could be used in microfluidic waveguides whose modes, unlike those of conventional waveguides, could be dynamically adjusted by tuning the fluid composition and flow rates [42]. Such waveguides have been demonstrated with aqueous solutions, but the availability of metafluids would expand the range of refractive indices available for these systems and would make different mode profiles possible. Fluidic lenses are another potential application. A lens made from a liquid has a smooth, spherical surface, and its radius of curvature and focal length can be dynamically adjusted using pressure [43]. As with microfluidic waveguides, metafluids could be used to increase the range of possible refractive indices for a fluidic lens. Moreover, they may make it possible to dynamically tune both the curvature and the refractive index.

1.3.1 Theory

Urzhumov *et al.* [41] used plasmon hybridization theory [44, 45], which relates the electromagnetic resonances of various structures to their symmetries, to show that some regular polyhedral clusters of metal nanoparticles exhibit isotropic electric and magnetic dipole resonances [41]. Examples include Platonic solids such as the tetrahedron, octahedron, and icosahedron.

To understand this prediction, one can consider the tetrahedron, whose symmetry corresponds to the T_d point group. Irreducible representations of the T_d group generate all possible arrangements of four electric dipoles situated at the vertices of a tetrahedron. Because the representations corresponding to electric and magnetic dipoles are each three-fold degenerate, these modes are three-dimensionally isotropic.[2]

Another way to understand this prediction is to consider each face of the tetrahedron as a collection of three metal particles. If there are gaps between these particles, they form a split ring, analogous to an LC circuit or a conventional split-ring resonator [Figure 1.8]. Because there is a fourth particle in the cluster, one can think of the structure as consisting of four split-ring resonators with different orientations. No matter how the structure is oriented with respect to incoming light, a magnetic dipole resonance can be excited in at least one face of the structure, or in at least three of the four particles, as illustrated in Figure 1.10(a). Thus, to make an optical metafluid, one needs only a dense suspension of tetrahedral clusters of metal nanospheres [Figure 1.10(b)] [41]. Negative index of refraction requires that the elec-

[2]The lowest-order electric multipole of the magnetic dipole resonance for the tetrahedron is an electric octupole ($2^3 = 8$) [41].

tric and magnetic dipole resonances overlap and these resonances are sensitive to the gaps between the particles. The resonant frequencies can redshift by up to 10% if the separation gaps decrease by just 1 nm [11], so nanometer precision is required to ensure that all clusters have uniform resonances.

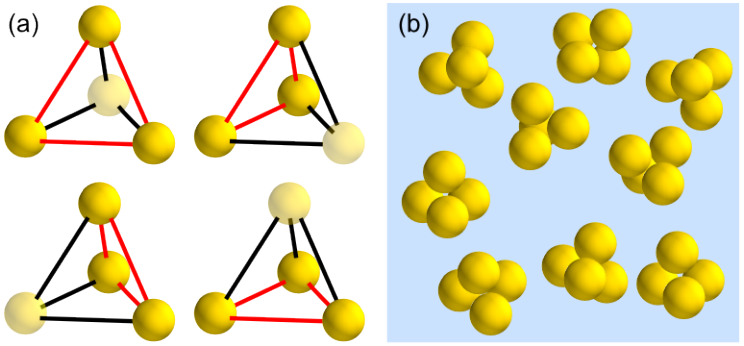

Figure 1.10: Tetrahedral clusters of metal nanospheres are isotropic electromagnetic dipole resonators. (a) Any set of three spheres is analogous to a split-ring resonator. Incident light of an appropriate frequency will excite a magnetic dipole resonance in at least one face of the tetrahedron, regardless of its orientation. (b) A metafluid is a dense, disordered collection of these clusters.

Since the building blocks for metafluids are three-dimensional structures, they cannot be made using conventional fabrication routes, which yield two-dimensional structures. A promising alternative is to make three-dimensional plasmonic nanoclusters "from the bottom up," using self-assembly. In this scheme, one controls the interactions between metal nanoparticles in a fluid such that specific clusters can assemble. The clusters must be as symmetric and as uniform as possible so that their optical properties are isotropic and reproducible.

1.3.2 Previous Experiments

The simplest designs for optical metafluids call for symmetric clusters of metal nanoparticles [41, 37]. There are many methods for making spherical particles of noble metals. A number of groups have developed mechanisms for making clusters on this length scale.

Metal Nanoparticles and Nanoshells

The study of gold nanoparticles has a rich history going back at least as far as Michael Faraday [46]. Modern techniques for the preparation of commercial gold nanoparticles are based on citrate reduction of $HAuCl_4$ in water [47, 48]. This method yields particles that are approximately spherical and monodisperse. However, electron microscope images show that the particles have irregular, polyhedral morphologies, as shown in Figure 1.11(a).

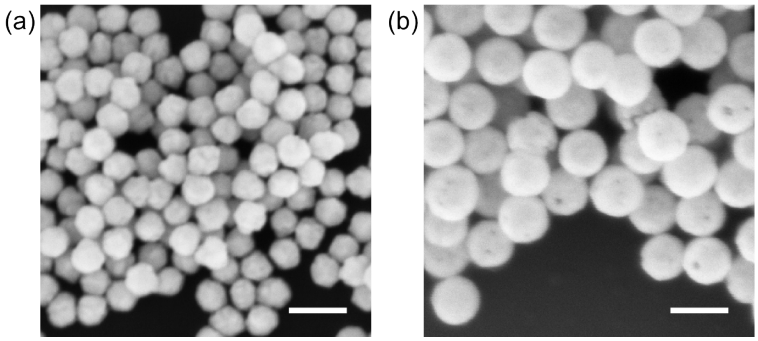

Figure 1.11: (a) Gold particles prepared by citrate reduction of $HAuCl_4$ are faceted, polyhedral crystals. This sample is from a batch purchased from Nanopartz, Inc. (b) Gold nanoshells with silica cores are more spherical and monodisperse but can have pinholes and the gold may dewet from the silica. Scale bars are 200 nm.

Gold nanoshells are preferred for many applications because they are more spherical. Oldenburg *et al.* [49] developed a procedure for synthesizing these particles, which consist of a gold film grown on a spherical silica core. The thickness of the gold layer can be controlled during synthesis, so that the ratio of core to shell diameter can be used to tune the electric dipole resonance [49, 44]. However, pinholes can develop in the gold layer [Figure 1.11(b)] and this can lead to dewetting or other changes in nanoshell morphology [50]. Smooth, spherical metal particles with superior thermal stability are needed for further progress in metafluid engineering.

Cluster Self-Assembly

Many groups have investigated colloidal self-assembly as a means of preparing small clusters. One method involves attaching particles to the surfaces of emulsion droplets and then evaporating fluid from the droplets. Capillary forces bring the particles togther in small clusters with well-defined, symmetric configurations such as tetrahedra and octahedra [51, 52]. However, the method generates a mixture of clusters, and the yield of any single type is low, unless the clusters are separated by size by using a density gradient [53]. It is also possible to control the geometry of nanoparticle clusters by assembling "patchy particles" [54, 55], but it is not clear how to make metal nanoparticles with well-defined nonspherical geometries.

It is possible to assemble small numbers of metal nanoparticle clusters. Drying a colloidal suspension of gold nanoshells on a dielectric substrate results in the self-assembly of two-dimensional clusters. Triangular clusters assembled this way have been shown to exhibit a magnetic dipole resonance [11]. It is also possible to assemble

plasmonic clusters in templated patterns on substrates [56, 57], but because they must assemble on a surface, the yield is limited compared to that of self-assembly in bulk.

New routes to self-assembly of three-dimensional plasmonic nanoclusters have emerged recently. For instance, Urban *et al.* [58] encapsulated small numbers of metal nanoparticles in polymer spheres. They found evidence of isotropic response in a gold nanoparticle tetrahedron. However, this method offers little control over interparticle separations, and the yield of any particular cluster geometry is limited. An alternative is to assemble large clusters from metal nanoparticles on the surface of a much larger dielectric particle [59, 60]. This method is claimed to yield materials with a magnetic response at optical frequencies, but one cannot control the number of nanoparticles per structure or the gaps between the nanoparticles. One can mitigate this problem by using icosahedral viruses as the dielectric particles and directing gold nanoparticles to bind at their vertices [61]. A high yield of icosahedral clusters is possible in principle, but the virus must be genetically engineered to exhibit thiol groups at the desired sites on the capsid, and even then, many clusters are incomplete icosahedra. Moreover, all of these approaches have used irregular nanoparticles or unstable nanoshells.

1.4 Overview

Our goal is develop a material exhibiting isotropic negative refraction at optical frequencies. Metafluids are the most promising route to such properties, since they contain isotropic electromagnetic resonators, and the arrangement and orientation of the resonators need not be controlled. Since a metafluid can be made from three-

dimensional clusters of plasmonic nanospheres, colloidal self-assembly appears to be the most promising way, if not the only way, to make one.

In this dissertation, I present our progress towards this goal. First, I show in Chapter 2 that spherical, smooth, monodisperse, and stable gold nanoparticles can be made by combining nanocrystal growth with slow chemical etching. My collaborators and I demonstrate that the plasmonic behavior of these individual nanospheres is reproducible and uniform, unlike that of conventional gold nanoparticles. In Chapter 3, I show that self-assembly of tetramers in high yield is experimentally achievable. We accomplish this by mixing spherical particles with larger spheres that can bind randomly and irreversibly to the smaller ones. In Chapter 4, I discuss simulations of magnetic resonances in tetrahedral gold clusters and examine how key geometric parameters affect the resonance. In Chapter 5, I apply our nonequilibrium self-assembly method to our spherical gold particles and present methods for the self-assembly and purification of tetramers composed of gold nanospheres. Finally, in Chapter 6, I propose some experiments to build on these results and to ultimately demonstrate high-yield self-assembly of isotropic, reproducible electromagnetic resonators for optical frequencies.

Chapter 2

Ultrasmooth, Highly Spherical Monocrystalline Gold Particles for Precision Plasmonics

2.1 Introduction

In equilibrium, a nanoscale crystal adopts a polyhedral morphology to minimize its surface free energy. As a result, metallic nanoparticles grown near equilibrium form facets [62, 63, 64]. Although the plasmon resonances and ease of functionalization [65] make such particles promising for bottom-up assembly of optical resonators [11, 66] and isotropic metamaterials [41], it is difficult to make structures whose optical

properties are reproducible from one particle or one multiple-particle cluster to the next since the resonances are often sensitive to features such as sharp corners [67], number of facets [68], roughness [69], and overall size and shape [70]. Moreover, the interparticle optical coupling varies significantly with nanometer-scale changes in gap distance [71] and orientation [72]. The ideal particle for self-assembly of plasmonic structures is therefore not a polyhedron, but a spherical crystal without facets or grain boundaries. However, producing such particles is a materials challenge, since spherical crystals are not stable under any growth conditions.

Here we show that a cyclic process of slow growth followed by slow chemical etching, which selectively removes edges and vertices, results in ultrasmooth, highly spherical monocrystalline gold particles. The etching process, which is functionally similar to (but chemically different from) that used to make monocrystalline silver nanospheres for surface-enhanced Raman spectroscopy [73, 74], effectively makes the surface tension isotropic, so that spheres are favored under quasi-static conditions. The resulting spherical crystals display uniform scattering spectra and consistent optical coupling at small separations, even showing Fano-like resonances [12] in small assemblies. The cyclic process we demonstrate could be extended to other metals and, because it is scalable up to particle sizes of 200 nm or more, might be used to create strongly scattering particles for sensors [36, 75], electromagnetic resonators [41], and other optical devices [76].

The challenge of synthesizing metallic nanoparticles with controlled morphology is intimately connected to how crystals grow. Unlike silica or polymer nanoparticles, metallic nanoparticles are crystalline and tend to adopt distinct facets when grown in a

bulk suspension. As first described by Gibbs [77] and Wulff [78], facets form because they minimize the surface free energy, which is a function of the exposed crystal planes. The number of facets can be controlled by chemically inhibiting the growth of certain crystal surfaces. This method has been used to produce nanoparticles with a variety of different shapes, including tetrahedra [62], octahedra [63, 67], cubes [67], and higher-order polyhedra [64]. However, even pseudospherical particles [79] produced this way have small facets.

We are not aware of any growth method that results in smooth, spherical nanocrystals. Quasi-spherical gold nanoparticles grown near equilibrium tend to increase in polydispersity and ellipsoidal eccentricity with increasing average particle diameter [80, 81]. Nevertheless, fundamental studies of plasmonic phenomena [82, 66] have proceeded under the assumption that such particles are adequate substitutes for spheres. An alternative is heterogeneous growth on a spherical dielectric shell, which produces nanoshells [49] that are spherical but polycrystalline, and as a result have rough surfaces and grain boundaries that can lead to additional losses in plasmonic applications. Nanoshells are also subject to dewetting [83] and thermal instabilities [50].

Our solution to this quandary is to use both growth and etching, rather than simply adjusting the growth conditions, to make solid gold nanospheres. The growth step produces single-crystalline polyhedral particles, while the chemical etching step selectively removes edges and vertices while leaving the crystal structure intact. It is important that both steps are quasi-static, to avoid instabilities. The effect of the reduction-oxidation etching process is analogous to introducing an isotropic surface tension, which leads to spherical particles as the particle size decreases. By alternating

between anisotropic growth and isotropic etching, we create smooth, spherical, single-crystalline particles of any desired size, up to 200 nm and conceivably larger. These spherical crystals are smoother than state-of-the-art polycrystalline or commercial particles and, as a result, show much more uniform optical properties, making them ideal building blocks for self-assembly of plasmonic nanostructures.

2.2 Results and Discussion

2.2.1 Synthesis of Uniform, Stable Gold Nanospheres

We start by synthesizing single-crystalline gold octahedra, following a procedure similar to that of Li *et al.* [63]. (See Section 2.4.1 for details.) The particles grow by the slow reduction of chloroauric acid ($HAuCl_4$) in ethylene glycol, which acts as a reducing agent at elevated temperature, with poly(diallyl dimethyl ammonium chloride) (polyDADMAC) and phosphoric acid (H_3PO_4). PolyDADMAC, a cationic polyelectrolyte, stabilizes the nanoparticles, and phosphoric acid controls the reduction rate of chloroauric acid [63]. The resulting uniform gold octahedra are 135.4 $\pm$ 12.5 nm in edge length [Figure 2.1(a)]. A small number of particles with different shapes, such as decahedra and truncated triangular bipyramids, are also formed in this reaction but constitute less than 5% of the total.

To smooth the vertices and edges, we add an oxidizing agent, chloroauric acid, to the unwashed gold octahedron suspension after it cools. Chloroauric acid favors oxidation of the gold atoms specifically at vertices and edges, where the atoms have the lowest coordination [84]. Although chemical etching processes have been used

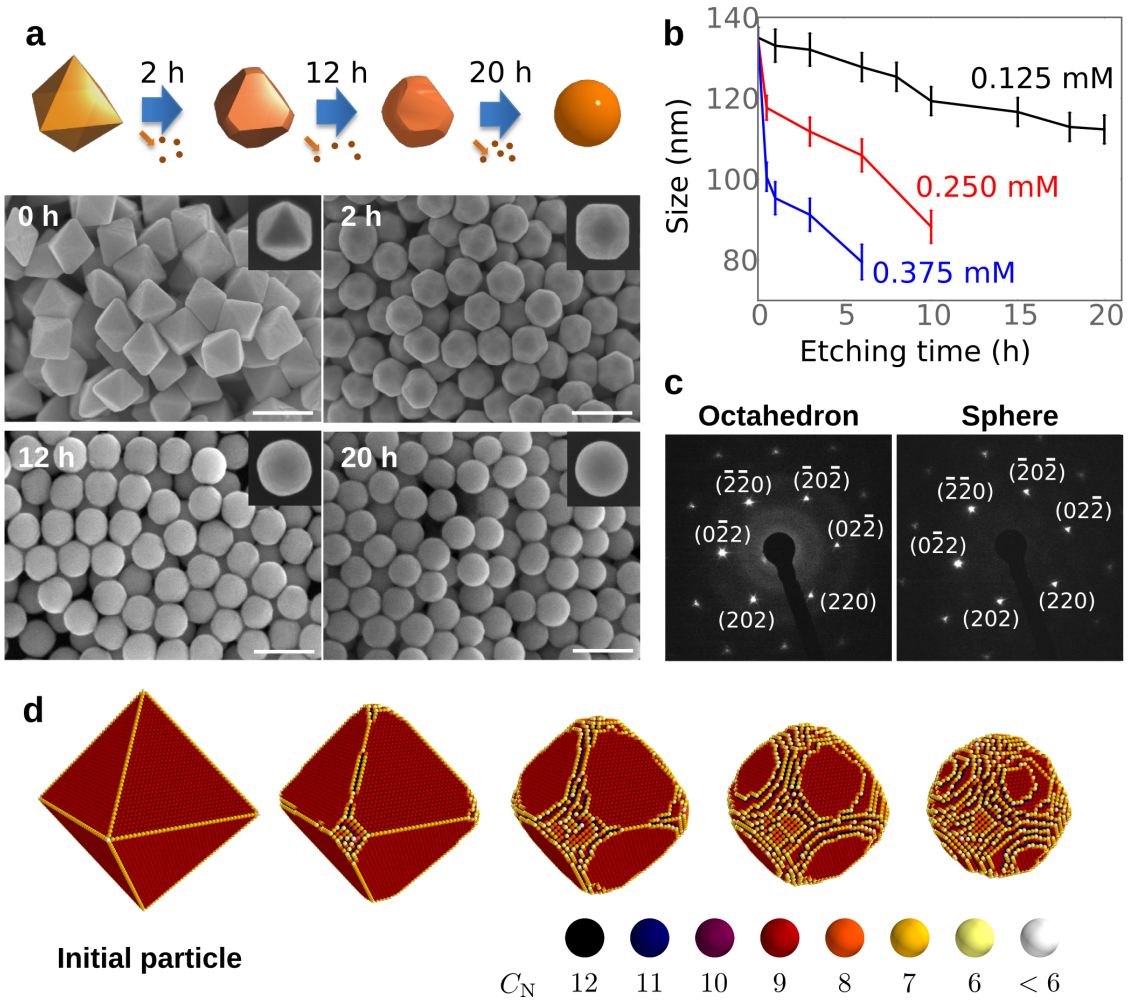

Figure 2.1: Growth followed by etching produces uniform, monocrystalline nanospheres. (a) Schematic diagram of shape evolution of gold particles during the etching process. SEM images of gold nanoparticles after chemical etching for various durations show the gradual transformation from octahedra to spheres. Scale bars are 200 nm. (b) Particle size as a function of etching time after the addition of $HAuCl_4$ in different concentrations. (c) Electron diffraction pattern of an octahedral particle and a spherical particle, showing that both are single crystals. (d) Sequential states in the simulated etching of a gold octahedron with edge length 40 atoms. The color of each atom corresponds to its coordination number C_N and energy.

to change the shape of polyhedral metal nanoparticles into exotic shapes, in general these processes do not produce uniform spheres [85]. Our etching process differs in that it is designed to be slow, so as to avoid instabilities leading to anisotropy, polydispersity, or significant reductions in particle size. Over the course of 20 h, the particles progress from octahedra to truncated octahedra, quasi-spheres, and finally smooth gold nanospheres of diameter 112.3 ± 8.2 nm [Figure 2.1(a)]. As shown in Figure 2.1(b), the particle size decreases abruptly at first and then decreases more slowly as the oxidation-reduction reaction approaches equilibrium, and the chemical potential difference vanishes. Electron diffraction patterns of individual octahedra and spheres [Figure 2.1(c)] indicate that each nanoparticle is a single, face-centered cubic crystal, both before and after the etching reaction.

Monte Carlo simulations of the etching process (Section 2.4.1), using atom energies calculated as a function of coordination number using the embedded atom method [86], show that the oxidation conditions alone can explain the transformation to a sphere. The embedded atom method calculations predict that gold vertex atoms have a free energy of 26 $k_{\mathrm{B}}T$ and edge atoms of 10 $k_{\mathrm{B}}T$ relative to the [111] faces. These conditions favor the removal of vertices and edges before faces, as shown in Figure 2.1(d). Although these simulations do not model diffusive dynamics, they do show that energetics favor the transition to a spherical morphology before the surface layers on the faces of the original octahedron are completely removed. Because the difference in free energy between faces is only 3.9 $k_{\mathrm{B}}T$, the anisotropy in the surface tension is small compared to the difference in free energy between edges and faces or between vertices and faces. Thus the surface tension is effectively isotropic, and it

favors the removal of regions of high curvature.

2.2.2 Cyclic Growth and Etching Process

The etching process leaves the crystal structure of each particle unperturbed, resulting in true spherical crystals, as evidenced by high-resolution transmission electron micrographs [Figure 2.2(a)]. To further confirm that the crystalline order extends to the boundary of the nanospheres, we used 112.3 ± 8.2 nm gold spheres produced by our growth and etching process as seeds for a second growth reaction [Figure 2.2(b)] (Section 2.4.1). This resulted in larger octahedra with edge length 156.5 ± 13.8 nm [Figure 2.2(c)]. If the original spheres were not monocrystalline, we would not expect that the regrowth reaction would result in such uniform and smooth octahedra.

The seeded growth experiments also illustrate a route to larger gold nanospheres through cyclic etching and growth. We initiated another etching reaction using the regrown octahedral particles and found that these too transformed into spheres. The new batch of nanospheres was larger (131.2 ± 9.5 nm) than the original seed spheres we had obtained after 20 h. We produced larger octahedral gold particles in a third growth step (173.3 ± 15.1 nm), and as we continued this procedure, we obtained smooth gold spheres of diameter 200 nm after seven iterations (Section 2.4.1). We know of no other route to such large and uniform gold particles.

Annealing experiments (Section 2.4.1) show that these spherical crystals, though metastable with respect to the polyhedral morphology, are in fact more stable than quasi-spherical gold nanostructures. We find that in the absence of etching reagents the nanospheres maintain their shape at temperatures up to 200 °C. At 250 °C,

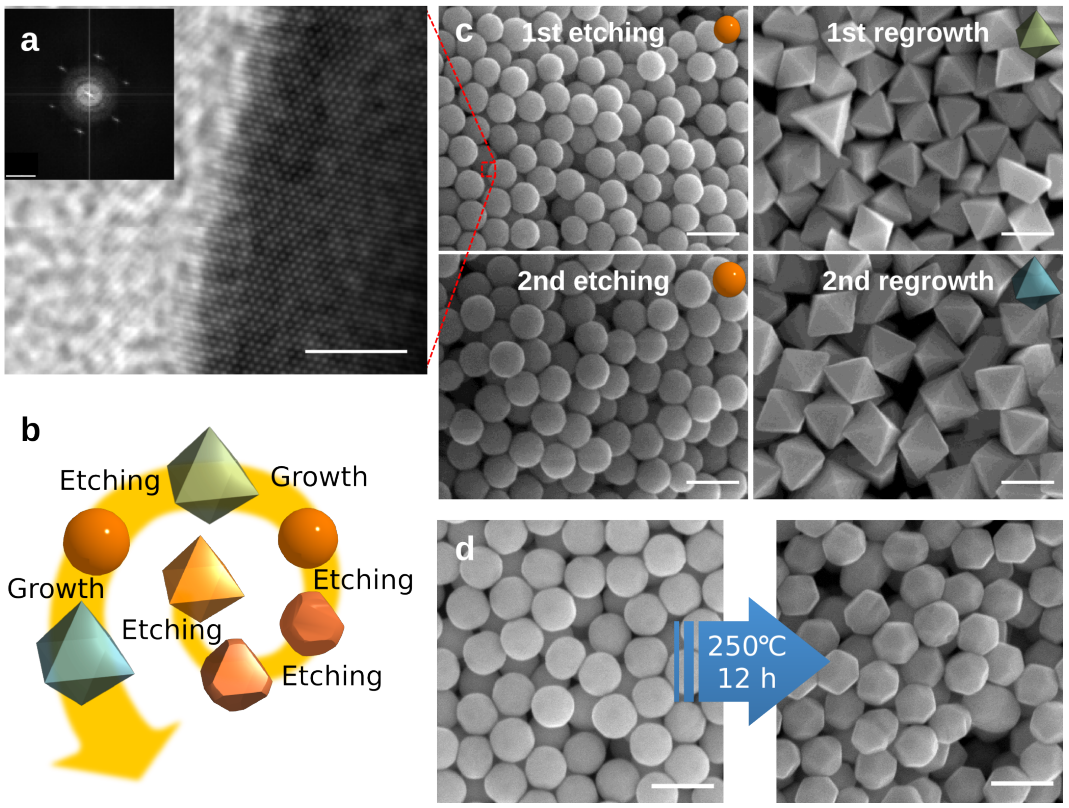

Figure 2.2: Nanospheres produced by growth and etching are single crystals that can be used as seeds for further growth. (a) High-resolution transmission electron micrograph of a gold nanosphere shows that the crystalline order extends to the edge of the particle. Scale bar is 2 nm. Inset shows the electron diffraction pattern. (b) Schematic diagram of iterated etching and regrowth of gold nanoparticles to produce large particles. (c) Scanning electron micrographs show particles after repeated etching and growth steps. Scale bars are 200 nm. (d) Scanning electron micrographs taken before and after annealing a sample of gold spheres at 250 °C in pentanediol for 12 h. Scale bars are 200 nm.

the particles start developing facets, as shown in Figure 2.2(d). In contrast, gold nanoshells melt at temperatures as low as 175 °C due to grain boundaries and fissures [50]. The enhanced stability suggests that the spherical crystals not only are monocrystalline but also have a low level of defects that might compromise thermal stability.

2.2.3 Circularity and Size Distribution

The other state-of-the-art particles for studies of plasmonic phenomena are quasi-spherical gold particles produced from citrate reduction of $HAuCl_4$ in water [47, 48]. These have been used in several recent experiments to study phenomena such as surface-enhanced Raman scattering [75], Fano resonances [66], nanoparticle-microcavity-based sensing [87], and quantum limits of plasmonic coupling [82]. However, we find that these particles are much less smooth and spherical than the nanospheres produced through growth and etching. We quantify these differences using image analyses of transmission electron micrographs (Figure 2.3).

Starting with a TEM image of a single nanoparticle, we use the software program ImageJ to threshold and filter the image. We then sample over all angles in the plane of the image to compute the maximum Feret's diameter (d_F) of the region representing the nanoparticle. This represents the longest line segment that can be drawn from one side of the particle to another. We define the "circularity" (c) of the particle as the ratio of its area (A) in the filtered image to the area of a circle whose diameter is equal to d_F, expressed in the equation $c = 4A/\pi d_F^2$. A perfectly circular particle corresponds to $c = 1$; the circularity decreases toward zero as the particle's

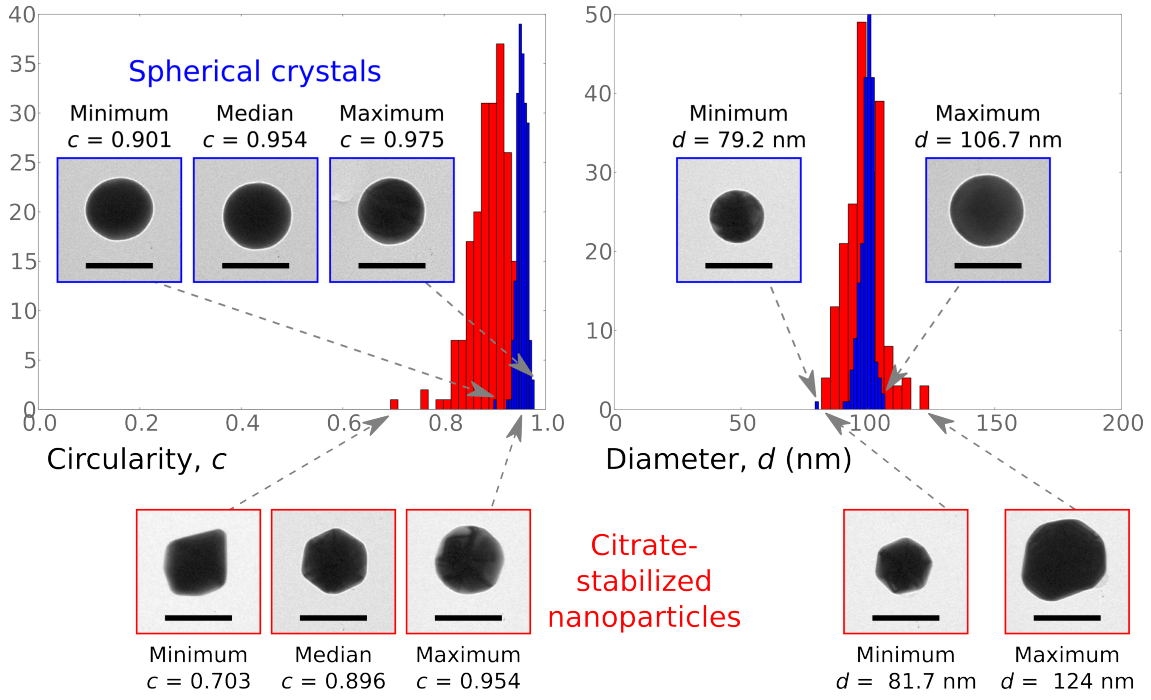

Figure 2.3: Distribution of circularity and diameter of spherical gold crystals (blue) and citrate-stabilized gold nanoparticles (red), as measured from TEM images of samples of 200 particles using image processing. A perfectly circular particle corresponds to $c = 1$; the circularity decreases toward zero as the particle's outline deviates from a circle. Insets show micrographs corresponding to key parts of each distribution. Scale bars are 100 nm.

outline deviates from a circle. From the area A that we measure in each image, we can also compute an average diameter of each particle, $d = (4A/\pi)^{1/2}$. From the distribution of d for each colloid, we can measure its polydispersity.

We measure c and d for equal numbers of gold nanospheres made through growth and etching and citrate-stabilized gold particles purchased from British Biocell International (BBI), which are prepared using a proprietary method based on the procedure developed by Turkevich *et al.* [47] As shown in Figure 2.3, the distributions of the circularity, c, and the diameter, d, for these particles are more than twice

as broad as they are for particles of comparable size from the growth and etching technique. The spherical crystals have an average diameter of 99.5 nm with a standard deviation of 2.9 nm. They are more monodisperse than a comparable sample of citrate-stabilized particles, whose average diameter is 98.8 nm with a standard deviation of 7.2 nm. Moreover, the median citrate-stabilized particle deviates from perfect circularity (1.000) more than twice as much as the median spherical crystal; the median circularity of the spherical crystals is 0.954 and that of the citrate-stabilized particles is 0.896.

2.2.4 Reproducible Scattering Spectra of Gold Nanospheres

The qualitative advances in particle uniformity, sphericity, smoothness, stability, and monocrystallinity afforded by the growth and etching technique [Figure 2.4(a)] enable the assembly of plasmonic structures with uniform and reproducible optical properties. We demonstrate this through several experiments examining the spectra of individual particles and assemblies thereof. To test the optical uniformity of the nanospheres, we record dark-field scattering spectra from individual particles deposited on a glass slide (Section 2.4.2), shown in Figure 2.4(b). We find that the standard deviation of the resonance peak wavelength for our spherical crystals is 5.7 nm, nearly 7 times smaller than that of commercial citrate-stabilized particles.

The nanospheres also show uniform spectra when their surface plasmons interact with those of a metal surface only 10 nm away. Unlike individual particles on a glass slide, this system enables us to probe higher-order plasmon modes in the context of coupling. We place the particles on a smooth gold film with an aluminum oxide

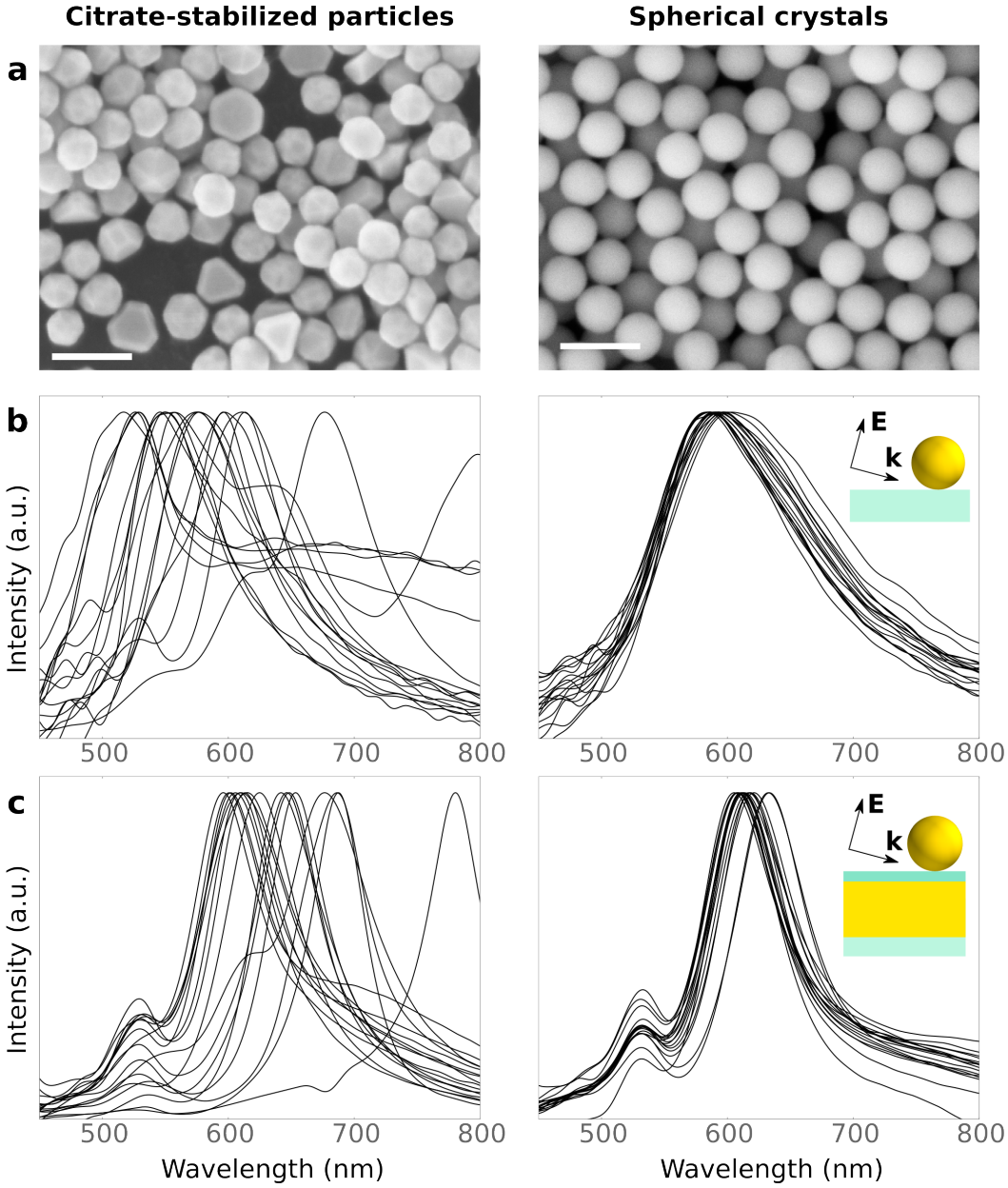

Figure 2.4: Reproducibility of gold nanoparticle scattering spectra. (a) Scanning electron micrographs of gold nanoparticles synthesized by citrate reduction or growth and etching. Scale bars are 200 nm. (b, c) Measured scattering spectra for citrate-stabilized nanoparticles and spherical crystals. Particles in (b) are on a glass slide and in (c) are on a gold film with a thin dielectric spacer. Insets show polarization and propagation direction of incident light.

spacer (Section 2.4.2) and measure their scattering spectra with p-polarized light at a 65° angle of incidence. In this geometry, the interaction results in a low-energy bonding mode and a higher energy antibonding mode, both of which are broadened due to the finite film thickness [88]. We find that for the nanospheres produced through growth and etching, the standard deviation in peak wavelength is nearly 6 times smaller than it is for citrate-stabilized particles of similar size [Figure 2.4(c)]. Furthermore, features like the smaller peak near 530 nm and the minimum near 550 nm are more reproducible for the spherical crystals than for the citrate-stabilized particles, some of which do not exhibit these features at all. For the spherical crystals, the wavelength of the small peak has a standard deviation of only 0.74 nm and may in fact be much smaller, as this value is comparable to the instrumental broadening of our spectrometer apparatus; for the citrate-stabilized particles the distribution is nearly 5 times as broad. The standard deviation of the ratio of the small peak intensity to the minimum intensity is 3.5 times larger for citrate-stabilized particles than for spherical crystals. Because the coupling that leads to these features depends sensitively on azimuthal symmetry and the distance between the particle and the gold film [88], the results suggest that nanospheres produced by growth and etching are round and smooth down to the nanometer scale.

2.2.5 Scattering Spectra of Quadrumer Cluster

To demonstrate that these particles may be used for self-assembly of artificial plasmonic molecules and other nanostructures showing complex coupling between plasmon modes, we prepare symmetric four-particle clusters ("quadrumers") on TEM

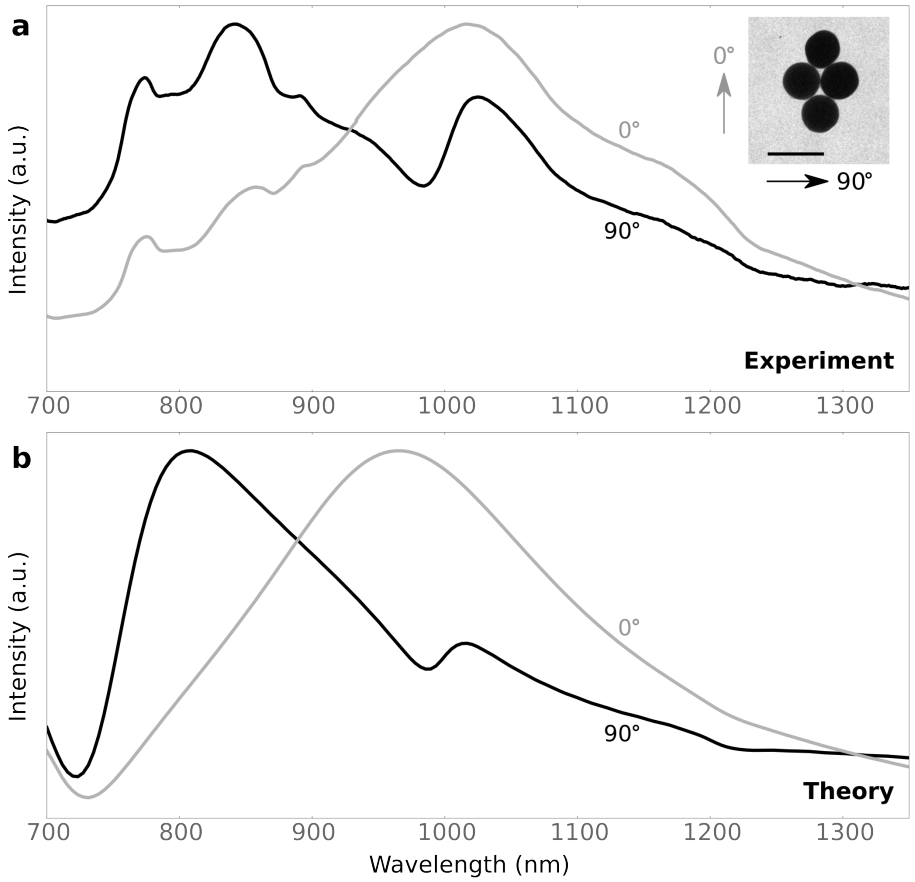

Figure 2.5: Scattering spectra of quadrumer cluster. (a) Experimental and (b) calculated near-normal incidence dark-field scattering spectra of a gold nanosphere quadrumer under long-axis (gray) and short-axis (black) polarization. Minima appear in both the experimental and calculated spectra near 980 nm when the polarization is parallel to the short axis of the quadrumer. We attribute this minimum to a Fano-like resonance because it occurs for only one polarization. Adsorption of organic molecules during the etching process results in a spacer on the order of 2 nm between the particles. Some discrepancies between the theoretical and experimental spectra at short wavelengths are likely due to scattering from other parts of the sample and have been observed in previous experiments [11, 12]. Inset shows a transmission electron micrograph of a quadrumer. Scale bar is 200 nm.

grids (Section 2.4.2) and measure their scattering spectra using near-normal incidence dark-field spectroscopy [89]. A narrow minimum appears in the spectrum near 980 nm when the polarization of the incident light is parallel to the quadrumer's short axis [Figure 2.5(a)]. The minimum disappears when the polarization is parallel to the quadrumer's long axis. These spectral features, characteristic of a Fano-like resonance [12], are in good agreement with calculated scattering spectra [Section 2.4.2 and Figure 2.5(b)] for a quadrumer modeled by uniform, spherical gold nanoparticles. The resonance results from interference between quadrupolar and higher-order modes of the nanoparticles [12]. This shows that the spherical nanocrystals can be used to fabricate plasmonic structures with similar properties to those made using gold nanoshells [11].

2.3 Conclusion

The method we have demonstrated to produce highly uniform, single-crystalline gold nanospheres can be used to address longstanding problems in the field of plasmonics. Particles on the order of 100 nm and larger are important for many applications because the scattering cross section exceeds the absorbance cross section for gold particles larger than 80 nm [34, 35]. The cyclic process we demonstrate can easily produce particles of 200 nm or larger, without the eccentricities and polydispersity typical of gold particles larger than 30 nm produced from established protocols. Indeed, conventional synthesis routes yield particles that are so heterogeneous that some groups have made use of the heterogeneity to fabricate asymmetric structures from a single batch of particles [66]. Furthermore, the high monodispersity of the

particles we demonstrate should facilitate the self-assembly of nanoparticle clusters with uniform linear or nonlinear optical resonances, which could in turn be used to fabricate optical metafluids [41] or to investigate enhanced optical four-wave mixing [90]. Narrow size distributions are required to control not only the spectral features but also the morphology and yield of clusters in certain assembly schemes [91]. A similar cyclic process of anisotropic growth followed by isotropic etching could be used to design spherical crystals of other metals, which might find uses as building blocks for optical sensors and circuits [75, 76], probes for biomedical applications [36, 92], nucleation sites for nanobubble generation [93, 94], and components for other applications in which smoothness, thermal stability, and uniformity of the optical response are critical.

2.4 Materials and Methods

2.4.1 Morphological Transformations

Chemicals

Ethylene glycol (anhydrous, 99.8%), gold(III) chloride trihydrate ($\geq$ 49.0% metals basis), poly(dimethyl diallyl ammonium chloride) (M_w 400 000 - 500 000, 20 wt% in H_2O), phosphoric acid (85 wt% in H_2O), chloroplatinic acid hydrate (99.995% metals basis), ethanol ($\geq$ 99.5%), hexadecyltrimethylammonium bromide ($\geq$ 99.0%), sodium dodecyl sulfate (92.5 - 100.5%), and polyvinylpyrrolidone (M_w 55 000) were purchased from Aldrich and used without further purification.

Synthesis of Octahedral Gold Particles

Octahedral particles were synthesized by a modified polyol process as described in a previous report by Li, *et al* [63]. When we used hydrochloric acid, we always found octahedral particles smaller than 100 nm, and we also found many byproducts from the reaction, including dodecahedra and trigonal plates. We tested several different acids and we found that phosphoric acid produced larger octahedral particles ($>$ 100 nm) with the fewest impurities. The exact reason for the better results with phosphoric acid is not clearly understood.

A 20 mL anhydrous ethylene glycol solution was stirred with a magnetic bar in a glass vial, and then 0.4 mL of polyDADMAC (20 wt% in H_2O, M_w 400 000 - 500 000) and 0.8 mL of 1 M H_3PO_4 solution were added. The mixture was stirred for 2 more minutes, and 0.02 mL of a 0.5 M $HAuCl_4$ aqueous solution was added under stirring. The mixture was maintained at room temperature for 15 min, and then the solution in the glass vial was loaded into an oil bath for 30 min, which was maintained at 195 °C throughout the reaction. During the reaction, the color of the solution changed from yellow to colorless and then, gradually, to purple and finally brown. We centrifuged the solution at 13 000 rpm and redispersed the precipitates in ethanol three times to remove the excess reactants and byproducts.

Etching Octahedral Particles to Form Spheres

To convert the octahedral gold nanoparticles to gold nanospheres, 5 μL of a 0.5 M $HAuCl_4$ solution was added into the unwashed gold octahedra suspension (20 mL, 8.9×10^{-3} wt%) at room temperature. The color of the suspension changed from

brown to pink. The size of the gold nanocrystals decreased from 135.4 ± 12.5 nm to 112.3 ± 8.2 nm over 20 h, and the particles evolved from octahedra to spheres.

At room temperature, ethylene glycol no longer behaves as a reducing agent, so growth of the nanocrystals is suppressed and the addition of chloroauric acid initiates an etching reaction. This etching process is driven by redox reactions and the concentration of $HAuCl_4$ controls the etching rate. To investigate this, we added three different amounts of chloroauric acid to equal volumes of unwashed octahedral particles. We found that decreasing the concentration of chloroauric acid slows the etching rate over the 20 h period.

To investigate whether there was another adjuvant that played a critical role in etching the gold octahedral particles, we tested the chemical ingredients used in our experiments. Only the mixture of $HAuCl_4$, polyDADMAC, and gold octahedral particles suspended in ethylene glycol exhibited a color change to orange [Figure 2.6(a)], accompanied by the transformation of the octahedra into spheres [Figure 2.6(b)-(g)]. PolyDADMAC may form a complex with $AuCl_2^-$ when Au from the octahedral particles is oxidized. Consequently, the removal of gold atoms from the octahedra continues as the product of this reversible reaction is steadily removed. It is well known that complexation of $AuCl_4^-$ and $AuCl_2^-$ with a surfactant facilitates oxidation of Au^0, although the standard oxidation potentials of Au^0 to $AuCl_4^-$ and $AuCl_2^-$ are large negative values (respectively -1.002 and -1.154 V, versus a normal hydrogen electrode) and the equilibrium constant for reaction 2.1 is very low [95].

$$AuCl_4^- + 2Au^0 + 2Cl^- \longleftrightarrow 3AuCl_2^-, K = 1.9 \times 10^{-8} \tag{2.1}$$

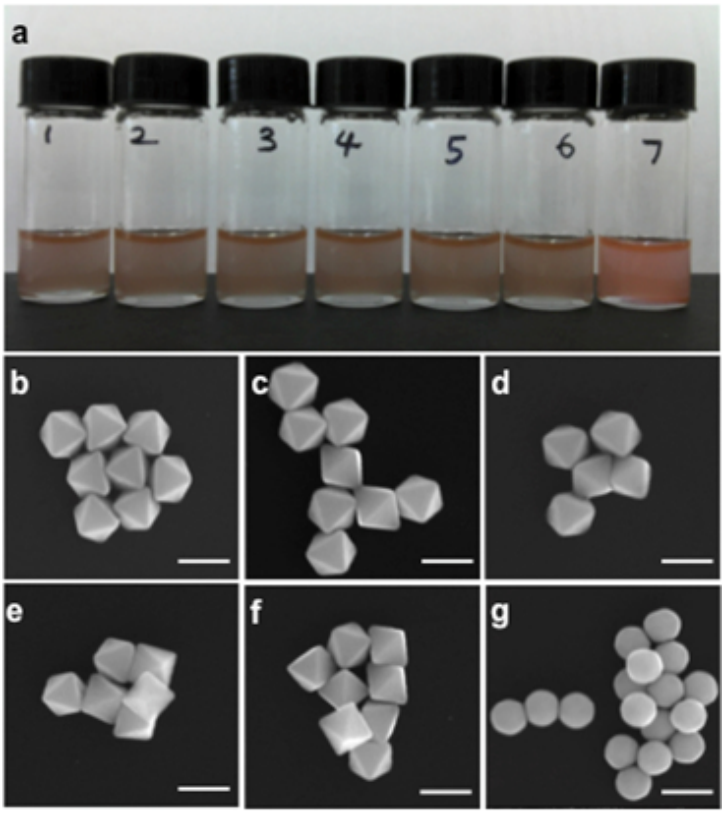

Figure 2.6: (a) Photographs of (1) the Au octahedron colloid solution before etching (20 mL, 8.9×10^{-3} wt%), and with the addition of (2) polyDADMAC (20 wt%, 0.4 mL); (3) H_3PO_4 (1 M, 0.8 mL); (4) $HAuCl_4$ (0.5 M, 5 μL); (5) polyDADMAC and H_3PO_4; (6) H_3PO_4 and $HAuCl_4$; or (7) polyDADMAC and $HAuCl_4$. SEM images of gold particles from a suspension (20 mL, 8.9×10^{-3} wt%) after adding (b) polyDADMAC aqueous solution (20 wt% in H_2O, 0.4 mL); (c) H_3PO_4 aqueous solution (1 M, 0.8 mL); (d) $HAuCl_4$ (0.5 M, 5 μL) aqueous solution; (e) polyDADMAC and H_3PO_4; (f) H_3PO_4 and $HAuCl_4$; or (g) polyDADMAC and $HAuCl_4$. Scale bars are 200 nm.

This suggests that the etching rate may depend on the quantity of polyDADMAC added. In control experiments, we added only 1/10 or 1/100 of the normal amount of polyDADMAC solution to the gold octahedron suspension, waited 20 hours as usual, and observed larger, less smooth Au particles (Figure 2.7). This indicates that less

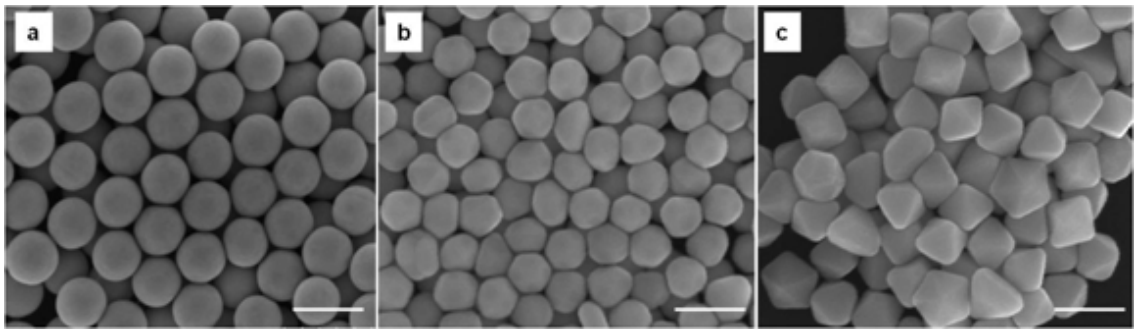

Figure 2.7: SEM images of Au particles after the addition of $HAuCl_4$ (0.5 M, 5 μL) and (a) 400 μL, (b) 40 μL, or (c) 4 μL of polyDADMAC into the washed gold suspension for a reaction time of 20 h. Scale bar: 200 nm.

etching occurs when less polyDADMAC is added. We tested other surfactants in addition to polyDADMAC and the results are shown in Figure 2.8. Cetyltrimethyl ammonium bromide (CTAB, a cationic surfactant) was effective in the chemical etching process but sodium dodecyl sulfate (SDS, an anionic surfactant) and polyvinylpyrrolidone (PVP, a nonionic surfactant) were not. CTAB may form complexes with gold chloride anions, however, as has already been reported in previous articles [96, 97]. Moreover, because of the relatively high viscosity of ethylene glycol, the particles were stable against sedimentation and ions presumably diffused slowly, which made

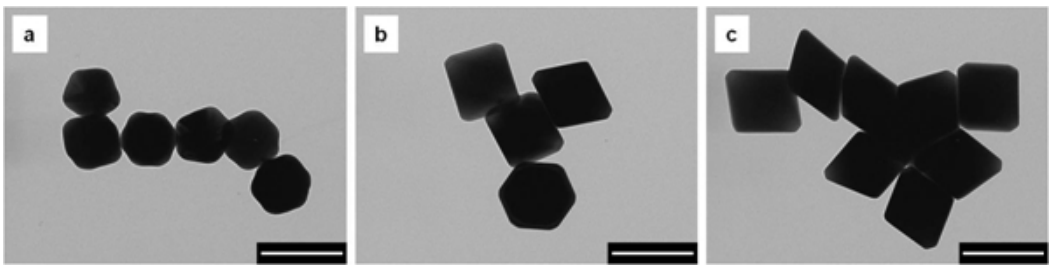

Figure 2.8: TEM images of Au colloids after the addition of $HAuCl_4$ (0.5 M, 5 μL) and (a) CTAB (20 wt% in H_2O, 0.4 mL), (b) SDS (20 wt% in H_2O, 0.4 mL), or (c) PVP (20 wt% in H_2O, 0.4 mL) to the Au octahedron suspension. Scale bar: 200 nm.

it possible to control the extent and uniformity of chemical etching.

To investigate the etching rate's dependence on chloroauric acid, we tested three different amounts of chloroauric acid with the same quantity of polyDADMAC (0.4 mL). We found that decreasing the concentration of gold salt slowed the etching rate over the 20 h period. We determined the particle sizes as functions of reaction time from measurements of SEM images of samples taken at different times during the experiment (Figure 2.9). In all cases, the particle size decreased abruptly at first and then saturated as the oxidation-reduction reaction approached equilibrium and the chemical potential difference vanished.

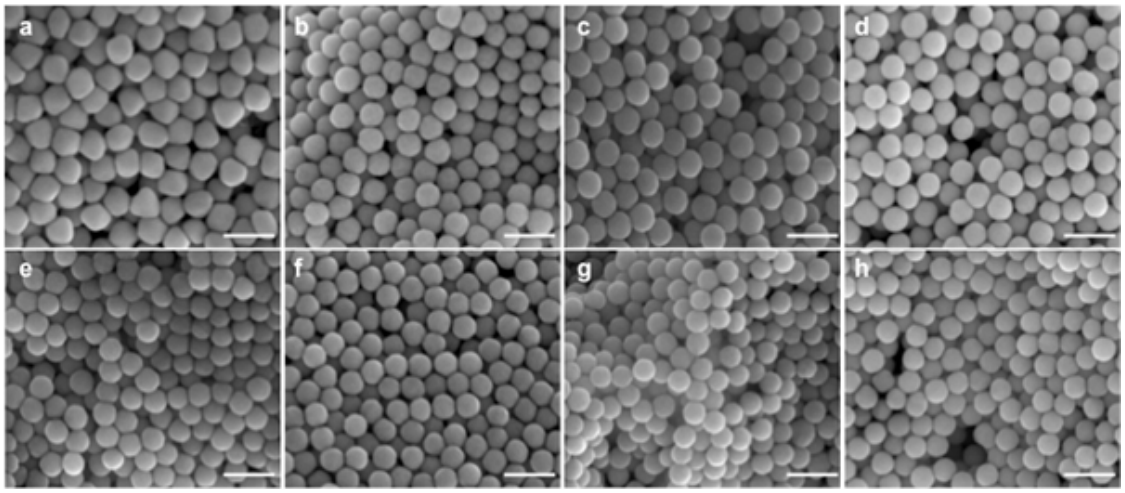

Figure 2.9: SEM images of the gold nanocrystals (a) 30 min., (b) 3 h, (c) 6 h, and (d) 10 h after the etching reaction began with 10 μL gold precursor. And SEM images of the gold nanocrystals (e) 30 min., (f) 1 h, (g) 3 h, and (h) 6 h after the etching reaction began with 15 μL gold precursor. Scale bars are 200 nm.

To understand how the different initial nanocrystal morphologies transformed during the etching reaction, we used SEM to observe samples of the mixture from various times throughout the etching process. The octahedral particles transformed into

spheres through etching fastest (Figure 2.10). The truncated triangular bipyramids changed shape at a slower rate but they all eventually became spheres. The final gold spheres are uniform in size and shape regardless of the seed particles' shapes.

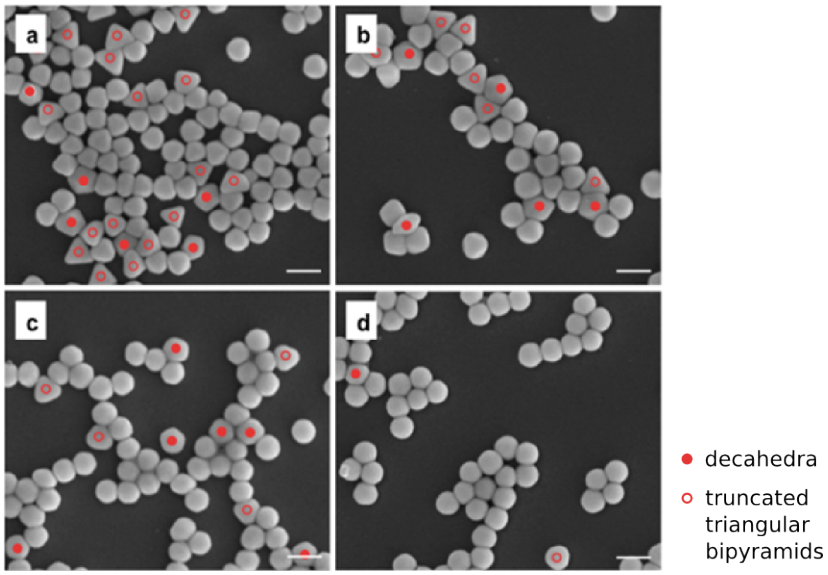

Figure 2.10: SEM images of the gold nanocrystals (a) 3 min., (b) 6 min., (c) 50 min., and (d) 4 h after the etching reaction began with 5 μL gold precursor. Scale bars are 200 nm.

X-ray diffraction (XRD) patterns in Figure 2.11 reveal that the {111} facet is dominant for the gold octahedron, in agreement with observations by other groups [63, 98]. Other crystal planes including {200}, {220}, and {311}, consistent with the standard spectrum of fcc gold (JCPDS no. 89-3697), are also exposed at surfaces during the chemical etching process.

Iterative Growth and Etching

In one experiment, we used our spherical gold crystals as seeds for octahedral re-growth. The unwashed gold sphere suspension in a glass vial was loaded into an

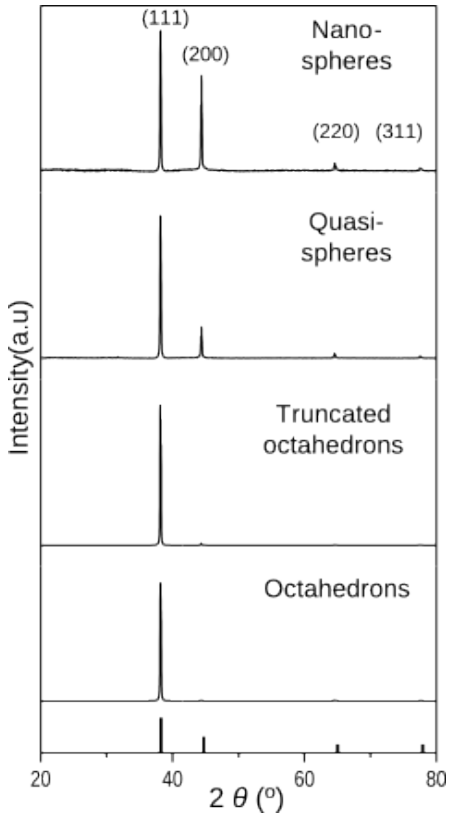

Figure 2.11: XRD patterns of gold structures from octahedron to truncated octahedron, quasi-sphere, and sphere. The standard XRD patterns for fcc gold (JCPDS no. 89-3697) are shown as a bar diagram at bottom.

oil bath at 195 °C for 1 h. We started with 112.3 ± 8.2 nm gold spheres in suspension with the 5 μL of chloroauric acid that had previously been added for etching. After the first regrowth, we obtained octahedral particles of edge length 156 ± 13.8 nm.

We initiated another etching reaction using these re-grown octahedral particles by adding 5 μL of chloroauric acid. We found that these too transformed into spheres. The resulting spheres were larger (131.2 ± 9.5 nm) than the original seed spheres we had obtained after 20 h. We produced larger octahedral gold particles in a third growth step, and as we continued this procedure, we obtained larger smooth gold oc-

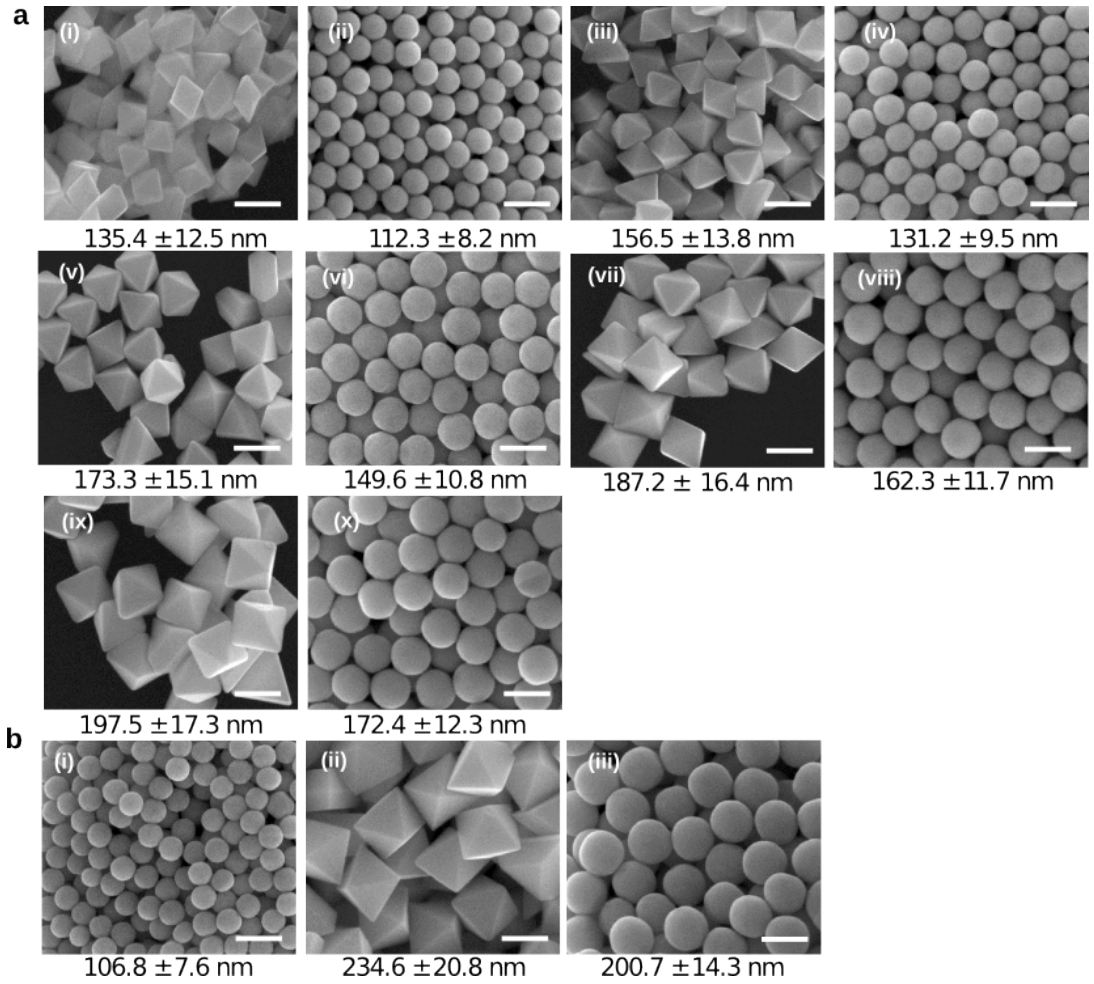

Figure 2.12: Iterative growth and etching of gold octahedra. a, (i-x) SEM images of gold octahedra and nanospheres after iterative growth and etching with addition of 5 μL aqueous $HAuCl_4$ solution. (i) initial growth, (ii) 1st etching, (iii) 1st regrowth, (iv) 2nd etching, (v) 2nd regrowth, (vi) 3rd etching, (vii) 3rd regrowth, (viii) 4th etching, (ix) 4th regrowth, (x) 5th etching. b, With the addition of 20 μL of 0.5 M aqueous $HAuCl_4$ solution, (i) smaller gold nanospheres and (ii) larger gold octahedra were produced from 197.5 nm gold octahedra shown in a(ix) and then (iii) 200.7 nm gold nanospheres were produced by etching 234.6 nm gold nanospheres in b(ii) with the addition of 5 μL of 0.5 M aqueous $HAuCl_4$ solution. Average particle sizes refer to edge length for octahedra and diameters for spheres. Scale bars are 200 nm.

tahedra after each successive iteration. Electron micrographs of the resulting spheres and octahedra after successive iterations are shown in Figure 2.12.

Transformation Back to Polyhedra at High Temperature

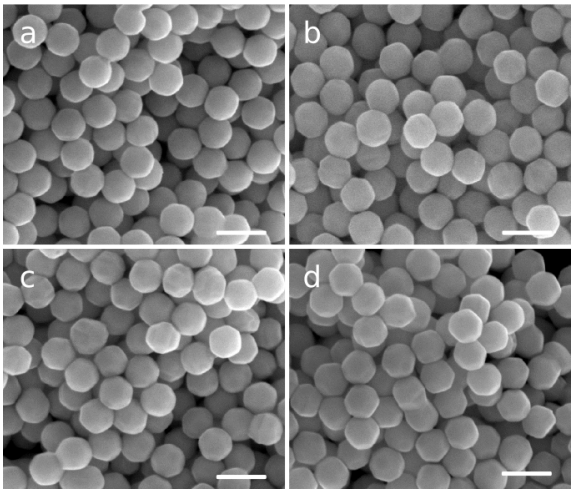

Figure 2.13: SEM images of Au particles after the solvo-thermal process in 1,5-pentanediol at 250 °C for a total reaction time of (a) 5 min, (b) 10 min, (c) 15 min, and (d) 30 min. Scale bars are 200 nm.

We conducted an annealing experiment to test the stability of our gold nanospheres in the absence of the etching reaction. We washed a batch of spherical gold crystals more than 10 times in ethanol and redispersed them in 1,5-pentanediol. We then heated the mixture to just below the boiling point of pentanediol (250 °C) for half an hour. We found that under these conditions, the particles gradually transform back to polyhedra, as shown in Figure 2.13. Facets begin to form on the particles in less than 30 minutes. After 12 hours, the particles show significant faceting and some of them have merged together as dimers. Many of them appear to have adopted a truncated octahedral morphology, in agreement with predicted shape transformations prior to

melting [99]. This implies that increased mobility at the crystal surface at 250 °C is sufficient to transform the particles to a faceted morphology. In a similar experiment, we washed and redispersed gold nanospheres in ethylene glycol and heated the suspension nearly to its boiling point (200 °C) for 12 hours. These particles showed no evidence of morphological transformation.

Comparison to Citrate-Stabilized Gold Nanoparticles

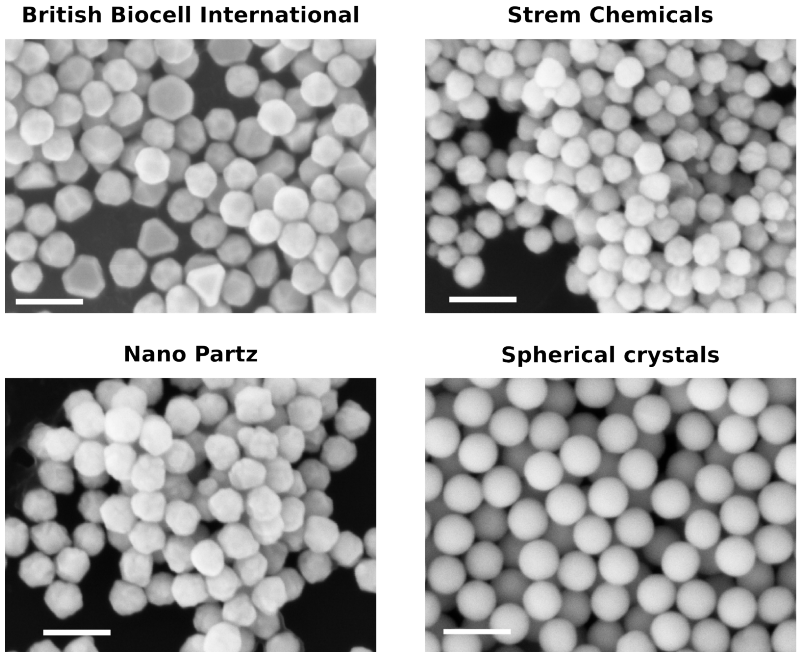

Figure 2.14: Scanning electron micrographs of gold nanoparticles purchased from various suppliers and as prepared with our growth and etching technique. Scale bars are 200 nm.

Citrate-stabilized gold nanoparticles were purchased from British Biocell International or BBI (100 nm), Strem Chemicals (90 nm), and Nano Partz (100 nm). Inspection of the particles with scanning electron microscopy (Figure 2.14) revealed that all three colloids consisted of faceted or lumpy particles which were not all the same size.

Qualitatively, these micrographs show that these conventional gold nanoparticles are not perfectly spherical or monodisperse. We used one of these colloids (BBI, 100 nm diameter) for more thorough quantitative comparison with the spherical gold crystals.

Monte Carlo Simulation of Chemical Etching

Starting with an octahedral nanoparticle defined in a space of fcc lattice sites, we calculate the energy of each atom based on its coordination number using the embedded atom method [86]. We then proceed with a grand canonical Metropolis algorithm [100, 101, 102] to select lattice sites at the surface of the crystal for either the insertion or removal of one atom at a time. The probability of insertion is determined from the change in free energy that would result,

$$W_{n\to n+1} = \min\left(1, \frac{V_{\mathrm{acc}}}{X\Lambda^3\,(n+1)} \mathrm{e}^{\left(\mu - \frac{\Delta E_{n+1,n}}{k_{\mathrm{B}}T}\right)}\right) \tag{2.2}$$

similar to the method explained in a previous study [102], with a few differences. In equation 2.2, n is the number of atoms in the nanocrystal and Λ is the thermal wavelength, given by $\left(\frac{h}{2\pi m k_{\mathrm{B}} T}\right)$. The volume where particles can be created V_{acc} is given by the number of occupied and unoccupied lattice sites with coordination number $C_{\mathrm{N}} > 0$ multiplied by the volume of a gold atom, $\left(\frac{4}{3}\pi r_{\mathrm{Au}}^3\right)$. Thus it includes not only the volume of the crystal itself but also the volume of a surface layer of lattice sites where an atom could be inserted such that it would form at least one bond with another atom already in the crystal. The chemical potential is calculated from $\mu = RT \ln a_{\mathrm{M}}$, where the activity a_{M} is taken as the initial concentration of chloroauric acid added to start the reaction. Molecules in solution at and outside the

surface of the nanocrystal are not modeled.

One difference between the present algorithm and the previous study [102] is that the change in energy due to the insertion of an atom, $\Delta E_{n+1,n}$, includes not only the decrease in energy from forming bonds with other atoms but also an energy increase of 3.700 eV due to the etching reaction. This value is the difference between the reduction potential (-0.228 eV) of reaction 2.1, calculated from reduction potentials for half-reactions reported elsewhere [96], and the binding energy of the atoms in the bulk of the crystal with $C_{\mathrm{N}} = 12$, which is -3.928 eV according to embedded atom method calculations.

Another difference in the present algorithm is that the probability is normalized by dividing by a large constant, X, chosen throughout the present study to be 10^9. This has the effect of slowing the entire simulation down, while introducing a preference for the insertion or removal of atoms at sites where the change results in a larger decrease in the system's free energy. We include this factor so that we can observe which areas of the crystal are modified first preferentially. This modification to the standard grand canonical Metropolis algorithm is acceptable because it should have no effect on the equilibrium state to which the simulation converges. We are not primarily interested in the equilibrium state anyway, which in this case is the dissolution of the crystal entirely. Instead, we are interested in how the system gradually changes as it slowly equilibrates. In our experiments we have to terminate the etching reaction after a certain period of time and we observe that the nanospheres continue to shrink as long as the reactants are present, so we do not assume that the system in fact reaches an equilibrium state.

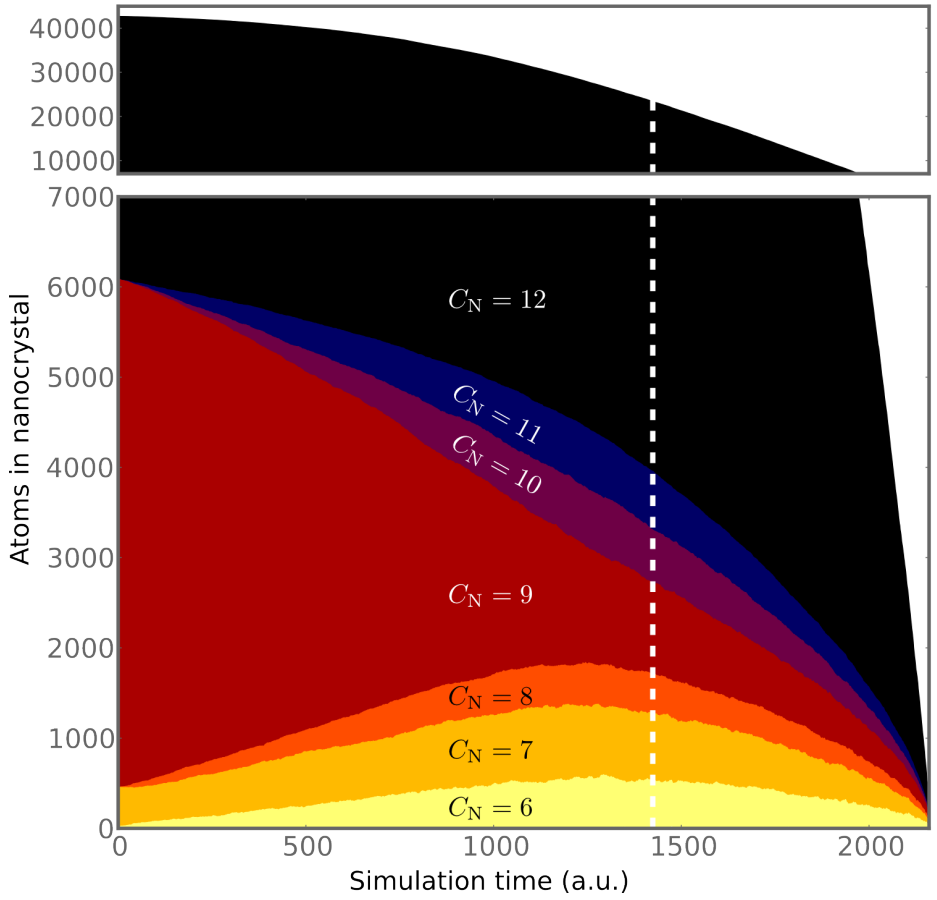

Figure 2.15: Number of atoms in a model octahedral nanocrystal as a function of etching simulation run time, color-coded by coordination number, C_N. The edge length is initially 40 atoms, or 42 680 atoms total. The percentage of atoms with $C_N < 6$ is negligible. The dashed white line marks the point when original faces of the octahedron have been completely removed. Until the very end of the simulation the majority of atoms are in the interior of the crystal with $C_N = 12$.

The probability of removal of an atom from the crystal is calculated similarly:

$$W_{n\to n-1} = \min\left(1, \frac{\Lambda^3 n}{X V_{\text{acc}}} \mathrm{e}^{\left(-\mu - \frac{\Delta E_{n-1,n}}{k_{\text{B}} T}\right)}\right) \tag{2.3}$$

where in this case $X = 10^9$ as before and $\Delta E_{n-1,n}$ represents the increase in energy due to breaking bonds between atoms by removing an atom from the crystal, plus a decrease in energy of 3.700 eV due to the chemical reaction.

We start with an octahedron of edge length 40 atoms for a total of 42 680 atoms. The vertices are removed first, followed by the edges, and then the crystal gradually becomes more and more spherical as the original facets are slowly removed. This is reflected in Figure 2.15, which shows how the number of atoms with different coordination numbers C_{N} changes over the course of the simulation. Initially there are many atoms with $C_{\text{N}} = 9$ on the faces of the octahedron and this number gradually diminishes as the faces are slowly removed. It takes roughly 10 million attempts at insertion or removal of atoms before all the atoms are etched away; the vast majority of attempts result in no change to the crystal at all. The simulation is this slow due to our large probability suppression factor, X.

2.4.2 Optical Properties of Gold Nanospheres

Preparation of Nanoparticles on a Glass Slide

We prepared samples for spectroscopy measurements by drying a droplet of dilute gold nanosphere suspension on a glass slide. The slide was treated with oxygen plasma at 60 W for 10 s to make the surface more hydrophilic. Immediately afterward

we placed onto the slide a droplet of gold nanosphere suspension that had been sonicated for at least 1 min in a bath sonicator. We measured spectra from individual particles after the droplet dried in air. Both the spherical crystals and the citrate-stabilized particles were deposited on the same glass slide for dark-field spectroscopy measurements. Scanning electron microscopy confirmed that the vast majority of particles on the sample were well-dispersed, sitting several micrometers apart rather than occurring in clusters.

Preparation of Particles on Gold Film Separated by a Dielectric Layer

We prepared samples by drying a droplet of dilute gold nanosphere suspension on a substrate consisting of a thin Al_2O_3 layer on top of a template-stripped gold film supported on a glass slide. To prepare the substrate, we first deposited 120 nm of gold onto a cleaned silicon wafer with electron beam evaporation. Then we placed a small drop of UV-curable epoxy (Norland Optical Adhesive 65 from Thorlabs, Inc.) on top of the gold film and put a glass slide on top before curing it under a UV lamp for 20 min. The wafer was stripped off of the film so that the film could be transferred entirely to the glass slide but retain a wafer-smooth surface. Next, 10 nm of Al_2O_3 was deposited onto the exposed surface of the gold film using atomic layer deposition. We treated the Al_2O_3 surface with oxygen plasma at 60 W for 10 s to make the surface more hydrophilic and then immediately placed a droplet of gold nanosphere suspension on it. We let the droplet air dry and then measured scattering spectra of individual particles on the film.

Self-Assembly of Plasmonic Clusters and Dark-Field Spectroscopy

We prepare gold nanoparticle quadrumers by drying a droplet of dilute gold nanosphere suspension on a London finder Formvar TEM grid (LF200), purchased from Ted Pella. We place 2 μL droplets of gold nanosphere colloid on the grids and let them air dry. Some of the particles assemble into clusters on the Formvar surface due to capillary forces while drying [11]. We locate individual clusters on the grid using a Zeiss Libra 120 TEM operating at 60 keV and we record micrographs at different magnifications so that the clusters can later be located (using the London finder grid pattern) for dark-field spectroscopy [11]. We conduct near-normal incidence dark-field spectroscopy as described by Fan *et al.* [89].

FDTD Simulations of Scattering Spectra

To calculate the quadrumer's scattering spectra we conducted finite-difference time-domain (FDTD) simulations with a total-field scattered-field implementation [103] using the commercial software package Lumerical, version 6.5.11. We simulated two different polarizations for the incident light. Our simulation volume was 1 μm × 1.3 μm × 0.5 μm and our mesh for FDTD calculations consisted of 1 nm^3 cubes. The grid boundaries in the simulation space were perfectly matching layers (PML).

Within this volume our model quadrumer is based on measurements of the experimental system's geometry. We simulated particles of diameter 130 nm, corresponding to measurements of our experimental quadrumer that we obtained with transmission electron microscopy. The simulated particles have optical properties of gold, following the Johnson and Christy standard [4]. The simulated particles are embedded in a

dielectric elliptical disc of major axis 174 nm, minor axis 126 nm, and depth 60 nm. The refractive index of this disc is 1.45. The particles embedded in this disc are separated from each other by gaps of 1.5 nm. The Formvar substrate is not modeled in the simulation. The simulated particles are large enough compared to the mesh size that surfaces in the simulation are relatively smooth. We verified that this mesh size was adequate by checking that the simulations converged in the near-infrared spectral region of interest even as we fine-tuned the mesh size. The simulated quadrumer, as rendered by Lumerical, can be seen in Figure 2.16.

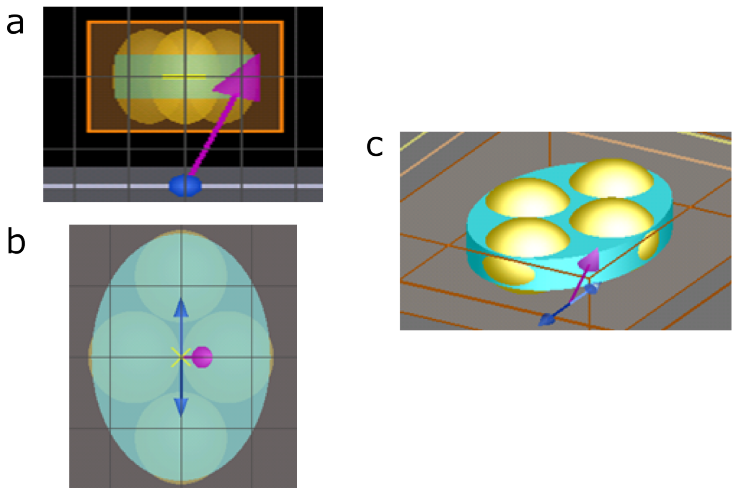

Figure 2.16: Rendering of a model quadrumer used for FDTD simulations, as viewed (a) along the major axis, (b) perpendicular to the plane of the axes, and (c) at an angle. Gold spheres of diameter 130 nm are embedded in an elliptical disc of constant refractive index 1.45 (blue). Purple arrow indicates propagation direction of incident light and dark blue arrows indicate electric field orientation for 0° polarization.

An electromagnetic plane wave pulse is introduced, corresponding to a 700 nm - 1400 nm wavelength range. This plane wave propagates in a direction indicated by the purple arrow in Figure 2.16 for an angle of incidence of 20°, approximately the same angle of incidence that we used in the near-normal incidence dark-field

spectroscopy technique. We obtained the scattering spectrum by collecting the power in the scattered field from a cone with a numerical aperture of 0.65, situated on the same side of the source as the spectrometer in our experimental system.

Differences Between Experiment and Simulation

There are differences between the calculated and measured spectra of the quadrumer, especially at wavelengths shorter than about 900 nm. As discussed by Fan *et al.* [11], these discrepancies arise due to scattering from parts of the sample that are not modeled in the simulation. This includes interactions between the cluster and the thin Formvar substrate as well as scattering from other particles or TEM grid bars that are close to the quadrumer.

Another reason for differences between the simulated and experimental scattering spectra is inhomogeneous changes in the Formvar substrate due to beam damage from the TEM that is used to locate the cluster. TEM images of quadrumers that have already been imaged at higher magnification show circular patterns of beam damage, as shown in Figure 2.17. The electron beam can warp the Formvar or even puncture it. Combined with local heating from the metal nanoparticles, this may result in inhomogeneous variations in the substrate geometry or even the contact angle between the substrate and the nanoparticles. Beam damage to the substrate may result in variations in its refractive index that are not captured in the simulations either.

A layer of material is observed surrounding the nanoparticles in a cluster under TEM. It is unclear whether this is a consequence of beam damage or simply material

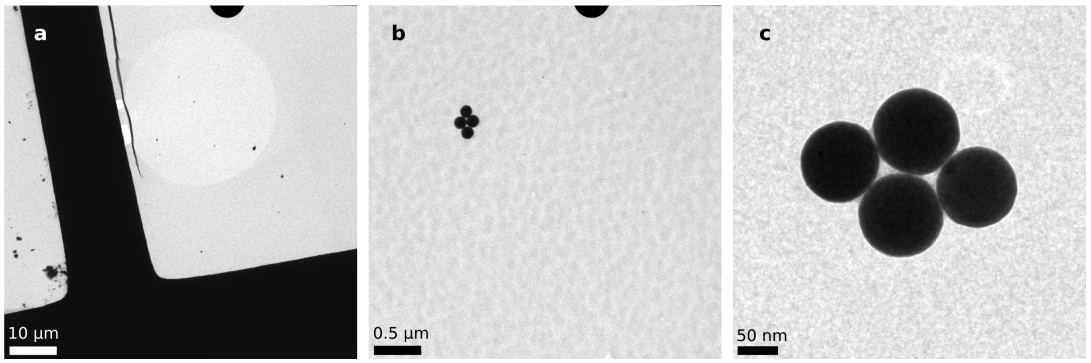

Figure 2.17: Transmission electron micrographs of quadrumer clusters of spherical gold crystals. (a) A low magnification image shows evidence of beam damage due to previous high magnification work on the same part of the sample. There is a circular region of beam damage which appears brighter in the image and a dark crease in the Formvar running parallel to a grid bar. (b) Higher magnification image of a quadrumer reveals the inhomogeneous nature of the Formvar substrate over a length scale of 100 nm. (c) High magnification image of a quadrumer shows material in the gaps between the particles, which causes the edges of the particles at the center of the cluster to appear blurry.

that adsorbs to the particles during or before TEM sample preparation. The elliptical disc of dielectric material in the simulation is meant to model this layer, but its refractive index is treated as a fitting parameter. Our simulation models neither the exact morphology of this layer nor potentially inhomogeneous variations in the refractive index within it.

Chapter 3

Tetrahedral Colloidal Clusters from Random Parking of Bidisperse Spheres

3.1 Introduction

Understanding the geometry of clusters formed from small particles is a fundamental problem in condensed matter physics, with implications for phenomena ranging from nucleation [104] to self-assembly [51]. Colloidal particles are a useful experimental system for studying cluster geometry and its relation to phase behavior [105] for several reasons: they are large enough to be directly observed using optical mi-

croscopy; their assembly can be understood in terms of geometry [106, 107]; and they can be driven to cluster by a variety of controllable interactions, including capillary forces [51], depletion [108], fluctuation-induced forces [109], or DNA-mediated attraction [110]. Colloidal clusters are also useful materials in their own right. They can be used, for example, as building blocks for isotropic optical metamaterials known as metafluids [41, 37, 11]. Tetrahedral clusters are of particular interest for metafluids since the tetrahedron is the simplest cluster with isotropic dipolar symmetry [41]. An unsolved challenge for this application is to determine the interactions and conditions that enable assembly of bulk quantities of highly symmetric, uniform clusters such as tetrahedra.

With this motivation in mind, we study experimentally the geometry and size distribution of binary clusters formed when small colloidal spheres are mixed with an excess of large spheres that stick *irreversibly and randomly* to their surfaces (Figure 3.1). An obvious way to control the cluster geometry in such binary systems is to vary the size ratio. One might expect that at certain ratios the particles could arrange into dense clusters or "spherical packings" – arrangements of spheres around a central

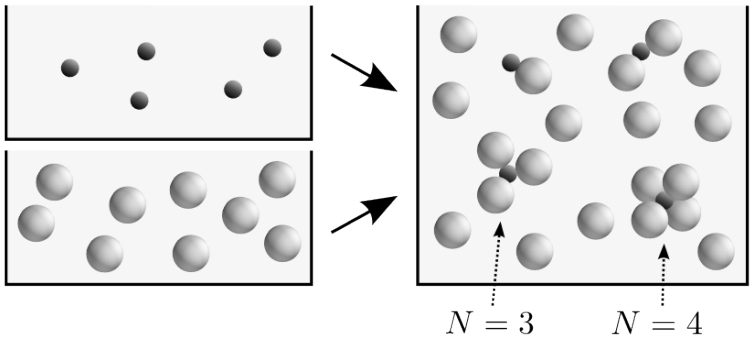

Figure 3.1: Two colloidal sphere species are mixed together to form clusters.

sphere that maximize surface density [111, 112, 113]. Such packings have long been used in modeling the microstructure of dense, disordered atomic systems [114, 115]. But unlike atoms, colloidal particles can stick irreversibly, such that two particles bound to a third show no motion relative to one another. This type of binding occurs frequently in strongly interacting, monodisperse colloidal suspensions, which consequently form fractal aggregates instead of dense glasses [116, 117]. Similarly, in the binary systems we study, the irreversible and stochastic process of sticking precludes the formation of dense or symmetric packings. The large spheres *park*, rather than pack, on the surfaces of the small spheres.

3.2 Results and Discussion

3.2.1 Experimental Results

Surprisingly, this random and nonequilibrium process can produce clusters of uniform size. Our experiments show that at a size ratio $\alpha = R_{\text{large}}/R_{\text{small}} = 2.45$, where R_{large} and R_{small} are the sphere radii, nearly all of the clusters contain four large spheres stuck to a smaller sphere (Table 3.1). In these experiments we use a 100:1 stoichiometric ratio of the two sphere species, statistically ensuring that each cluster contains only one small sphere surrounded by two or more larger spheres. After waiting several days for the average cluster size to saturate, we measure the distribution of N, the number of large spheres bound to each small sphere. (See Section 3.4.3 for details.) We do not include single large spheres, non-specifically aggregated clusters of large spheres, or clusters with multiple small spheres. While there are many iso-

Table 3.1: Experimentally observed cluster size distributions for charged colloids. Percentages of total are listed. The distribution for $\alpha = 2.45$ (bold) is sharply peaked at $N = 4$.

Size ratio α	1.94	**2.45**	3.06	4.29
$N = 6$	6.3	**0.0**	0.0	0.0
$N = 5$	39.2	**0.8**	0.0	0.0
$N = 4$	54.4	**90.2**	18.6	0.7
$N = 3$	0.0	**6.6**	69.9	35.9
$N = 2$	0.0	**0.8**	10.9	51.0
$N = 1$	0.0	**0.8**	0.6	11.1
$N = 0$	0.0	**0.8**	0.0	1.3

lated large spheres due to the high stoichiometric ratio, the latter two types of cluster are rare.

The $N = 4$ tetramers that we observe are not dense packings or, in general, symmetric arrangements. As can be seen from the images in Figure 3.2, there is space between the large particles, and the resulting tetrahedra are irregular. Moreover, the ratio $\alpha = 2.45$ is well below the value $\alpha = 4.44$ found by Miracle *et al.* [118] for efficient tetrahedral packing in binary atomic clusters. In fact, at $\alpha = 4.29$, closer to this bound, we see much smaller clusters and few tetrahedra. The sparsity of large spheres in the clusters is a result of the irreversible, nonequilibrium, random binding: once the big particles stick to the smaller ones, we do not see them detach or move relative to one another. We expected such a stochastic process to lead to a much broader distribution of clusters. At other values of α it does (Table 3.1), but at $\alpha = 2.45$ we obtain 90% tetramers.

The high yield of tetramers occurs in two experimental systems with different types of interactions. In both systems the interactions are specific, strong, and short-ranged, and the particles do not rearrange once bound. In the first system the clustering is

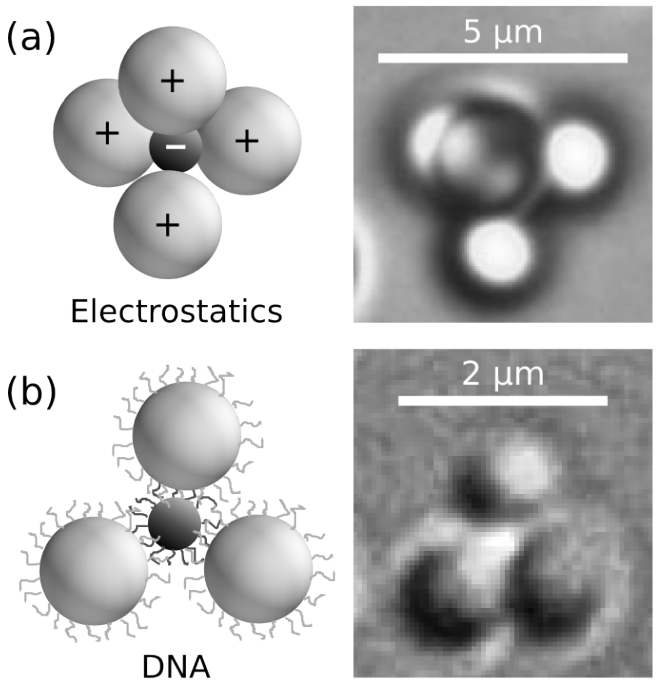

Figure 3.2: (a) Oppositely charged polystyrene spheres cluster due to electrostatic attraction. Optical micrograph shows a tetramer ($N = 4$). (b) Polystyrene spheres labeled with complementary DNA strands (not to scale) cluster due to DNA hybridization. Optical micrograph shows a trimer ($N = 3$); the small, central sphere is fluorescent.

driven by electrostatic interactions. We mix large, positively-charged particles with small, negatively-charged particles, as shown in Figure 3.2(a). To adjust α we use several different particle sizes (Section 3.4.1). We add salt to reduce the Debye length to approximately 3 nm, small enough to ensure that the interaction range does not significantly influence the effective particle size. In the second system the clustering is driven by hybridization of grafted DNA strands (Section 3.4.2). As shown in Figure 3.2(b), we mix small and large spheres labeled with complementary DNA oligonucleotides [119]. We work well below the DNA melting temperature so that the attractive interaction is many times the thermal energy [120].

3.2.2 Random Parking Theory

To better understand why the distribution is sharply peaked at $N = 4$ for $\alpha = 2.45$, we use simulations and analytical techniques that account for the irreversibility of the aggregation process.

Simulation Results

Our simulations use a "random parking" algorithm [13, 121, 122, 123] to model the formation of clusters. The algorithm involves attaching large spheres to randomly selected positions on the surface of a small sphere, subject to a no-overlap constraint (Section 3.4.4). We do not model the finite range of the interactions, which in both experimental systems is small compared to the particle size, or the diffusion of the particles prior to binding. In accord with experimental observations, the particles are not allowed to rearrange once bound. We repeat the process numerically to obtain distributions of cluster sizes as a function of a single parameter, α.

The simulations find a 100% yield of tetramers at the size ratio $\alpha \approx 2.41$. As in the experiments, the large particles in these tetramers are not densely packed, and the clusters are therefore distorted tetrahedra. We also find that while the yield of any particular cluster can be maximized by varying α [Figure 3.3(a)], the yield approaches 100% only for dimers ($N = 2$) and tetramers ($N = 4$). Interestingly, the yield curve for tetramers has a cusp at its peak, showing that the size ratio α_c at the maximum is a mathematical critical point.

The simulated distributions agree well with those found experimentally [Figs. 3.3(b) and 3.3(c)] for both electrostatic and DNA-mediated interactions. For instance, at

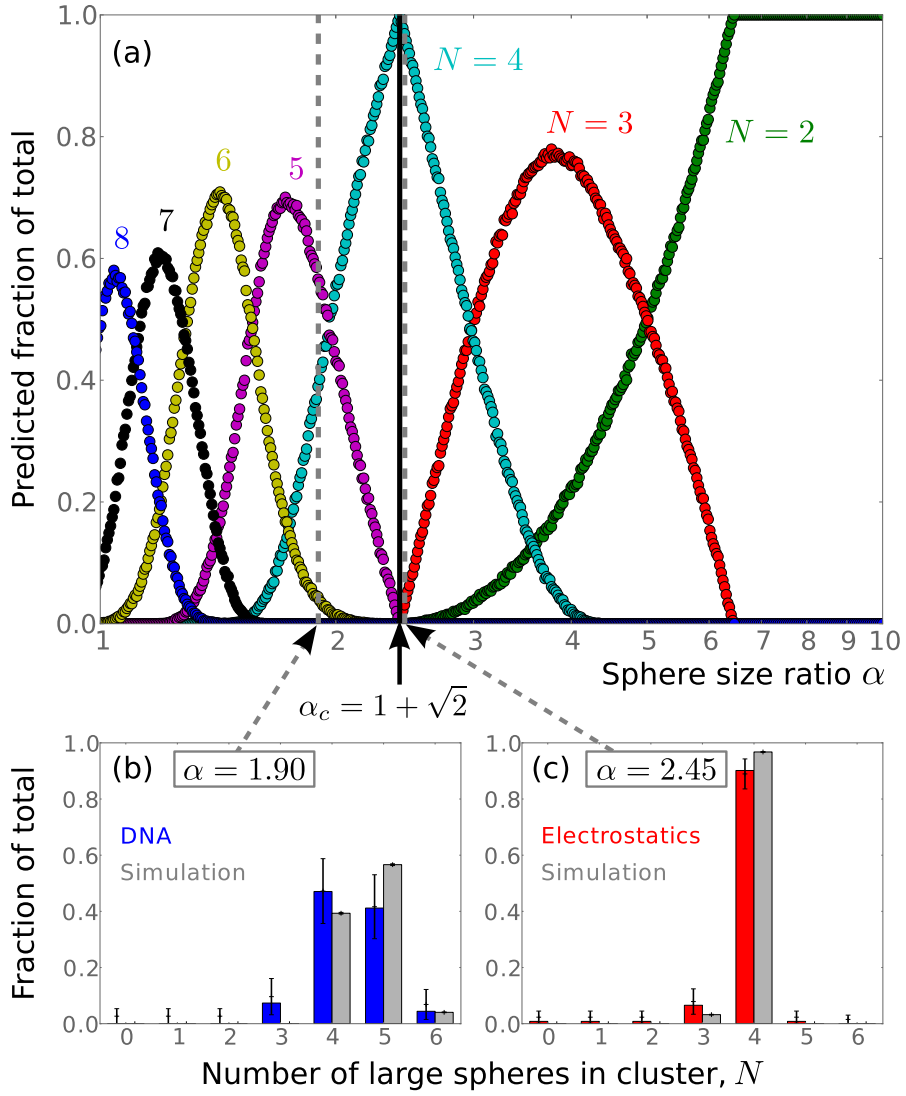

Figure 3.3: (a) Yield curves, as determined by simulations, for N-particle clusters, $2 \leq N \leq 8$, where the critical size ratio α_c is marked with a black line. Below are histograms for (b) DNA-labeled particles (left) at $\alpha = 1.90$ and (c) charged particles (right) at $\alpha = 2.45$, as observed in experiments (colored bars) and as predicted from simulations (gray bars). Error bars are 95% confidence intervals (Wilson score interval method).

$\alpha = 2.45$ with electrostatic interactions, we find a sharply peaked distribution consisting almost entirely of tetramers. This value of α is close to but not precisely at the critical value, so a small yield of trimers is predicted and observed experimentally. In contrast, at $\alpha = 1.90$ we find a mixture of mostly $N = 4$ and $N = 5$ clusters in both the DNA system and simulations. Some discrepancy arises between the simulated and experimental histograms because the yield curves in Figure 3.3(a) are steep; a slight error in the effective size ratio can shift the cluster distribution. Nevertheless, the random sphere parking model successfully reproduces both the large yield of tetrahedra near α_c and the details of the measured histograms at various other α.

Origin of Geometrical Critical Point

That we can reproduce the same phenomenon in two different experimental systems and in a one-parameter model suggests that the critical size ratio α_c has a universal, geometrical origin. Intuitively, one might expect that it is related to packing constraints on the large spheres. Other theoretical studies of random sphere parking [121, 13] have calculated the maximum number of large spheres $N_{\max}$ that can fit around a small sphere at a given α. However, this bound cannot by itself explain why the yield of tetramers can reach 100% while that of other clusters, such as trimers or hexamers, cannot. At a given α, it tells us only why no clusters larger than $N_{\max}(\alpha)$ can form, but it says nothing about the probability of forming smaller clusters with different arrangements.

Therefore we also examine a different bound, one not previously discussed in the context of random sphere parking: the "minimum parking" curve $N_{\min}(\alpha)$. $N_{\min}$ is

the smallest number of hard spheres that can be positioned on a smaller sphere such that another sphere cannot fit. To understand this bound, consider a simple, one-dimensional analogy to car parking on a busy city street, where if a space opens up that is large enough to fit a car, it is filled. The minimum parking number occurs when all drivers have been equally inconsiderate, leaving spaces between their parked cars that are all slightly too small for another car to fit. This lower bound is meaningful only at long times, when all available parking spaces have been filled. The long-time limit holds also for our experiments and simulations, which we carry out until the average cluster size has saturated.

Whereas the upper bound $N_{\max}(\alpha)$ is straightforwardly related to solutions of the well-known spherical packing problem [112, 124], the calculation of the lower bound $N_{\min}(\alpha)$ requires a different approach. In our clusters, the distance between the centers of any two big spheres must be at least $2R_{\text{large}}$. Consider then a sphere of radius $(R_{\text{small}} + R_{\text{large}})$ that circumscribes the centers of the parked spheres. If this sphere is completely covered with N circles of radius $2R_{\text{large}}$, it will be impossible to add an $(N+1)^{\text{th}}$ large sphere. We are led naturally to the *spherical covering* problem, a problem with a rich history in mathematics. Like spherical packings, spherical coverings are solutions to an extremum problem: they are arrangements of N points on a sphere that minimize the largest distance between any location on the sphere surface and the closest point [112]. But unlike spherical packings, spherical coverings need not correspond to arrangements of nonoverlapping spheres. We therefore solve for the minimum parking curve by examining the solutions to the spherical covering problem [124] at each N and manually verifying that they

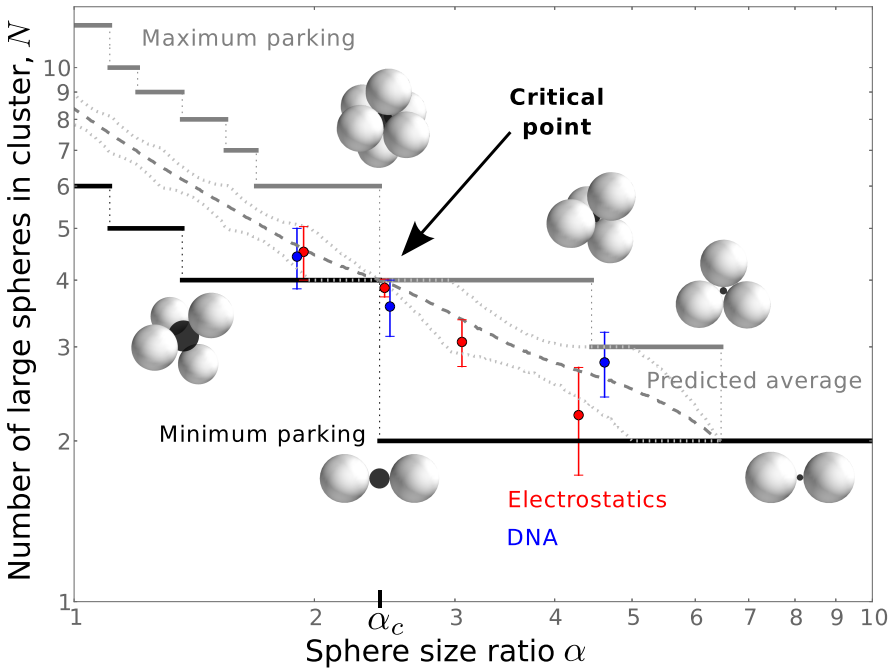

Figure 3.4: $N_{\max}$ (solid gray) and $N_{\min}$ (black) as functions of α. Cluster images show sphere configurations at discontinuities of these curves. Average cluster sizes from simulations (dashed gray line) and experiments (blue and red data points) are shown. We characterize the statistical dispersion in each distribution by the average absolute deviation from the median, indicated by dotted light gray lines for simulations and vertical bars for experiments.

correspond to nonoverlapping configurations.[1]

Our analytical results for the bounds reveal why α_c is a special point: it is the only nontrivial point where the calculated maximum and minimum parking curves come together (Figure 3.4). Analytically we find the location of the critical value to be $\alpha_c = (1+\sqrt{2}) \approx 2.41$, very close to the values where the experimental distributions are peaked. At α slightly larger than this value, the minimum parking configuration corresponds to two spheres placed at opposite poles ($N_{\min} = 2$), and the maximum N

[1]See Appendix A for additional details.

is obtained by first parking three large spheres next to one another, so that there is room for one more sphere to park ($N_{\max} = 4$). At α slightly smaller than α_c , the big spheres can park along orthogonal axes about the small sphere to make an octahedron ($N_{\max} = 6$). The minimum N is obtained by placing four spheres as far from each other as possible, so as to make the addition of a fifth impossible ($N_{\min} = 4$). Thus, as we increase α through α_c, $N_{\max}$ goes from 6 to 4 and $N_{\min}$ from 4 to 2, and the two curves become infinitesimally close.

The parking process is therefore geometrically constrained to yield clusters with exactly $N = 4$ particles in the limit $\alpha \to \alpha_c$. A simple geometric argument sheds some light on this result. At α_c there is always room for four large spheres to park. Parking more spheres requires that at least three park precisely along a great circle of the smaller particle, but the probability of this happening randomly is zero. Thus irreversible binary aggregation, a stochastic process, has a deterministic feature at the critical size ratio: although the space between the large spheres can vary, all clusters must be tetramers. Our numerical approach confirms that the statistical dispersion in the cluster size distribution vanishes at α_c, as shown in Figure 3.4.

The experimental and simulated distributions differ slightly due to two effects. First, the measured sizes tend to be smaller than the simulated ones because a few parking spaces remain unfilled even at long times. This effect is more pronounced for larger spheres, which diffuse more slowly and encounter the small spheres less frequently. The systems most affected are the electrostatic ones at $\alpha = 3.06$ and 4.29. Second, the experimental size ratios can vary by 5% due to polydispersity. Both of these factors increase the width in the experimental distributions and diminish the

achievable yield of tetramers near α_c. The random parking model also assumes the interactions are infinitesimally short-ranged and isotropic. It would not be valid if, for example, there were surface inhomogeneities on length scales comparable to the particle radii. Nevertheless, the experimental data indicate that near α_c a tetramer yield of at least 90% is possible, and the model is useful for predicting cluster size distributions in two very different colloidal systems.

3.3 Conclusion

These results have both fundamental and practical consequences. On the fundamental side, the particle size ratio could affect the jamming threshold in bulk packings of bidisperse spheres. Previous simulations of these systems have shown that the distribution of coordination numbers also depends on the size ratio [125] and may be modeled using random parking [122]. This contrasts with dense atomic systems like metallic glasses [114, 115] in which the atoms have some freedom to rearrange locally. In these systems packing constraints may explain structure and coordination better than parking arguments.

On the practical side, this random aggregation process is a simple way to mass produce tetrahedral clusters in theoretically 100% yield. Although the tetrahedra we produce are irregular in that the distance between the large spheres can vary, it may well be possible to form large quantities of symmetric tetrahedra simply by shrinking the small spheres after the tetramers have formed [126]. An additional step, such as density gradient centrifugation [51], will also be required to separate the assembled clusters from the many unbound large particles. Furthermore, although the yield will

approach 100% only for dimers and tetramers, the yield of any N-particle cluster can be maximized by choosing the appropriate size ratio. For instance, the yield of octahedral clusters, also promising candidates for building metamaterials [37], may surpass 70% at $\alpha = 1.42$.

The size ratio in binary colloidal systems thus emerges as a valuable control parameter for directed self-assembly. Moreover, because it does not require precise control over the interactions, random parking offers a robust and simple way to make colloidal clusters that are more monodisperse than those prepared through other methods [51].

3.4 Materials and Methods

3.4.1 Electrostatic Interactions

Charged colloidal polystyrene spheres were purchased from Invitrogen as "IDC surfactant-free latex" in batches as listed in Table 3.2.

Table 3.2: Charged particles used in electrostatic system experiments. Values for surface charge from data sheets provided by manufacturers.

Mean diameter	Surface functionality	Fluorescent?	Surface charge
0.49 μm	carboxylate-modified latex (CML)	yes	-262 μC/cm^2
0.95 μm	amidine	no	$+23.7$ μC/cm^2
1.2 μm	amidine	no	$+18.2$ μC/cm^2
1.5 μm	aldehyde-amidine	no	$+18.2$ μC/cm^2
2.1 μm	amidine	no	$+30.2$ μC/cm^2

A 100 μL sample of each colloid was diluted to 1% weight by volume. This was then vortexed for a few seconds and bath-sonicated for 10 seconds. We cleaned the particles by centrifuging and redispersing them several times in deionized (DI) water, using the following wash procedure.

1. Colloids were centrifuged for 5 minutes at 6 600g.

2. Supernatant was removed and 190 µL of DI water was added to each sample.

3. Samples were vortexed for 5 seconds each and then bath-sonicated for 10 seconds.

Because the washing procedure involves centrifugation at high acceleration, it can cause the particles to aggregate. The vortexing and sonication steps break apart the majority of these aggregates, but some small aggregates remain and can later appear as clusters showing non-specific aggregation. We do not count these non-specific aggregates when we characterize the cluster size distribution.

We performed six wash cycles. After the last centrifugation, the supernatant was replaced with 40 µL of DI water, rather than 190 µL as before. Then 50 µL of 20 mM NaCl was added to each sample to achieve an overall salt concentration of 10 mM. This screens the repulsion between like particles before mixing.

We prepared mixtures of the positively and negatively charged particles such that each mixture contained one batch of positively charged particles at 1% w/v. In each mixture, the number ratio of the large (positively charged) to small (negatively charged) spheres was 100 : 1. The salt concentration in each mixture was 10 mM NaCl. Each mixture consisted of large and small particles with a different size ratio $\alpha = R_{\text{large}}/R_{\text{small}}$, as listed in Table 3.3.

Each mixture was stored in a micro-centrifuge tube and vortexed at 3 000 rpm, bath-sonicated for 20 seconds, and then mounted on a Glas-Col Rugged Rotator to tumble slowly at 4 °C. Each mixture tumbled for at least three days before observation

Table 3.3: Size ratios and components of binary mixtures of charged colloids.

α	Large particles	Small particles
1.94	0.95 μm amidine (+)	0.49 μm CML (-)
2.45	1.2 μm amidine (+)	0.49 μm CML (-)
3.06	1.5 μm aldehyde-amidine (+)	0.49 μm CML (-)
4.29	2.1 μm amidine (+)	0.49 μm CML (-)

to reduce the effects of sedimentation on local particle concentrations throughout the mixture. To make it easier to identify and characterize one cluster at a time, we diluted samples of the mixtures to 0.1% w/v just prior to observing the distribution of cluster sizes.

Electrostatics Control Experiment

In the experiments outlined above, each mixture contained particles with surface charges of opposite sign. In a separate control experiment, we mixed particles of two different sizes but with surface charges of the same sign. Both components in our control mixture were carboxylate-modified latex (CML) colloids with a size ratio $\alpha = 2.24$, as listed in Table 3.4.

Table 3.4: Colloids used in electrostatic system control experiment.

Mean diameter	Surface functionality	Fluorescent?	Surface charge
0.49 μm	CML	yes	-262 μC/cm^2
1.1 μm	CML	no	-31.5 μC/cm^2

We washed these colloids using the procedure outlined above and then mixed them in a 100 : 1 number ratio. After letting them tumble at 4 °C for several days, we measured the cluster size distribution. As shown in Figure 3.5, fewer than 1% of the small particles bind to large particles when they have surface charges of the same sign. Non-specific aggregation is therefore rare in the charged colloidal systems.

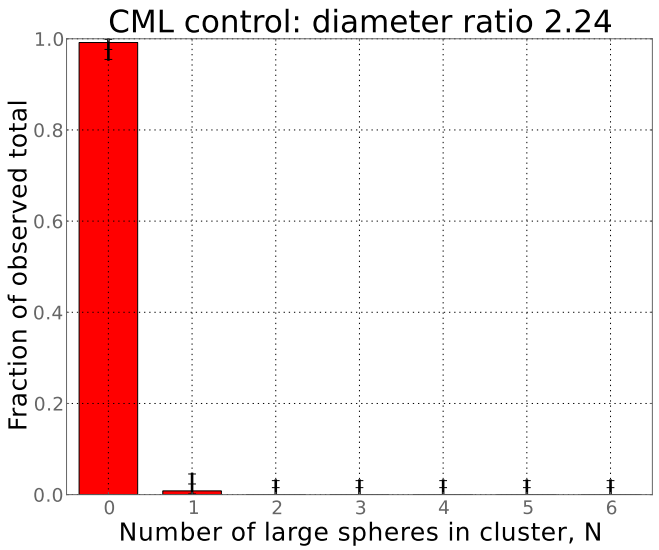

Figure 3.5: Cluster size distribution in a mixture of 1.1 μm non-fluorescent CML particles and 0.49 μm fluorescent CML particles in a 100 : 1 number ratio, showing that particles with surface charge of the same sign rarely form clusters.

Experiments Without Salt

In another set of experiments, mixtures of charged colloidal particles were prepared as described above, but without salt. The number ratio of positively charged spheres to negatively charged spheres was again 100 : 1, and several size ratios α were investigated, as listed in Table 3.5. As in the experiments with 10 mM NaCl, we tumbled the mixtures for several days before measuring the distribution of clusters.

Table 3.5: Size ratios and components of binary mixtures without salt.

α	Large particles	Small particles
1.09	1.2 μm amidine (+)	1.1 μm CML (-)
1.36	1.5 μm aldehyde-amidine (+)	1.1 μm CML (-)
1.94	0.95 μm amidine (+)	0.49 μm CML (-)
2.45	1.2 μm amidine (+)	0.49 μm CML (-)
3.06	1.5 μm aldehyde-amidine (+)	0.49 μm CML (-)
4.29	2.1 μm amidine (+)	0.49 μm CML (-)

Figure 3.6 shows that the average cluster sizes in these mixtures were smaller than the average sizes predicted from simulation and those observed in mixtures containing 10 mM NaCl. For instance, at $\alpha = 2.45$ with 10 mM NaCl the average cluster size is $N = 3.9$, but when there is no salt in the system the average cluster size is $N = 2.7$. For the four size ratios for which there is data both without salt and with 10 mM NaCl, we found that clusters are 20% to 35% smaller when no salt is added.

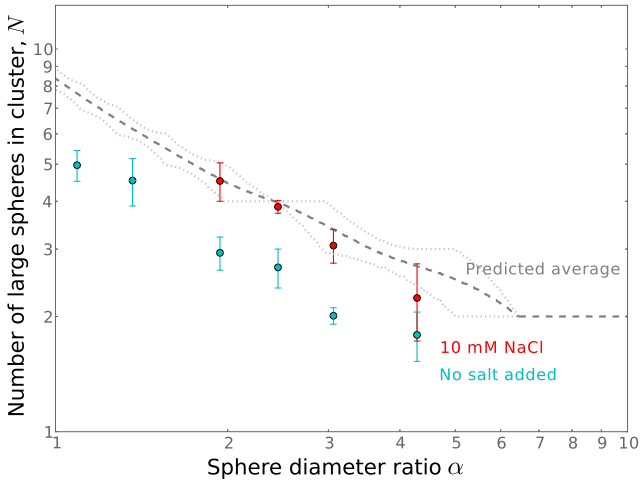

Figure 3.6: Average cluster sizes from simulations (dashed dark gray) and electrostatic experiments with (red data points) and without (cyan) salt. Widths of the cluster size distributions are indicated by dotted light gray lines for simulations and vertical error bars for experiments.

These experiments show that electrostatic repulsion affects the cluster assembly. This observation is consistent with other recent experiments [127] showing that the cluster size distribution in binary mixtures depends on ionic strength when the salt concentration is less than 10 mM. In our mixtures with 10 mM NaCl, the Debye length is approximately 3 nm, very small compared to the particle sizes, so the large spheres do not interact with each other except at small distances. The random parking model

should be more appropriate for systems like these where the interaction range is much smaller than the particle size. This is because the random parking model assumes no interactions between the particles except for a hard-core repulsion and irreversible binding on contact between spheres of two different types.

3.4.2 DNA-Colloid Interactions

In another set of experiments, we mixed small and large spheres labeled with complementary 65-base ssDNA oligonucleotides purchased from Integrated DNA Technologies:

- Sequence A: 5'-biotin-51xT-TGTTGTTAGGTTTA-3'
- Sequence B: 5'-biotin-51xT-TAAACCTAACAACA-3'

The oligonucleotides terminate with a biotin group, which allows us to graft them to streptavidin-coated polystyrene particles using a protocol from Dreyfus *et al.* [119]. We purchased the streptavidin-coated polystyrene particles from Bangs Laboratories, Inc. with the following diameters:

- 0.21 μm, fluorescent, to be coated with sequence B
- 0.39 μm, fluorescent, to be coated with sequence B
- 0.51 μm, fluorescent, to be coated with sequence B
- 0.97 μm, non-fluorescent, to be coated with sequence A

We dissolved the DNA strands in water in 20 μM concentration. We mixed 20 μL of this DNA solution with 10 μL of 1 wt % streptavidin-coated polystyrene particles

with 120 μL of phosphate buffer in a 1.7 mL propylene micro-centrifuge tube. Each 50 mL batch of buffer contained 0.0128 g KH_2PO_4, 0.0707 g K_2HPO_4, 0.1467 g NaCl, and 0.250 g F108 surfactant in 50 mL of deionized water. We filtered the buffer through a 0.2 μm membrane before use. We prepared a separate batch containing no salt so that the salt concentration could be adjusted by combining the two. We vortexed the mixtures at 3 000 rpm for 5 seconds and bath-sonicated them for 10 seconds. We incubated them at room temperature for 30 minutes to allow the ssDNA to graft to the surface of the particles. Then we washed the colloids using the following procedure:

1. We centrifuged the colloids for 3 minutes at 12 000g.
2. We removed the supernatant and added 100 μL of 50 mM NaCl buffer to each sample.
3. We vortexed the samples for 5 seconds at 3 000 rpm and then bath-sonicated them for 10 seconds.

As in the charged particle system, the centrifugation step can create aggregates, some of which survive the vortexing and sonication steps and appear as non-specifically aggregated clusters. We washed each colloid three times to remove excess DNA from the system, and then incubated each at 55 °C for 30 minutes. We then washed three more times, incubated at 55 °C for another 30 minutes, and washed three times again. At this point the salt concentration in the buffer was adjusted to 20 mM. The A- and B-labeled particles were mixed in a 100 : 1 (large : small) number ratio such that the larger particles were at a volume fraction of about 0.1%. Three separate mixtures were prepared, as listed in Table 3.6.

Table 3.6: Size ratios and components of mixtures with DNA-driven interactions.

α	Large particles	Small particles
1.90	0.97 μm, sequence A	0.51 μm, sequence B
2.49	0.97 μm, sequence A	0.39 μm, sequence B
4.62	0.97 μm, sequence A	0.21 μm, sequence B

After the mixtures had been prepared, we followed the same procedure that we used for the charged colloid system.

DNA-Colloid Control Experiment

In the experiments outlined above, each mixture contained particles labeled with complementary DNA strands. In a separate control experiment, we mixed particles of two different sizes but labeled with identical ssDNA.

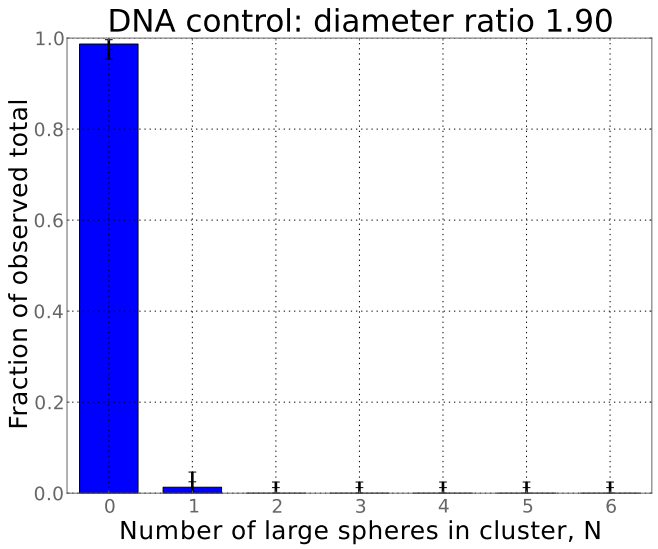

Figure 3.7: Cluster size distribution in a mixture of 0.97 μm non-fluorescent particles and 0.51 μm fluorescent particles in a 100 : 1 number ratio, coated with the same non-self-complementary DNA sequence (A).

Both components in our control mixture were streptavidin-coated polystyrene colloids labeled with sequence A. We used 0.97 μm (non-fluorescent) and 0.51 μm (fluorescent) particles, for a size ratio $\alpha = 1.90$. We functionalized the particles with DNA using the same procedure described above and then mixed them in a 100 : 1 number ratio. After tumbling them at 4 °C for several days, we measured the cluster size distribution. Figure 3.7 shows that fewer than 2% of the small spheres bind to large spheres when they are coated with the same DNA sequence. The low amount of non-specific aggregation is expected, since we designed sequence A to have a negligible amount of self-hybridization even at 0 °C.

3.4.3 Measurement of Cluster Size Distribution

To measure the distribution of cluster sizes in a particular mixture, we placed a 5 μL, 0.1% w/v sample between two cover slips and then sealed it at the edges with UV-curable epoxy (Norland Optical Adhesive 61). We observed each sample under differential interference contrast with a 100X oil-immersion objective on a Nikon Eclipse TE2000-E inverted microscope. We used fluorescence to identify the small spheres.

We obtained the distribution by counting the number of clusters at each N. $N = 0$ is a small sphere without any large spheres adsorbed, $N = 1$ a small sphere attached to a single large sphere, etc. We also counted clusters containing multiple small spheres and clusters formed through non-specific aggregation. The number of such clusters is small compared to the total number of clusters counted. Thus, we do not include these in the histograms.

Our counting procedure is designed to avoid errors from double counting. We begin by counting clusters in the field of view (FOV) on the microscope, scanning through z to find clusters that may initially be out of focus. The Brownian motion of each cluster eventually brings all particles into view. We can therefore determine the number of large and small spheres in each cluster through direct observation. Once we have recorded all clusters in the FOV, we translate the FOV to another part of the sample located more than one FOV away. We repeat this process to build up the histogram, rastering the FOV over the sample. We count more than 60 clusters at each size ratio and more than 120 clusters at size ratios greater than 2. The entire histogram for a given mixture is recorded in one session on the microscope.

3.4.4 Random Sphere Parking Calculations

Monte Carlo Simulations

We simulate the cluster size distribution for spheres undergoing a random sequential adsorption or "random parking" process. We use an algorithm based on Monte Carlo trials. These consist of two stages:

Coarse stage We repeatedly try to insert a disc of radius $r = R_{\text{large}}/(R_{\text{large}}+R_{\text{small}})$ on the surface of the unit sphere. The center of the disc is randomly and uniformly distributed on the sphere. If the disc overlaps any discs that are already "parked", we reject it; otherwise we add it to the list of parked discs. After a fixed number of consecutive rejections, (typically $N_{\text{coarse}} = 10^4$), we switch to the fine stage.

Fine stage We compute the remaining regions of possible insertion and then try to insert an additional disc. We choose the center of the disc randomly and uniformly from these regions.

To find the regions of possible insertion, we first compute the arcs that form their boundaries: Given a central disc of radius r, neighboring disc centers must lie on or outside a concentric circle of radius $2r$. We erase arcs that lie in the interior of the concentric circles of radius $2r$ about each neighboring disc. If the central circle contains any unerased arcs, these are added to our roster of arcs.

We do this for each parked disc center, and then stitch together the remaining arcs to form the regions to which another disc center could be added. To find the area of each region, we inscribe the region in a circumcircle and use a Monte-Carlo integration method to determine the ratio of the area of the region to the area of its circumcircle.

The algorithm terminates when the list of remaining arcs in the fine stage is empty, at which point the final number of inserted discs is recorded.

Bounds on Cluster Size Distribution

The upper and lower bounds $N_{\max}$ and $N_{\min}$ on the cluster size distribution can be calculated from *spherical codes* [124] corresponding to known solutions to the problems of spherical packings ($N_{\max}$) and spherical coverings ($N_{\min}$). Spherical packings are arrangements of N points on a unit sphere that maximize the smallest distance between any two of them [112, 124]. For a given α we determine $N_{\max}(\alpha)$ by looking up the spherical packing [124] with the largest N for which the minimal distance

between points is at least $2\alpha/(1+\alpha)$. Our calculation of $N_{\min}(\alpha)$ is more involved, as explained in Appendix A.

Chapter 4

FDTD Simulations of Plasmonic Nanoclusters

4.1 Introduction

Fluid metamaterials, also known as metafluids, are composed of subwavelength structures that show isotropic electric and magnetic dipole resonances [41, 37]. Electromagnetic resonators can self-assemble from metal nanoparticles [11] and symmetric three-dimensional structures are required for isotropic resonances. The challenge is to assemble these structures in high yield and with high precision. In Chapter 3, we show that random sphere parking enables the self-assembly of tetramers in up to 100% yield, in principle. One simply requires control over the size ratio of two species of spherical particles that bind to one another randomly and irreversibly. However, the clusters that form this way are distorted tetrahedra; the separation gaps between the particles vary and a fifth particle sits at the center of each cluster [91].

What is the optimal geometry for a tetrahedral plasmonic resonator for use as a metafluid constituent? To answer this question, one must understand how the magnetic dipole resonance of the structure depends on several geometric and material parameters. Light must couple strongly to the magnetic resonance mode in the structure for it to be useful in a metafluid. Tuning the optical properties of a metafluid requires adjusting the resonances, so it is also important to understand which parameters are available for shifting the resonant frequency.

4.2 Methods

We conduct finite-difference time-domain (FDTD) simulations to understand how various parameters of gold nanoclusters affect their magnetic dipole resonances. Using the commercial software program Lumerical, we model clusters consisting of gold nanoshells with silica cores, similar to those assembled by Fan *et al.* [11]. The optical properties of gold in the simulations are based on the measurements by Johnson and Christy [4]. In our simulations we suspend each cluster in water ($\varepsilon_r = 1.77$, independent of wavelength) and surround it with perfectly matched (absorbing) layers on all sides. We illuminate each structure with a plane-wave pulse with a wavelength spread from 600 nm to 1200 nm or broader. A circulating current mode produces a strong oscillating magnetic dipole, narrow in frequency, at the center of the structure. The far-field radiation from the magnetic dipole excitation is proportional to the intensity of the magnetic resonance excited at the center. Thus the normalized magnetic field intensity in the frequency domain at the center reveals the frequency of this resonance, if it exists.

We examine how the magnetic dipole resonance depends on structural parameters of the tetrahedral cluster. For instance, we adjust the core/shell diameter ratio x from 0 (solid 150-nm gold spheres) to 0.87 (10-nm-thick gold layer on a 130-nm silica core), holding the separation gaps constant at 20 nm. We also increase the separation gaps to characterize how they affect the magnetic resonance. Additionally, we vary the dielectric function of the particles, insert an additional metal sphere at the center of the cluster, and add roughness to the particles' surfaces to see how each of these parameters affects the magnetic dipole resonance.

4.3 Results and Discussion

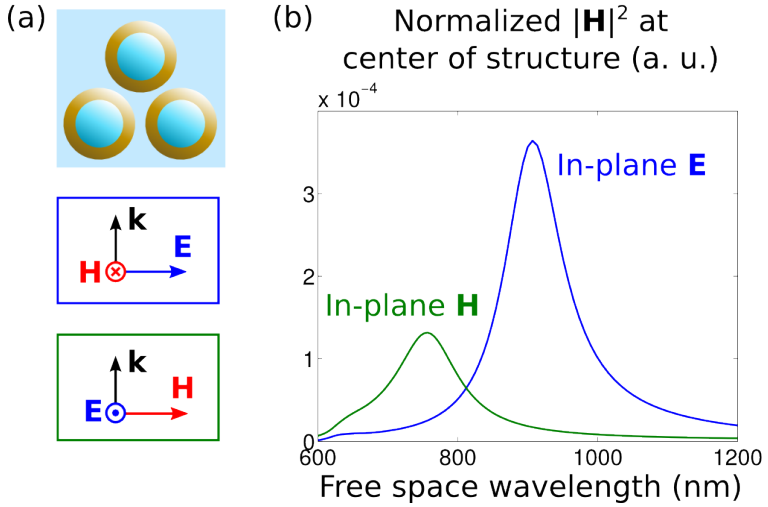

Figure 4.1: FDTD simulation results for a trimer suspended in water. (a) The trimer consists of 150 nm gold spheres with 100 nm silica cores and 10 nm gaps between the gold shells. It is illuminated with a light pulse in one of two polarizations. (b) The plot shows the magnetic field intensity at the center of the structure as a function of frequency for each polarization.

First we consider the trimer, an arrangement of three gold nanoshells and the

simplest analogue of a split-ring resonator that can be constructed from metal spheres [Figure 4.1(a)]. When the magnetic field is perpendicular to the plane of the trimer, and the electric field is in the plane, the pulse strongly couples to the magnetic dipole mode because the electric field is aligned with the gaps between the spheres, and the magnetic flux through the center oscillates. This coupling is evident from the strong resonance near 900 nm in Figure 4.1(b). For a perpendicular polarization, the coupling is weaker and the resonance occurs at higher frequency. These differences between the resonant frequencies and their amplitudes illustrate the anisotropy of the trimer and support other theoretical and experimental studies [128, 11].

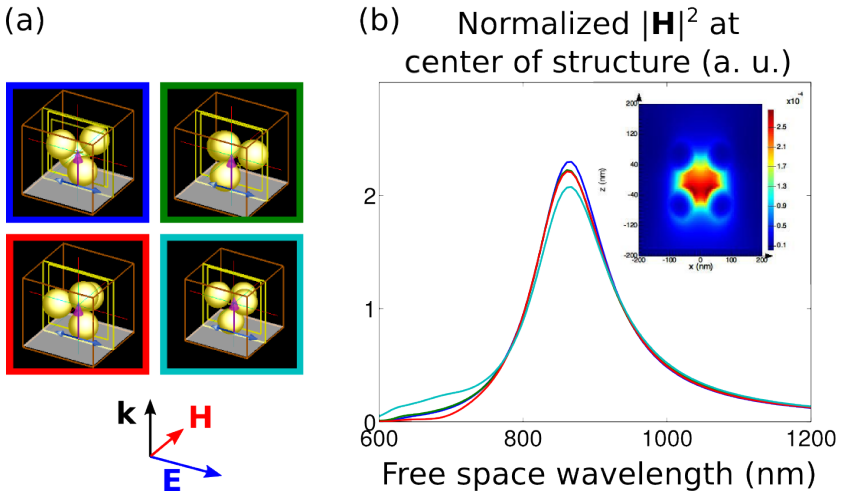

Figure 4.2: FDTD simulation results for a tetrahedron suspended in water. The tetrahedron consists of 150 nm gold spheres with 100 nm silica cores and 20 nm gaps between the gold shells. (a) We simulate the tetrahedron's response in four different orientations for a given polarization. (b) Magnetic field intensity at the center of the structure. The colors of the curves correspond to the colored outlines of the orientations shown at left. Inset shows a colormap of magnetic field enhancement in the **E**-**k** plane of the structure at resonance ($\lambda = 860$ nm) when oriented as shown in the picture at left with the dark blue outline.

We next examine a tetrahedron composed of gold nanoshells [Figure 4.2(a)] to

test whether it produces an isotropic magnetic response. Isotropy in this sense means that the cluster responds identically for all orientations of the tetrahedron. As shown in Figure 4.2(b), rotating the tetrahedron does not affect the magnetic dipole excitation. The invariance of the resonance with respect to orientation supports previous predictions [41] and observations [58]. The small discrepancies between the curves are likely due to numerical factors, such as how the simulation mesh is defined for each orientation of the cluster.

Since we use solid gold nanoparticles in our experiments while previous studies have used gold nanoshells [11, 129, 57], we examine the dependence of the magnetic resonance on the core/shell diameter ratio x. We vary x from 0 (solid 150 nm gold spheres) to 0.87 (10 nm thick gold layer on a 130 nm silica core), as shown in Figure 4.3(a), holding the interparticle separation gaps constant at 20 nm. The resonance redshifts with increasing x, consistent with enhanced capacitive coupling within the nanoshells due to the larger interior cavity. We see that for $x < 0.67$, when the gold layer is thicker than the gold skin depth, increasing the gold thickness negligibly affects the resonance, consistent with results reported elsewhere [41]. The capacitive coupling increases with decreasing separation gaps between the spheres, as shown in Figure 4.3(b). As the gaps become smaller, the resonance intensifies and redshifts, consistent with expectations from the LC circuit analogy.

Previous studies have indicated that high index contrast alone can produce magnetic behavior in nanostructures, as observed in silicon carbide [130, 131]. We investigated the magnetic resonance for a tetramer composed of solid particles made out of an idealized high-index dielectric, similar to diamond in permittivity but non-

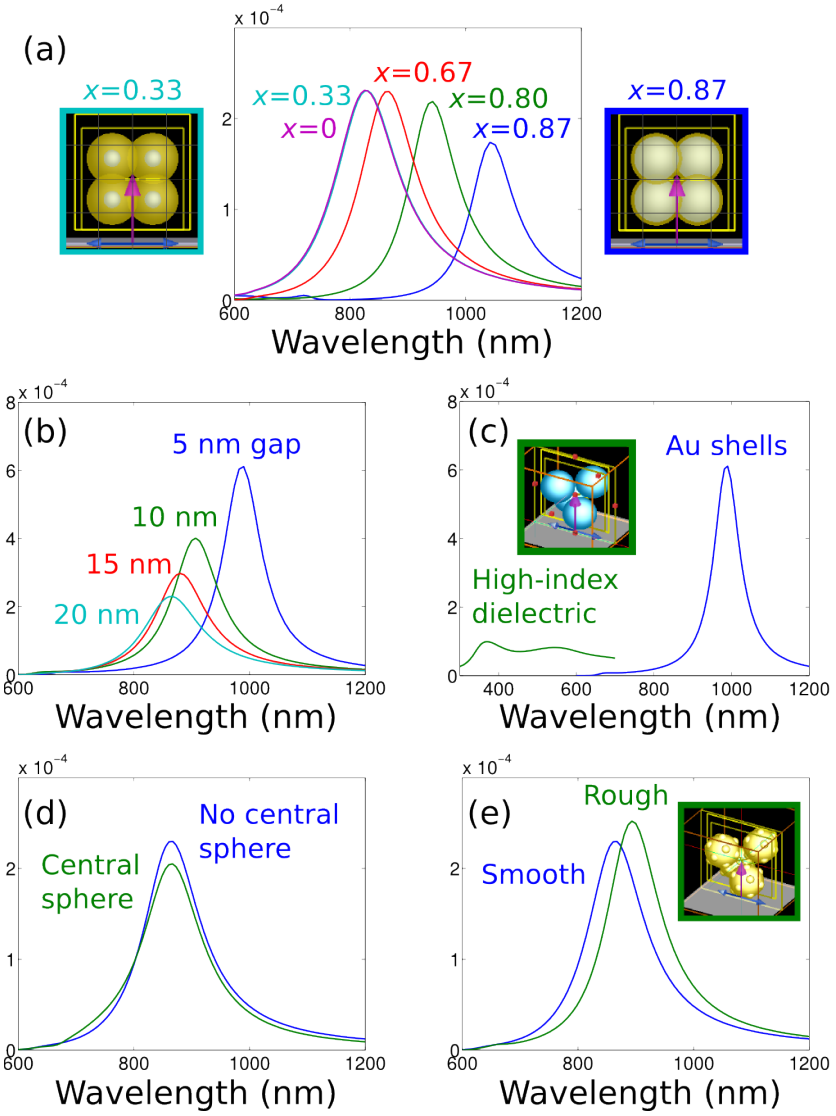

Figure 4.3: Magnetic field intensity in the frequency domain at the centers of simulated tetramer structures. (a) The resonance redshifts with increasing core/shell diameter ratio x. Solid gold spheres correspond to $x = 0$ while $x = 0.87$ represents large silica cores with thin gold shells. (b) The resonance redshifts and strengthens when the separation gap between gold nanoshells decreases from 20 nm to 5 nm. (c) We compare magnetic resonances of tetrahedra of gold nanoshells to those of tetrahedra of spheres made out of an idealized dielectric with high index contrast. The separation gaps are 5 nm for both structures. (d) The addition of a smaller gold sphere at the center of the gold nanoparticle tetrahedron has a minor impact on the magnetic dipole resonance. (e) Surface roughness can shift the magnetic dipole resonance, but the shift is likely due to a decrease in the effective interparticle gap.

dispersive. As depicted in Figure 4.3(c), the magnetic resonance can be observed, but with much weaker coupling and at a higher resonant frequency than that predicted for a tetramer of gold particles. Thus, a dielectric tetramer is less attractive as a metafluid building block than a metal tetramer.

We also use FDTD simulations to examine some practical considerations regarding the assembly of the tetramer. When we place a small gold sphere at the center of the tetramer in our simulations, the magnetic dipole resonance does not shift in frequency, as shown in Figure 4.3(d). Moreover, the strength of the resonance is only slightly diminished by the presence of the central gold sphere. Therefore, a self-assembly approach in which metal particles assemble into a tetrahedron on the surface of another metal particle does not compromise the resulting magnetic dipole resonance. The presence of a small metal particle at the center of the structure might affect the electric dipole resonance, but we have not examined that effect.

Additionally we study the effect of surface roughness on the resonance by dotting the surfaces of the gold nanoshells in our simulation with gold bumps. We see a small shift in the resonance behavior [Figure 4.3(e)], but this shift can be attributed to a decrease the effective separation gap between the spheres. Thus, although it would be important in practice to keep the spheres as smooth as possible, slight surface roughness may not severely degrade the magnetic resonance of the cluster. This particular simulation is by no means conclusive, as surface roughness is difficult to parametrize [132]. In this simulation, we added gold bumps to all of the spheres in an identical, symmetric pattern. However, as the electron micrographs in 2.14 indicate, surface roughness in general is neither symmetric nor identical from one

particle to another. The faceting shown in the commercial gold particles could likely be detrimental for coupling because of the high fields near the sharp edges of the particles.

4.4 Conclusion

Our FDTD simulations support the findings reported elsewhere [41, 58] that a tetrahedral structure consisting of four gold nanoparticles exhibits isotropy in its magnetic dipole response, a long-sought property for metamaterial applications. The resonance is sensitive to geometric parameters such as the separation gaps between particles and the core/shell diameter ratio, so a high degree of precision would need to be attained over these parameters before a bulk suspension of tetramers could be used as a practical metafluid. As the core/shell diameter ratio x increases, the resonance weakens, redshifts, and becomes more sensitive to x. Solid metal spheres, rather than nanoshells, would serve as ideal building blocks for these resonators because they correspond to $x = 0$. As shown in Chapter 2, it is possible to make smooth gold nanospheres experimentally.

Additionally, our simulations indicate that the presence of a metal nanoparticle at the center of a tetramer is not necessarily problematic for its optical properties. Such structures could be assembled from metal nanoparticles by using a random parking approach [91]. Because random parking results in 100% yield of tetramers when the diameter ratio of the spheres is $\alpha_c = 1 + \sqrt{2}$, all that is required for the high-yield assembly of ideal magnetic resonators is a means of applying this technique with smooth gold nanospheres.

Chapter 5

Self-Assembly of Tetrahedral Plasmonic Nanoclusters

5.1 Introduction

When a subwavelength conducting structure interacts with light, its geometric and material properties can result in exotic optical phenomena. Such structures can act as magnetic resonators [6, 7, 9], optical nanocircuits [76], plasmonic antenna arrays [18], and photonic traps for individual proteins [133]. Flat metal nanostructures can be fabricated for these applications with techniques like electron-beam lithography and focused ion beam milling [3]. However, some optical phenomena, like isotropic magnetic resonances, a key to producing metafluids [41, 37], require three-dimensional subwavelength structures. One way to produce the structures is colloidal self-assembly, wherein the interactions between nanoparticles suspended in a fluid direct their spontaneous organization into three-dimensional structures. Colloidal

self-assembly has been used to create plasmonic nanoclusters that exhibit optical magnetism [11] and Fano interference [12, 66], but isotropic resonance requires high-symmetry clusters such as tetrahedra [41]. Although there are some methods to self-assemble these structures – for example, polymer encapsulation [58] or attachment to dielectric cores [60, 61] – there is as yet no method that can produce structures with reproducible, isotropic optical properties in high yield.

Here we show that tetrahedral plasmonic clusters can self-assemble in high yield from metal nanoparticles that irreversibly bind to one another. We mix gold nanoparticles with smaller particles such that there is a specific attractive interaction between the two sizes (Figure 3.1). The large particles bind to the small particles irreversibly and randomly. In a previous report [91], we showed that this process, which is described in the mathematics literature as "random parking" [121, 13], results in a high yield of irregular tetrahedra if α, the ratio of the large to small sphere diameter, has the critical value $\alpha_c = 1 + \sqrt{2}$. We extend this work using spherical gold nanocrystals that are prepared through a combination of synthesis and chemical etching such that they are monodisperse and smooth down to the nanometer scale. Unlike the nanoparticles used in previous metafluid studies, spherical nanoparticles of this quality may result in clusters with precise, reproducible plasmonic properties [132].

5.2 Self-Assembly Experiments

As in Chapter 3, we pursue two different strategies for directed self-assembly of clusters. In each of our experiments, either DNA hybridization or electrostatic forces give rise to strong, short-ranged, attractive interactions that drive cluster self-

assembly. One difference in this study is that we use particles on the 0.1 μm scale, rather than on the 1 μm scale. The size of the DNA strands is closer to the particle size at this smaller length scale. Another difference is that, rather than polystyrene, in this study we use gold particles, which have higher density and different surface chemistry. We must use different methods to attach DNA strands to these particles.

5.2.1 DNA-Mediated Interactions

To prepare a colloidal mixture in which DNA strands mediate interactions, we first design ssDNA sequences so that they can create a strong bond between two nanoparticles. The DNA sequences are:

- Sequence X: 5'-thiol-50xT-CCACATCAACCTACT-3'
- Sequence Y: 5'-thiol-50xT-AAGAGTAGGTTGATG-3'

The last 12-base portions of the sequences, closest to the 3' ends, are complementary to one another. We check computationally that the sequences are not self-complementary [134, 135], because self-complementarity could result in aggregation of each species before mixing. We purchase the oligonucleotides from Integrated DNA Technologies, Inc. (IDT). From British Biocell International (BBI), we purchase gold particles that are made with a proprietary technique based on citrate reduction of $HAuCl_4$ in water [47, 48].

Functionalization of Gold Nanoparticles with Thiolated DNA

Our procedure for grafting DNA strands to citrate-stabilized gold particles is similar to other protocols in the literature [32, 136], with a few differences. First, we

use borate buffer (diluted from 20X stock, Thermo Scientific) rather than phosphate buffer. Second, we add salt to the particles slowly over a period of days. This ensures that even particles as large as 100 nm remain stable during the salting process. A summary of our procedure follows and more details can be found in Appendix B.

We begin by adding 200 µL of 0.1 M dithiothreitol (Research Products International Corp.) in deionized water to 100 nmol of each oligonucleotide as received from IDT, and then we wait for one hour. Dithiothreitol cleaves disulfide bonds between thiolated DNA strands so that the thiol groups can bind to the surface of gold. Then we purify the deprotected DNA solutions by elution through NAP-5 columns (Sephadex G-25 DNA grade, GE Healthcare Life Sciences). This step removes the dethiothreitol. From this point on, we keep our DNA solutions frozen or on ice to minimize the formation of new disulfide bonds between strands.

At this point we add the DNA to the particles and begin the salting process. First, we measure the concentrations of DNA and gold particles using UV-vis spectrophotometry (NanoDrop 1000). We add DNA solution to a 2 mL aliquot of gold particle suspension. For 50 nm gold, we add about 18 000 times as many DNA strands as particles, so that the DNA concentration is 1 µM. For 100 nm gold, the ratio is 100 000 and the DNA concentration is 25 nM. Next we adjust the buffer to 50 mM borate and 0.01 wt % sodium dodecyl sulfate (SDS) and let the mixture incubate for at least one hour at room temperature. Over the next three days, we gradually add NaCl to the solution to increase its salt concentration in 25 mM increments, until it reaches a final concentration of 250 mM NaCl. During each salting step, we also increase the DNA concentration in 100 nM increments to maximize the DNA loading

on the particles [32].

We incubate the particles at room temperature for three days and then wash them. We pellet them in a centrifuge for 20 minutes (700g for 50 nm particles, 300g for 100 nm particles) and then replace the supernatant with an aqueous buffer containing 50 mM borate buffer and 100 mM NaCl. We repeat this procedure for a total of three wash cycles. At the end of the last wash we add supernatant to resuspend each sample to just 10% of its original volume, so that each suspension is at a high concentration. Thereafter we store the DNA-functionalized particles at 4 °C.

Bidisperse Mixtures

We dilute the DNA-labeled 50 nm gold particles with buffer containing 50 mM borate and 100 mM NaCl, and then prepare mixtures of 100 nm particles and 50 nm particles in different approximate stoichiometric ratios (1:1, 10:1, 100:1, and 1000:1). We tumble the mixtures for four days on a Glas-Col Rugged Rotator. In the 1:1 mixture, the color of the solution gradually changes from orange to pale purple, indicating aggregation. The other mixtures do not show a color change. This lets us determine by eye which mixtures have a sufficiently high stoichiometric ratio of large particles to small particles such that small clusters are statistically favored over large aggregates [91]. We select the 10:1 mixture for further investigation.

5.2.2 Electrostatic Interactions

In a separate set of experiments, we mix gold particles with smaller particles whose surface charge is opposite in sign. The choice of material for the smaller

particle species is quite flexible, and we investigate several different types of particle.

Positively Charged Gold Nanospheres

For the large particles in the electrostatic scheme, we use gold nanospheres that are exceptionally smooth, round, and monodisperse. These particles can be prepared by synthesis of gold octahedral nanocrystals [63], followed by a slow chemical reaction that etches the particles and preferentially removes atoms from their vertices and edges. The reaction proceeds in the presence of polyDADMAC, which stabilizes the particles and gives them a positive surface charge. As shown in Chapter 2, this reaction can be halted after the facets of the crystal have been removed, resulting in spherical nanocrystals. We prepare these particles using the same method described in Chapter 2.

To understand the electrostatic interactions, we characterize the particle surface charge. We measure the zeta potential (ζ) of dilute suspensions of spherical gold crystals using a Malvern ZetaSizer Nano-ZS. As an experimental control, we also measure the zeta potential of dilute suspensions of gold nanoparticles of a similar size purchased from British Biocell International (BBI). The measured zeta potentials are shown in Figure 5.1.

The conventional gold nanoparticles have a negative surface charge ($\langle\zeta\rangle = -45$ mV) but the spherical crystals are positively charged ($\langle\zeta\rangle = 39$ mV), likely owing to the cationic polymer used in the synthesis. Because of this positive surface charge, the method described in Section 5.2.1 for functionalizing gold particles with oligonucleotides does not work for these particles. Instead, negatively charged particles may

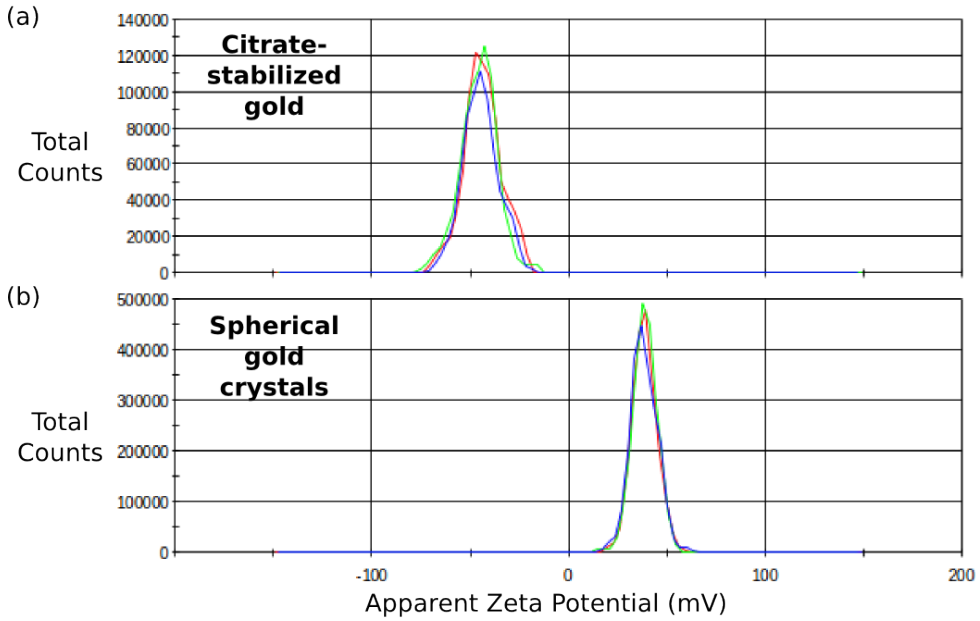

Figure 5.1: Zeta potential distributions of (a) 100 nm gold particles stabilized by citrate and (b) 110 nm spherical crystals prepared from chemical etching of gold octahedra. We plot three independent measurements of each colloid.

be used as the smaller particle species so that self-assembly of large particles on the surface of small particles proceeds due to electrostatic interactions [91].

Negatively Charged Particles

For the small particles, we use either gold nanoparticles functionalized with DNA strands or carboxylate-functionalized polystyrene nanoparticles. The 50 nm gold particles (BBI) are functionalized with DNA using the same method described in Section 5.2.1. We purchase 42 nm polystyrene particles from PolySciences and use them without further chemical modification. Although the polystyrene nanoparticles are fluorescently labeled, this is not a necessary feature for our method. Both of these particle types are strongly negatively charged due to the presence of long, anionic

molecules on their surfaces (DNA in the case of the gold particles and carboxylated polystyrene for the polystyrene particles).

We adjust the buffer of our DNA-functionalized gold particles before mixing them with the spherical gold crystals. We use 50 nm gold particles labeled with DNA sequence Y. We centrifuge the particles at $700g$ for 20 minutes to pellet them, replace the supernatant with either 2 mM NaCl or 10 mM NaCl, and then repeat this process for a total of three wash cycles. We make samples with two different salt concentrations, so that we can combine the colloids to obtain an intermediate concentration.

We wash the polystyrene nanoparticles using a centrifugal filtration device (Vivaspin 500, Sartorius Stedim Biotech). We add 500 μL of 0.2 wt % polystyrene colloid to the device and then centrifuge it at $2900g$ for 10 minutes. The device contains a filter with a 300 000 dalton molecular weight cutoff, which permits the aqueous solution to flow through but stops the nanoparticles. Then we add an additional 500 μL of water and repeat this process for a total of three wash cycles. After the last wash, we resuspend the nanoparticles in 10 mM NaCl to make up 100 μL total volume.

Bidisperse Mixtures

We mix each species of negatively charged nanoparticles with the positively charged gold spheres. We combine them in a variety of number ratios (1:20, 1:2, 5:1, 50:1), as we do in our experiments with DNA-mediated interactions. We mix the suspensions such that the final salt concentration of each mixture is either 10 mM or 1 mM NaCl. We also prepare control samples containing no small particles. Then we tumble the mixtures on a Glas-Col Rugged Rotator at room temperature for more than 12

hours. In the 10 mM NaCl samples, we observe a color change from orange to pale purple, indicating aggregation. The 1 mM NaCl samples with high stoichiometric ratios, however, are stable. As before, we look for the mixture containing the highest number density of small particles that does not exhibit aggregation and select this sample for further study.

5.3 Characterization of Nanoparticle Clusters

To characterize the results of our self-assembly experiments, we use density gradient centrifugation followed by electron microscopy. Each of these techniques yields information about the contents of the mixture.

5.3.1 Density Gradient Centrifugation

Theory

Brownian particles of different sizes or masses can be separated by centrifugation in a density gradient column. The density gradient is prepared in a centrifuge tube and contains high-density fluid at the bottom and low-density at the top. One loads a small colloidal sample at the top of the column. The average density of the sample must be less than that of the fluid at the top of the column to avoid a Rayleigh-Taylor instability, which occurs if a light fluid is supporting a heavier fluid [137]. At high centrifugal acceleration, particles of higher density move toward the bottom of the tube. If the fluid density were uniform over some distance along the tube, the arrival of heavier particles at that point in the tube would create a Rayleigh-Taylor instability

between the fluid at that point and the fluid below. The presence of a continuous gradient in fluid density prevents this instability [53, 51]. In this scheme, the particles are denser than the densest region of fluid, so that the separation depends on the time over which the acceleration is applied. If the time is too long, all particles will pellet at the bottom.

To understand how this technique works, we consider an isolated particle in the frame of its container. The centrifuge tube is not an inertial reference frame because it revolves around the axis of the centrifuge, as illustrated in Figure 5.2(a). Thus, an

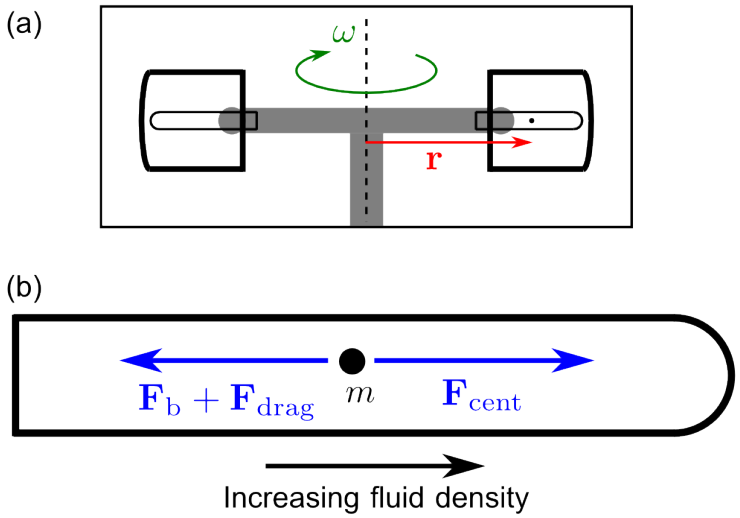

Figure 5.2: (a) Centrifugation of tubes containing density gradient columns and colloidal samples in a hanging-bucket centrifuge. (b) A close-up of a centrifuge tube and the forces that act on a colloidal particle (not to scale).

outward fictitious centrifugal force $\mathbf{F}_{\text{cent}}$ acts on the particle in this frame:

$$\mathbf{F}_{\text{cent}} = m\omega^2\mathbf{r}. \tag{5.1}$$

Here m is the mass of the particle, ω is the angular velocity, and $\mathbf{r}$ is a vector that

points outward from the rotation axis with a magnitude equal to the distance between the particle and the axis. The mass of the particle can be expressed as the product of its density ρ_{p} and volume V_{p}, which in turn can be expressed in terms of the particle's radius R_{p}:

$$\mathbf{F}_{\mathrm{cent}} = \rho_{\mathrm{p}} \left(\frac{4}{3} \pi R_{\mathrm{p}}^3 \right) \omega^2 \mathbf{r}. \tag{5.2}$$

There is correspondingly a fictitious force on the fluid surrounding the particle, which results in an apparent inward buoyancy force $\mathbf{F}_{\mathrm{b}}$ on the particle in accord with Archimedes's Principle [53]:

$$\mathbf{F}_{\mathrm{b}} = -m_{\mathrm{disp}} \omega^2 r = -\rho_{\mathrm{f}} \left(\frac{4}{3} \pi R_{\mathrm{p}}^3 \right) \omega^2 \mathbf{r}, \tag{5.3}$$

where ρ_{f} is the fluid density.

The particle experiences a drag force $\mathbf{F}_{\mathrm{drag}}$ as it moves through the fluid. If the particle is more dense than the fluid (the usual case), the force opposes outward motion of the particle and, by Stokes' Law [138], takes the form

$$\mathbf{F}_{\mathrm{drag}} = -6\pi R_{\mathrm{H}} \eta v \hat{r}, \tag{5.4}$$

where R_{H} is the hydrodynamic radius of the particle, η the fluid viscosity, and v the speed of the particle through the fluid. For constant angular velocity ω a particle at distance r from the axis reaches a terminal velocity $v_t\,(r)$ on a time scale that is short compared to r/v. Therefore at each r, the forces are balanced [Figure 5.2(b)] such

that

$$6\pi R_{\mathrm{H}}\eta\left(r\right)v_t\left(r\right)=\left(\rho_{\mathrm{p}}-\rho_{\mathrm{f}}\left(r\right)\right)\left(\frac{4}{3}\pi R_{\mathrm{p}}^3\right)\omega^2 r, \tag{5.5}$$

where the viscosity $\eta\left(r\right)$ and the fluid density $\rho_{\mathrm{f}}\left(r\right)$ are functions of r.

Rearranging this equation to solve for $v_t\left(r\right)$, we find

$$v_t\left(r\right)=\frac{2}{9}\frac{\left(\rho_{\mathrm{p}}-\rho_{\mathrm{f}}\left(r\right)\right)\omega^2 r}{\eta\left(r\right)}\left(\frac{R_{\mathrm{p}}^3}{R_{\mathrm{H}}}\right). \tag{5.6}$$

Thus, at any particular r in the centrifuge tube, two particles with the same density and different sizes travel at different speeds. This occurs because the ratio $R_{\mathrm{p}}^3/R_{\mathrm{H}}$ generally increases with particle size and all other variables on the right side of equation 5.6 are the same for two particles at the same location and of the same density.

This argument holds for clusters of particles as well, assuming that fluid is not entrained by the cluster. For a tetrahedral cluster of spheres, for example, the hydrodynamic radius of the tetramer is related to the hydrodynamic radius of one of its constituent particles [139, 140] by

$$R_{\mathrm{H,tetra}}\approx 1.844\times R_{\mathrm{H,sphere}}. \tag{5.7}$$

If the tetrahedral cluster contains spheres of mass m, the mass of the cluster is $4m$, which means that the velocity of a tetrahedral cluster of spheres will be higher than

that of a single unbound sphere at any location in the centrifuge tube:

$$v_{t,\text{tetra}} \approx \frac{4}{1.844} \times v_{t,\text{sphere}}$$

$$v_{t,\text{tetra}} \approx 2.17 \times v_{t,\text{sphere}}.$$

We have assumed that entrainment of fluid by the cluster is negligible. This analysis suggests that in general larger clusters travel faster than smaller clusters, as long as they are more dense than the surrounding fluid.

Experiments

We prepare sucrose density gradients using the freeze-thaw method [141]. We make three solutions, starting from solutions of 50 wt % sucrose in water, 50 mM borate, and 100 mM NaCl that are filtered through a 0.2 μm membrane (bottle-top vacuum filter, Corning).

1. 25 wt % sucrose in water
2. 25 wt % sucrose, 50 mM borate, 100 mM NaCl in water
3. 25 wt % sucrose, 1 mM NaCl in water

To make the gradients, we first load 4.25 mL of these solutions into several Ultra-Clear Thinwall Tubes (11 × 60 mm, Beckman Coulter), seal them with at least two layers of parafilm, and sonicate them for 5 minutes. We place the tubes in a -80 °C freezer for at least half an hour, and then move them to room temperature to thaw for 1.5 hours. After the solutions melt completely, we return them to the freezer for

another cycle. We leave the tubes in the freezer for storage after the third freezing step, and we remove them to thaw only when we are ready to use them.

In a typical density-gradient centrifugation run, we first choose a gradient from one of the gradients listed above, so that the borate and salt concentrations match those of the nanoparticle suspension. Once it has melted, we load 10 μL of the nanoparticle suspension onto the top of the fluid column. To do this, we pipette the suspension into the column so that the pipette tip touches the inner wall of the tube just below the meniscus. We hold the pipette at a large angle from the vertical and deposit the sample at a rate of about 1 μL/s. Then we centrifuge the samples in a hanging-bucket centrifuge (Allegra X-15R, Beckman Coulter). We centrifuge the density gradients at $500g$ or $1000g$ for time intervals ranging from 5 to 30 minutes, depending on the particle sizes, and we adjust the angular velocity at the lowest possible angular acceleration and deceleration (with braking).

After centrifuging, we look for evidence of particles or clusters separated into different bands. We do this by examining each tube by eye under dark field with a flashlight positioned under the tube, as shown in the photograph in Figure 5.3(a). If the separation is incomplete, we centrifuge for a longer time. If not, we take a photograph and then use the image processing program ImageJ to measure vertical intensity profiles along the tubes. We extract bands from the tubes using a syringe with a blunt pipetting needle [Figure 5.3(b) and Figure 5.3(c)]. To capture each band, we remove approximately 250 μL of fluid. We centrifuge these fractions at $250g$ for 20 minutes and remove the supernatant to concentrate the contents of each band. We redisperse each fraction by gentle pipetting.

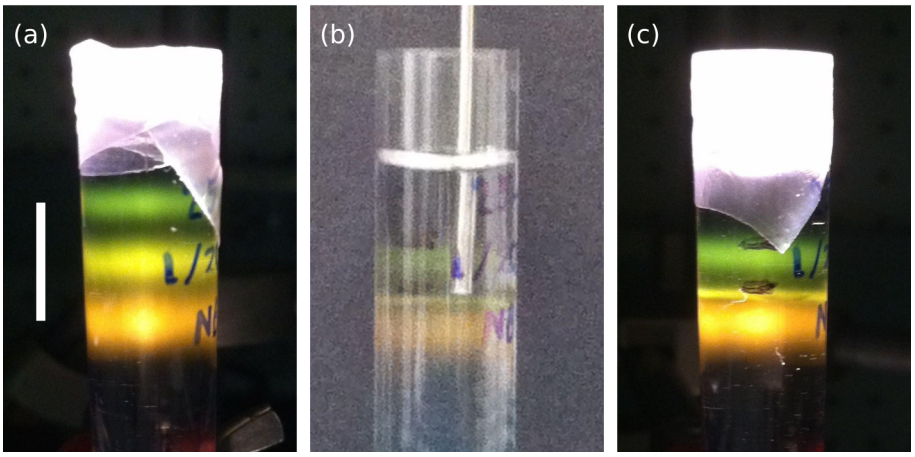

Figure 5.3: (a) Density gradient centrifugation for 15 minutes at 500g of a mixture of gold particles of sizes 60 nm, 80 nm, and 100 nm. The differences in color occur because the particles have different electric dipole resonances, which redshift with increasing particle size. Parafilm is visible at the top of the tube. (b) We insert a blunt pipetting needle to extract the band of 80 nm particles. (c) Dark field illumination shows that a portion of the 80 nm particle band has been removed. Scale bar is 1 cm.

5.3.2 Electron Microscopy

Our scanning electron microscopy (SEM) sample preparation technique is designed to produce a dry sample of clusters on a flat substrate while preventing the formation of a ring deposit or "coffee ring." Typically when a colloidal droplet dries, evaporation occurs most rapidly near the edge, and pinning of the contact line to the solid substrate results in capillary flow outward from the center of the droplet towards the edge [142]. The result is that most of the solid particles in the droplet dry in aggregates near the edge, which precludes determination of the sizes and arrangements of clusters as they existed in suspension.

We avoid this problem by inducing an attraction between the solid colloidal particles and the solid substrate before the droplet dries. We accomplish this by preparing

samples with the following procedure. We sonicate aluminum SEM stubs (Electron Microscopy Sciences) and 5 mm × 5 mm silicon wafer chips (Ted Pella product no. 16008) in isopropanol, then methanol, and then acetone (all HPLC-grade) to clean them. We let them air dry in a fume hood and then immerse the wafers in a solution of 1 wt % poly(diallyl dimethyl ammonium chloride), also known as polyDADMAC (Polysciences), for at least 30 minutes. PolyDADMAC is a cationic polyelectrolyte and it gives the wafer a positive surface charge [143, 144]. Then, holding each wafer piece with tweezers, we rinse each with deionized water and dry it with compressed nitrogen. We place a droplet of colloid on the silicon wafer and wait 10 minutes for the particles to sediment and adsorb to the substrate. Then we rinse the droplet off with deionized water and immediately dry the wafer with compressed nitrogen again. Most of the particles are rinsed off with the droplet but some remain bound to the wafer's surface.

We use conducting paint (Electrodag 502, Ted Pella) to affix the wafer to an aluminum stub. Samples containing polystyrene particles are sputter-coated with 2 nm of platinum/palladium to improve the imaging contrast. We examine our samples with a field-emission scanning electron microscope (Zeiss Ultra55 or Supra55VP). In each instrument, we use both an Inlens detector and an Everhardt-Thornley detector to obtain micrographs.

5.4 Results and Discussion

5.4.1 Faceted Particles

We prepare mixtures of two types of nanoparticles that can strongly bind to one another. First, we design thiolated single-stranded oligonucleotides whose melting temperature is greater than 50 °C [134, 135], so that they will form a strong bond at room temperture. We graft these DNA strands to gold nanoparticles of diameter 50 nm or 100 nm using the procedure given in Section 5.2.1. We aim for a high density of strands on the particles' surfaces, so that when two particles with complementary strands come together, the number of DNA duplexes bridging the particles is high, resulting in a strong bond [145]. We mix the two species of particles in different number ratios and we tumble them at room temperature for several days. Each mixture contains 100 mM NaCl so that the Debye length is 1 nm [146], and the particles interact only at small separations.

Density Gradient Centrifugation

As a control experiment to test for non-specific aggregation, we load a sample of DNA-labeled 100 nm gold particles in 100 mM NaCl into a density gradient prepared with 25 wt % sucrose and 100 mM NaCl using the freeze-thaw method [141]. After centrifuging at 500g for 10 minutes, we see a single bright band with a faint band below it, as shown in the photograph and intensity profile in Figure 5.4(a). This suggests that the majority of the particles in this sample are unbound and that non-specific aggregation is rare.

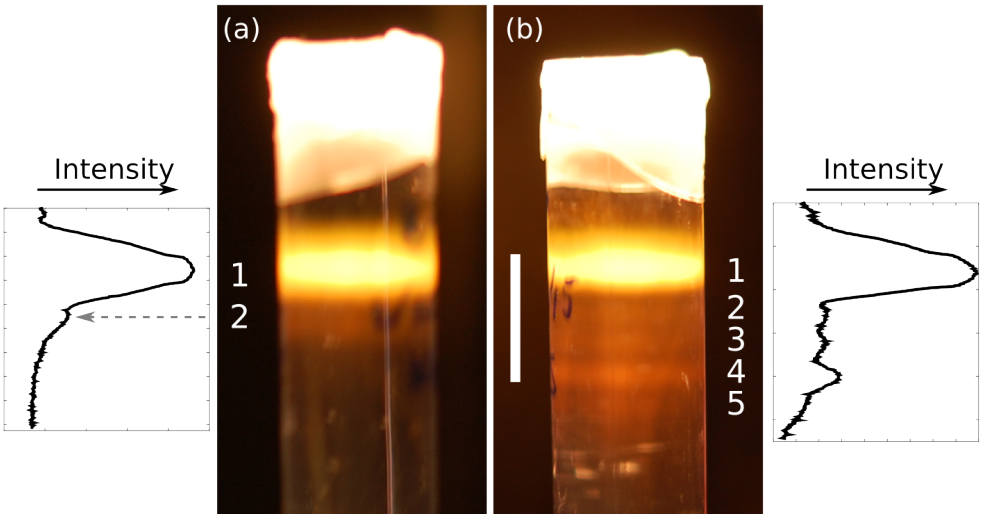

Figure 5.4: Photographs of colloidal gold mixtures after density gradient centrifugation, with vertical intensity profiles shown at the side. (a) 100 nm gold particles labeled with DNA strands move as a broad band through a sucrose density gradient. A faint second band, evident from the intensity profile at left (dashed gray arrow), indicates that non-specific aggregation occurs but is rare. (b) A mixture of 100 nm and 50 nm gold particles labeled with complementary DNA strands separates into bands after density gradient centrifugation. The first and fourth bands are pronounced, corresponding to unbound particles and tetramers. Scale bar is 1 cm.

Density gradient centrifugation of a mixture of 50 and 100 nm gold particles, labeled with complementary DNA strands, reveals the presence of clusters. As shown by Figure 5.4(b), a sequence of faint yellow bands appears below the bright band at the top. The bright band appears at roughly the same height as the bright band in the tube that contains the control mixture, which suggests that it too corresponds to unaggregated 100 nm gold particles. The lower bands do not occur in the control mixture. The fourth band is the brightest, suggesting that tetramers are the most common type of cluster that assembles. We extract each band, starting from the top of the tube, for further investigation by electron microscopy.

Scanning Electron Microscopy

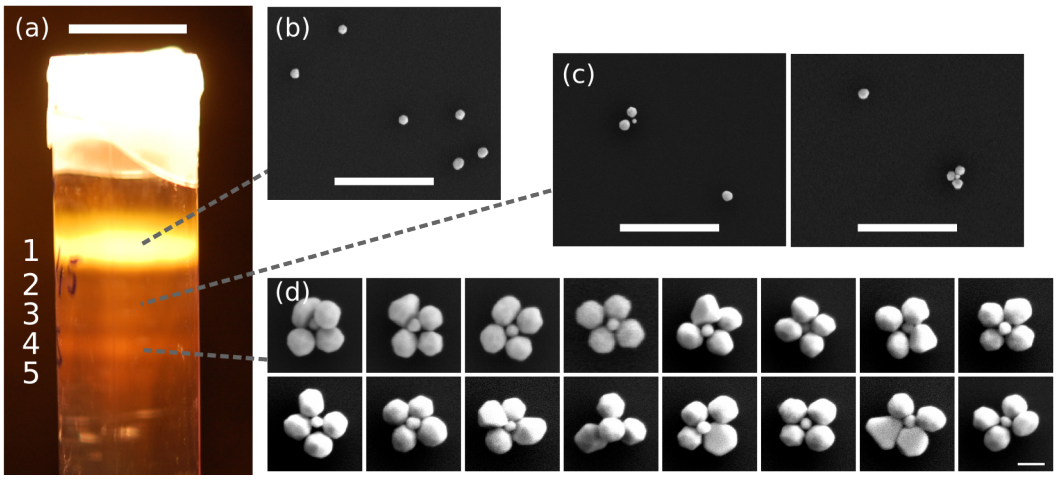

Figure 5.5: (a) Photograph of density gradient column containing a mixture of 100 nm and 50 nm gold particles, labeled with complementary DNA strands, after centrifugation. Scale bar is 1 cm. (b) Scanning electron micrograph of the top band, showing that it contains unbound 100 nm particles. Scale bar is 1 μm. (c) Below the top band are dimers and trimers, as well as some singlets. Scale bar is 1 μm. (d) SEM images of tetramers (distorted tetrahedra) found in the fourth band. Scale bar is 100 nm.

Scanning electron microscopy reveals that the bright band at the top of the density gradient column after centrifugation contains unbound large particles, as shown in Figure 5.5(a)-(b). Very few particles are in contact with other particles in this sample, indicating little non-specific aggregation in this band and negligible contamination of this band from the other bands in the tube. The bands just below the bright band at the top are faint. Dimers appear in the second band and trimers in the third, but there are also many unbound 100 nm particles, as shown in Figure 5.5(c). The contamination of these bands by unbound particles likely occurs because some of the unbound particles from the top band mix into the bands below during extraction.

The fourth band contains many tetramers, as shown in Figure 5.5(d). Most of the tetramers lie flat on the silicon wafer, most likely due to capillary forces during drying. Because the size ratio of the large to small spheres, $\alpha = R_{\text{large}}/R_{\text{small}} \approx 2:1$, is small, any tetramer that forms has sufficiently large gaps so that the large spheres could rearrange on the surface of the small particle [91]. We also observed this phenomenon in previous experiments [129] on dried clusters of DNA-labeled gold nanoshells. In this sense, these flattened clusters are a limiting case of distorted tetrahedra.

Nevertheless, the density gradient and SEM images indicate that self-assembly in this colloidal mixture yields a substantial percentage of tetramers. A random sphere parking model predicts [91] roughly a 60% yield of tetramers and 40% yield of pentamers at this size ratio. In our experiments we see many dimers and trimers, however. The presence of clusters smaller than tetramers may be due to the length of the DNA strands, which is comparable to the particle sizes. Single-stranded DNA has a persistence length of 1 - 2 nm in a 100 mM NaCl solution [147], so multiple strands on one particle can associate with strands on an adjacent particle. As a result, on each small particle, the percentage of DNA that is free to form new duplexes decreases faster as the cluster grows than it would if the strands were much smaller than the particle size [129]. The random parking model may need to be modified when the interactions are mediated by ssDNA comparable in size to the nanoparticles. Furthermore, neither of the particle species is particularly spherical or monodisperse, which limits the relevance of a random-parking description and broadens the expected cluster size distribution [91].

5.4.2 Spherical Particles

The ideal particles for self-assembly in this experiment therefore are not polyhedral gold nanocrystals but rather monodisperse gold nanospheres. We can prepare such particles with the method described in Chapter 2, but we find evidence of some non-specific aggregation between these particles. Density gradient centrifugation of the control sample shows a wide bright band, as shown in Figure 5.6(a). This band is not as sharp as the bright band resulting from density gradient centrifugation of DNA-labeled 100 nm gold particles, as shown in Figure 5.4(a). The bottom portion of this band contains clusters of gold nanospheres, as determined by SEM analysis. The appearance of these clusters in the absence of any oppositely charged particles indicates that the gold nanospheres are not sufficiently stable to obtain a high yield of tetrahedra.

Nevertheless, the gold nanospheres bind specifically to negatively charged particles in mixtures. In one set of experiments, we use 42-nm carboxylate-modified polystyrene nanospheres as the small particle species. Density gradient centrifugation of a mixture again yields a wide bright band, as shown in Figure 5.6(b). SEM analysis shows that the bottom portion of the band contains clusters of gold spheres without any polystyrene particles as well as aggregates containing both kinds of particles. Some aggregates of polystyrene particles appear in this mixture as well, perhaps as a consequence of the way in which they are washed. The significant amount of non-specific aggregation in this system results in poor control over cluster self-assembly.

In another set of experiments, we mix the positively charged gold nanospheres with smaller citrate-stabilized gold particles labeled with DNA strands. The citrate-

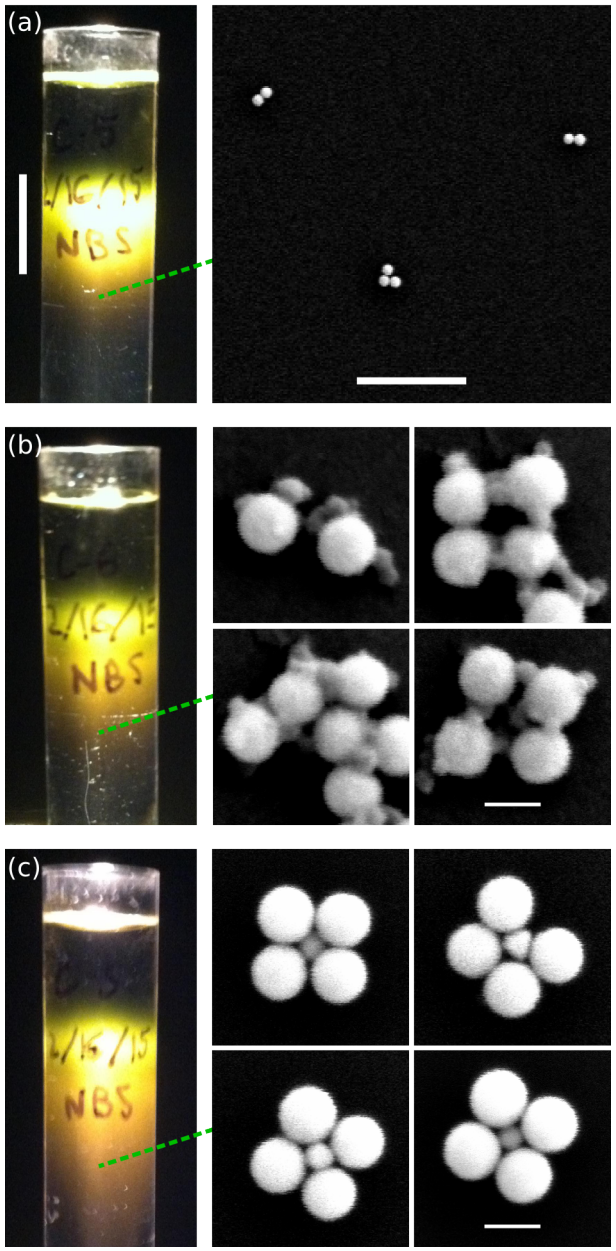

Figure 5.6: Photographs of mixtures of nanoparticles after centrifugation in density gradient columns (left) and scanning electron micrographs of samples extracted from the bottom of the wide band in each column (right). Scale bar is 1 cm for photographs. (a) A control sample of spherical gold crystals in 1 mM NaCl shows non-specific aggregation. Scale bar for electron micrograph is 1 μm. (b) A mixture of spherical gold crystals and 42 nm carboxylate-modified polystyrene particles. Scale bar is 100 nm. (c) A mixture of spherical gold crystals and 50 nm DNA-labeled gold particles. Scale bar is 100 nm.

stabilized gold particles are less spherical than polystyrene particles [132], but the DNA strands give them a large negative charge [148] so that they are stable at even higher salt concentrations [32]. Furthermore, the interaction between the DNA strands on the small particles and polyDADMAC on the surface of the larger nanospheres is precisely the same interaction by which DNA-labeled particles stick to the surface of positively charged silicon wafers in our SEM sample preparation technique.

The results of one of these experiments are shown in Figure 5.6(c). Again there is a single wide band in the density gradient column, rather than well-resolved bands corresponding to clusters of different sizes, owing to non-specific binding between the large gold particles. However, we also find many clusters containing four uniform 100-nm gold spheres bound to a single DNA-labeled 50-nm particle. These clusters constitute a minority of the self-assembly products; non-specifically aggregated gold spheres are the majority component. However, the presence of the tetramers suggests that at higher salt concentrations this system could show strong, specific binding corresponding to random sphere parking [91]. If the stability of the gold nanospheres could be improved, then it should be possible to achieve self-assembly of tetrahedral clusters in high yield.

5.5 Conclusion

Our results demonstrate two laboratory techniques that can be used to characterize clusters assembled from nanoparticles. While density gradient centrifugation has been used to separate clusters of microspheres [51, 52, 55], here we show that it can separate irregular clusters of metal nanoparticles. Even dilute species in a 10 μL

sample can be identified by visual inspection of the density gradient column, making this a valuable technique for bulk characterization and purification. Second, we have demonstrated a method to characterize individual self-assembled nanostructures on a dry substrate without incurring the coffee ring effect. By adsorbing suspended clusters to a charged substrate and then rinsing the fluid away, we minimize the effects of capillary forces during drying, which would otherwise obscure cluster sizes and geometry. Together these methods deliver important information about nano-scale self-assembly products. They could be implemented to better understand systems from DNA origami [149] to virus capsids [150] and metafluids [61].

More importantly, we have shown that random parking is a promising route to bulk production of tetrahedral plasmonic nanostructures. The yield has not yet been optimized, but the data indicate that strong, specific, nonequilibrium binding is attainable in a mixture of gold nanoparticles, thus fulfilling the key requirement for a random parking self-assembly scheme [91].

Chapter 6

Conclusion and Outlook

We have demonstrated several crucial steps toward the practical realization of optical metafluids that could exhibit a negative index of refraction. First, we have shown that it is possible to synthesize spherical, monodisperse building blocks for plasmonic structures. While spherical particles are frequently regarded as the simplest morphologies to prepare in polymeric particles, this is not the case for metals. We now understand how to prepare gold spheres with sizes up to at least 200 nm. This is important because particles of 80 nm or larger are needed to avoid large losses. Similar synthesis strategies are possible with other noble metals [151].

We have also demonstrated that it is possible to achieve at least a 90% yield of tetrahedral clusters through nonequilibrium self-assembly. We accomplished this by taking advantage of a geometric critical point, not previously reported in the mathematics literature, that affects the way spheres randomly and irreversibly bind to – or "park" on – smaller spheres. Tetrahedral clusters are the simplest possible building blocks for isotropic metafluids [41], and no self-assembly scheme that we are

aware of produces clusters of a single type in comparable yield. Furthermore, our simulations show that 100% yield of tetramers is possible in principle, and yields of 70% or more are possible for trimers and octahedra, two other structures that are useful for engineering plasmonic resonances [37, 11].

Finally, we have implemented nonequilibrium self-assembly in binary mixtures of nanoparticles and shown that the random parking model is applicable on this length scale as well. Density gradient centrifugation and electron microscopy reveal that tetrahedral clusters are the dominant species when non-specific aggregation is negligible. That density gradient centrifugation successfully separates disordered nanoparticle clusters into bands for purification demonstrates the power of this technique for characterizing the results of colloidal self-assembly, even with nanoscale components. The technique may be particularly important for separating clusters from unbound nanoparticles, a by-product of any random-parking assembly scheme. The combination of random parking for high yield of tetrahedra with this purification method could allow the unbound particles to be separated and reused so that, ultimately, none of the building blocks are wasted.

6.1 Opportunities for Further Investigation

Our results cast light on important areas for further inquiry, many of which we continue to actively investigate. For instance, non-specific aggregation must be eliminated in our spherical gold particles. We hypothesize that this aggregation occurs because individual polyDADMAC chains can form bridges between particles. This hypothesis would also account for why polyDADMAC-covered particles bind to a

substrate coated with the same material. It may be possible to solve this problem by functionalizing the gold nanospheres with a thiolated polymer after the etching reaction is complete, to saturate any exposed regions of the gold surface and sterically stabilize the nanospheres. If this functionalization does not inhibit further functionalization with oligonucleotides, the particles would become versatile reagents in directed self-assembly schemes.

Another important challenge is creating regular tetrahedra from our nonequilibrium self-assembly method. Although random sphere parking results in tetramers in theoretically 100% yield, the clusters are disordered tetrahedra, and the separation gaps between the particles vary. The asymmetry makes it impossible to achieve uniform and isotropic resonances [41], and the gaps allow capillary forces to flatten clusters during drying. As a consequence, it is difficult to measure optical properties of individual, undistorted clusters.

It may be possible to solve both of these problems using another geometric trick: changing the sphere size ratio after the clusters self-assemble. One might assemble tetramers in high yield at the critical size ratio $\alpha_c = 1 + \sqrt{2}$, as illustrated in Figure 6.1(a), and then increase the size ratio to

$$\alpha \to \frac{\sqrt{2}}{\sqrt{3} - \sqrt{2}} \approx 4.45. \tag{6.1}$$

Above this size ratio the maximum parking number drops to 3 [13, 124], which means that the large spheres in a tetramer are geometrically constrained to adopt tetrahedral symmetry in order to maintain contact with the small sphere. It may be possible to implement this scheme by substituting a thermoresponsive nanogel, such

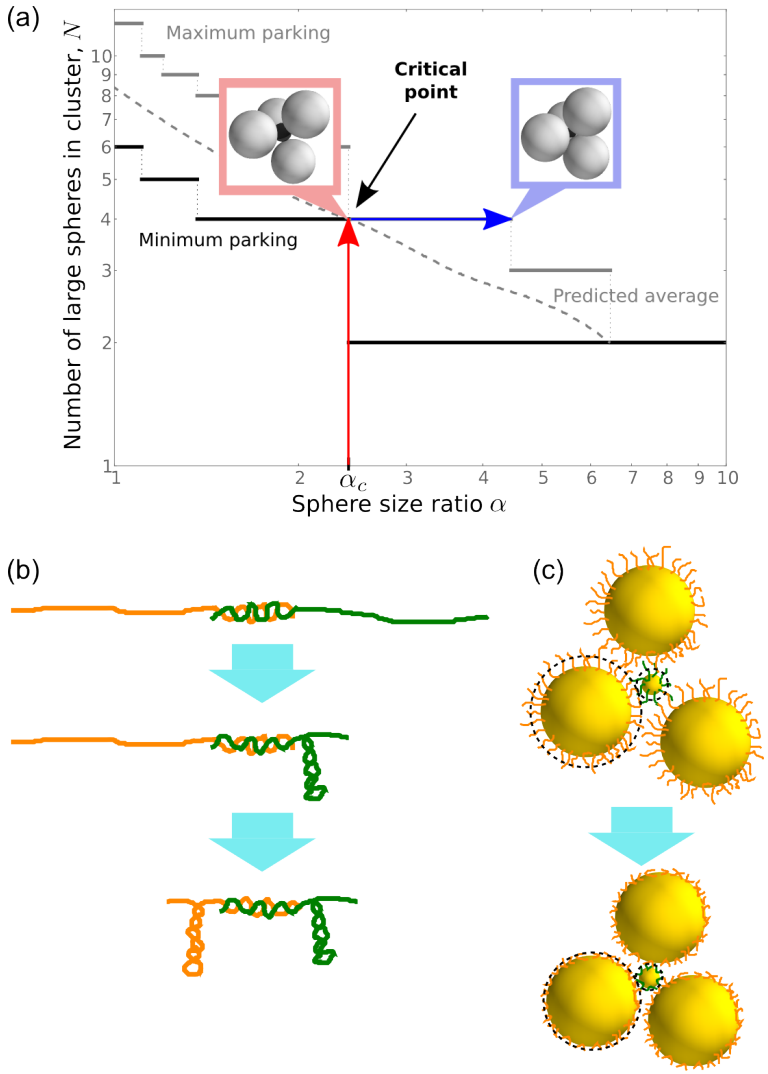

Figure 6.1: A possible strategy for self-assembly of regular tetrahedra in high yield: (a) Tetramers assemble in high yield through random parking at the critical size ratio (red arrow). If we then adjust the size ratio (blue arrow), we can turn them into regular tetrahedra. (b) One way to do this is through the use of DNA strands (orange and green) that form hairpins, decreasing the length of the tethers between the particles. The hairpinning changes the effective size ratio (c) by making the shell of DNA surrounding each particle thinner (dashed black circles), and in turn making the separation gaps between the particles more uniform.

as poly(N-isopropylacrylamide) or PNIPAm, for the small sphere [126]. PNIPAm particles as small as 42 nm shrink to 55% of their initial diameter as the temperature rises from 28 °C to 40 °C [152], which is enough to change the size ratio in a binary mixture from $\alpha_c \approx 2.41$ to $\alpha \approx 4.38$, almost precisely the desired shift. Moreover, they are negatively charged and thus serve as an ideal small-particle species to mix with positively charged gold nanospheres. We are experimentally investigating this system in collaboration with Dr. Jin-Gyu Park.

It may also be possible to adjust the size ratio after clusters self-assemble using DNA nanotechnology. In binary mixtures of DNA-labeled nanoparticles, the shell of DNA surrounding each particle must be taken into account in determining the effective size ratio of the mixture. It may be possible to modify our DNA sequences so that the spacer portion of each sequence forms a hairpin when the temperature falls below some threshold, as illustrated in Figure 6.1(b). The hairpin formation could pull the large particles closer to the small particle and to one another, as depicted in Figure 6.1(c), increasing the effective size ratio and reconfiguring the structure [153] to make the separation gaps between the gold nanoparticles more uniform. Yet another solution is to replace the small particle with a DNA construct or other nanostructure with symmetric and specific binding sites [61] to achieve more control over the geometry of the structure than one can obtain through random parking. My colleague Nabila Tanjeem is investigating this option.

We also need to investigate other materials to make the nanostructures themselves. In the first proposal of a metafluid, the authors noted that the high losses in gold would be problematic and that volume fractions greater than 50% would be necessary

to achieve $\mu < 0$ in a metafluid made with gold nanoclusters [41]. It may be possible to avoid such large volume fractions by using a transition-metal nitride instead of gold. The dielectric function of titanium nitride (TiN) is similar to that of gold in the visible, but ε_r of TiN has a smaller negative real part (ε_r') and a larger imaginary part (ε_r'') [154]. Consequently, TiN's refractive index (n) is larger than gold's and its absorption index (k) is smaller. As a result, many recent studies have examined it as a material for building plasmonic nanostructures [155, 156, 157, 158]. These studies predict that TiN should yield greater field enhancement than gold and figures of merit that are orders of magnitude higher than gold in some geometries. Further work is required to understand whether TiN or a related material could be used to make isotropic resonators for metafluids. If so, it will be necessary to develop synthesis schemes for TiN nanoparticles that can be used in our self-assembly strategies.

Lastly, our work raises some fundamental questions about the physics of nonequilibrium self-organization. For instance, random sphere parking requires irreversible interactions. As a consequence, it is possible to achieve 100% yield of tetramers, an unexpected result. Is such a high yield possible in an equilibrium system? How do the yield curves change for random parking of shapes other than spheres? Can this technique be extended to mixtures of three or more species of particles with different types of interactions? Is it experimentally possible to achieve 100% yield of trimers in a two-dimensional system with random parking?

Our work on the synthesis of gold nanospheres raises questions about crystals out of equilibrium as well. A slow chemical reaction can render the surface tension of a gold crystal effectively isotropic, resulting in spherical crystals. What other sur-

face morphologies are accessible with slow reactions that do not reach equilibrium? Over what range of metals and other crystalline materials can this technique be applied? Can it be extended to crystals composed of molecules such as DNA [159] or crystals made from even larger building blocks, such as nanoparticle superlattices [136]? Throughout the research I have described in this thesis, nonequilibrium statistical physics results in surprising phenomena which happen to be quite useful for our purposes. These examples demonstrate the possibilities for other nonequilibrium self-assembly schemes.

6.2 Final Remarks

It has been fifteen years since Pendry proposed negative refraction as a means of perfect lensing [19] and eight since Urzhumov *et al.* introduced the concept of an isotropic metafluid [41]. It has been my privilege to make contributions towards realizing these goals during my graduate studies. Throughout this time, the plasmonics and metamaterials community has brought intriguing new physics and experimental possibilities to light. In the arena of colloidal self-assembly, the relationship between physics and geometry has led to particularly fruitful discoveries, while we are only just beginning to explore the vast array of possibilities enabled by DNA nanotechnology. I look forward to the exciting results and provocative questions that these fields will continue to raise over the next several years.

Appendix A

Connection Between Spherical Covering and Minimum Parking

Here we verify that the best known coverings are also optimal solutions to the minimum parking problem. For a given configuration of N "parked" points on a unit sphere, let the *covering radius* r_c be the maximum distance between any point on the sphere to the nearest parked point. Let the *packing radius* r_p be (half) the minimum of the pairwise distances between the parked points. If the parked points represent centers of circles with some radius r, it is impossible to add another circle without overlapping a parked one if and only if the covering radius is less than $2r$. The circles that are already parked do not overlap provided that the packing radius is greater than r. Therefore, if we are given an optimal solution to the covering problem, that

is, one that minimizes the covering radius for a given N, it will also be the optimal minimal parking configuration if the covering radius is less than 2 times the packing radius.

We manually verify that the best known coverings satisfy this constraint for $N \in \{4, \ldots, 130\}$ by calculating the packing radius for each optimal known covering, obtained from ref. [124]. Table A.1 shows the covering radius r_c, packing diameter $2r_p$, and difference (in degrees). The difference is always positive, confirming our statement.

Table A.1: Packing diameters and covering radii for different cluster sizes N, measured in degrees, and the differences between them. Because the differences are always positive, we conclude that the optimal covering configuration is also the optimal minimal parking configuration, at least for $N \in \{4, \ldots, 130\}$.

N	$2r_p$	r_c	$2r_p - r_c$
4	109.47	70.53	38.94
5	90.00	63.43	26.57
6	90.00	54.74	35.26
7	72.00	51.03	20.97
8	61.76	48.14	13.62
9	68.97	45.88	23.09
10	65.53	42.31	23.22

Table A.1: (Continued)

N	$2r_p$	r_c	$2r_p - r_c$
11	50.65	41.43	9.22
12	63.43	37.38	26.06
13	46.23	37.07	9.16
14	52.58	34.94	17.64
15	45.67	34.04	11.63
16	50.48	32.90	17.58
17	41.63	32.09	9.54
18	45.53	31.01	14.51
19	40.73	30.37	10.36
20	40.01	29.62	10.39
21	39.45	28.82	10.62
22	40.70	27.81	12.89
23	38.99	27.48	11.51
24	36.67	26.81	9.86
25	36.75	26.33	10.42
26	35.12	25.84	9.27
27	38.06	25.25	12.81
28	35.87	24.66	11.21
29	33.86	24.37	9.50
30	31.18	23.88	7.30

Table A.1: (Continued)

N	$2r_p$	r_c	$2r_p - r_c$
31	29.94	23.61	6.33
32	37.38	22.69	14.69
33	26.61	22.59	4.02
34	30.82	22.33	8.49
35	27.98	22.07	5.90
36	28.78	21.70	7.08
37	31.22	21.31	9.91
38	30.31	21.07	9.24
39	30.73	20.85	9.87
40	30.13	20.47	9.66
41	27.71	20.32	7.39
42	28.34	20.05	8.29
43	27.27	19.84	7.43
44	26.36	19.64	6.72
45	25.15	19.42	5.73
46	29.11	19.16	9.96
47	25.38	18.99	6.38
48	27.70	18.69	9.01
49	24.93	18.59	6.33
50	28.01	18.30	9.71

Table A.1: (Continued)

N	$2r_p$	r_c	$2r_p - r_c$
51	24.30	18.20	6.10
52	24.24	18.05	6.19
53	22.56	17.88	4.68
54	25.58	17.68	7.90
55	24.06	17.52	6.54
56	24.89	17.35	7.54
57	23.98	17.18	6.80
58	23.72	17.02	6.70
59	23.69	16.90	6.79
60	24.67	16.77	7.90
61	20.50	16.64	3.86
62	20.43	16.49	3.94
63	21.60	16.37	5.23
64	21.34	16.19	5.15
65	20.78	16.11	4.66
66	21.61	15.96	5.66
67	21.32	15.86	5.46
68	21.74	15.72	6.02
69	20.41	15.60	4.82
70	21.47	15.50	5.98

Table A.1: (Continued)

N	$2r_p$	r_c	$2r_p - r_c$
71	21.46	15.39	6.07
72	23.06	15.14	7.92
73	17.51	15.12	2.39
74	17.95	15.03	2.92
75	20.02	14.95	5.07
76	19.08	14.85	4.23
77	22.03	14.74	7.29
78	19.14	14.66	4.49
79	19.77	14.56	5.21
80	19.94	14.45	5.49
81	19.07	14.38	4.69
82	20.40	14.29	6.11
83	17.08	14.22	2.86
84	19.93	14.12	5.81
85	19.92	14.05	5.88
86	19.89	13.96	5.93
87	18.70	13.88	4.81
88	19.80	13.79	6.01
89	19.76	13.71	6.05
90	19.83	13.62	6.21

Table A.1: (Continued)

N	$2r_p$	r_c	$2r_p - r_c$
91	17.18	13.56	3.62
92	17.83	13.49	4.34
93	18.75	13.43	5.32
94	19.15	13.35	5.81
95	18.54	13.29	5.25
96	19.21	13.21	6.00
97	18.38	13.14	5.24
98	18.99	13.06	5.93
99	19.06	13.00	6.06
100	18.58	12.94	5.64
101	18.67	12.87	5.80
102	17.63	12.81	4.82
103	17.51	12.74	4.77
104	18.49	12.67	5.82
105	18.94	12.62	6.32
106	17.66	12.56	5.10
107	18.62	12.50	6.13
108	18.10	12.43	5.67
109	18.23	12.38	5.85
110	18.40	12.30	6.10

Table A.1: (Continued)

N	$2r_p$	r_c	$2r_p - r_c$
111	18.70	12.25	6.45
112	18.71	12.19	6.52
113	18.28	12.15	6.14
114	16.87	12.10	4.78
115	17.42	12.05	5.37
116	16.27	11.99	4.28
117	17.67	11.94	5.73
118	17.71	11.89	5.83
119	17.09	11.84	5.25
120	17.25	11.79	5.47
121	17.56	11.73	5.83
122	17.70	11.68	6.02
123	14.38	11.64	2.74
124	14.14	11.59	2.55
125	17.38	11.54	5.84
126	17.07	11.49	5.58
127	16.54	11.45	5.09
128	16.50	11.41	5.09
129	16.98	11.36	5.62
130	16.95	11.32	5.63

Appendix B

Functionalization of Gold Nanoparticles with DNA

This procedure is based on a protocol I learned from Dazhi "Peter" Sun, while visiting Oleg Gang's group at the Center for Functional Nanomaterials (CFN) at Brookhaven National Laboratory (BNL). Long wait times are in bold for ease of planning. The entire procedure can be completed in just a couple of days if all materials are on hand and the required lab equipment is available.

B.1 Materials

- Gold nanoparticles (Au NPs) in suspension, stabilized with citrate[1]

[1] According to Peter, the problem with surfactants other than citrate is that they may tightly bind with Au, thus making the thiolization less efficient. You may need longer time for salting with thiol-DNA, i.e. instead of 30min every round, you may need 1 hour with longer sonication time. It is also helpful to add some more thiolated DNA every time you add salt.

- Thiolated DNA strands as received from IDT (order 1 µmol of each, use HPLC purification, 50 bases total, 15 bases in sticky end). The particle stability may depend on the DNA sequence and length [160, 32].[2] Note that IDT synthesizes DNA starting at the 3' end and most of the errors during synthesis are truncation errors. Therefore, if the thiol group is on the 5' end, the purification may not be important or have much effect.

- Dithiothreitol (DTT) (Powder, RPI Corp. This should smell bad. If it doesn't smell bad, it's expired.)

- Sephadex columns (one for each DNA sequence). illustra, NAP-5 columns, Sephadex G-25 DNA Grade, 17-0853-02, 50 purifications, contains 0.15% kathon CG as preservative. (These should arrive with Sephadex gel in them already. They can be stored at room temperature.)

- Deionized water

- Bucket of ice

- Sodium dodecyl sulfate (SDS)

- Syringes and filters for filtering SDS solution

- Borate buffer (Thermo Scientific, 20X Borate Buffer, product no. 28341, 500 mL bottle, store at room temperature) or phosphate buffer

[2] According to Peter, generally in experiments, Au functionalized with shorter DNA is less stable, especially for large particles. He normally uses 30 bases or higher. If you use a longer salting time and add more DNA gradually, it may help increase the DNA coverage and make the particles more stable.

- Sodium chloride (NaCl)

B.2 Procedure

B.2.1 Cleave Disulfide Bonds in Thiolated DNA

IDT provides additional information about why it is important to reduce thiol-modified oligos before use. Some groups use different methods depending on whether the thiol group is on the 3' or 5' end of the oligo [161]. Peter said that the following method is ok for both 3' and 5' modifications with thiol.

1. Prepare a 0.1 M solution of DTT (154.2 molecular weight) in deionized water. 200 μL of this will be added to each DNA vial. This can be stored in the freezer when not in use.

2. If using DTT solution from freezer, remove from freezer and **wait about an hour** for it to come to room temperature.

3. Centrifuge DNA vial as received from IDT. Check that you can see the blob of DNA at the bottom of the tube.

4. Add 200 μL of 0.1 M DTT solution to each DNA vial. (No additional water or buffer added to DNA.)

5. Vortex the DNA vials for 5 seconds and centrifuge them briefly in a small benchtop centrifuge.

6. **Wait one hour**. (Begin preparing sephadex columns while you wait though.)

B.2.2 Use Sephadex Columns to Remove DTT from DNA

1. Prepare a sephadex column for each DNA strand.

   (a) Mount the column on a ring stand. Place a Falcon tube below each column to collect waste. Label each column with the DNA sequence that you will filter through it.

   (b) Open the column and, before adding anything to it, let water drip out of the column until the water level is at the top of the gel.

   (c) Once the water level is at the top of the gel, add 1 mL of deionized water (or buffer), and let it keep dripping until the water level again comes down to the top surface of the gel.

   (d) Repeat the previous step a total of 10 times (adding 1 mL of DI water at a time, to wash the gel and make sure it is in the desired buffer prior to adding DNA and DTT). When doing this, it is not necessary to wait for the water level to come all the way down to the gel's top surface each time. You can just wait a few minutes between adding water each time.

2. Prepare 4 microcentrifuge tubes for each DNA sequence. Label the tubes with the DNA sequence name and a number for the order in which they'll be used for the elution.

3. Prepare a small bucket of ice. (Keep the DNA on ice after elution to prevent the thiols from forming disulfide bonds again.)

4. Position the first of the four microcentrifuge tubes below the column. Make sure the columns are at least 1 cm above the microcentrifuge tubes.

5. Add the full 200 μL of DNA/DTT solution to the column. Immediately add 500 μL of water or buffer, and collect what comes out in the microcentrifuge tube. (While this is in progress, the same can be done for other DNA sequences.)

6. Once it stops dripping, seal the microcentrifuge tube and immediately put it in the ice bucket. (Keep the tubes cold when working with them so that the disulfide bonds won't form again quickly.)

7. Replace the microcentrifuge tube with the next one, and add another 500 μL of water or buffer and repeat the process with the other tubes.

8. After all 4 tubes are full, put them in the freezer. Usually the second tube has the highest DNA concentration.

9. Use UV-vis spectrometry to measure the concentration of DNA in the tubes.

   (a) Blank with DI water first. Remember to keep diluted DNA solution on ice until it is necessary to make a measurement.

   (b) Dilute a sample of the DNA solution by a factor of at least 100 for UV-vis measurement. Repeat measurement with different dilutions (e.g. 100, 200, 300) to determine concentration of DNA solution.

   (c) Using extinction coefficient reported by IDT and equation $C = A_{\text{abs}}/\epsilon L$ (Beer-Lambert law), solve for C. Here A_{abs} is measured absorption, ϵ is the extinction coefficient reported by IDT, L is the propagation length

through the liquid in the cuvette, and C is the concentration. Remember to multiply by dilution ratio to get back to original concentration.

10. Return DNA to freezer when done.

B.2.3 Gradually Load DNA onto Gold Nanoparticles

See Hurst *et al.* [32] for details of how many DNA strands can be loaded onto gold nanoparticles as a function of particle size, salt concentration, spacer length and type, etc. For example, aim for 300 DNA strands per 10 nm particle, 10 000 DNA strands per 50 nm particle, or 100 000 DNA strands per 100 nm particle. (Actual loading will be much less than this.)

1. Before adding any DNA to gold nanoparticles, use dynamic light scattering to measure their size (hydrodynamic diameter).

2. Also measure concentration of nanoparticles using UV-vis, if not yet known. For references on gold nanoparticle extinction coefficient and dependence on particle size, see [162, 33].

3. Prepare a 1 wt % SDS solution in water. It's probably a good idea to filter this through a < 1 μm pore membrane. (If using solution from fridge, sonicate for 5 minutes before use.)

4. Vortex the gold nanoparticles for a few seconds.

5. Add 1 mL of the first type of gold nanoparticles to each of 2 microcentrifuge tubes (volume permitting).

6. Add DNA of desired sequence to each of the microcentrifuge tubes in volume that corresponds to the DNA loading that you are aiming for. (See beginning of this section.)

7. Add 50 μL of 20X borate buffer to each tube to increase DNA loading. (To do this, place it in the lid of the microcentrifuge tube so that vortexing will mix it in thoroughly immediately and the buffer will be diluted 20X as intended.)

8. Also add 10 μL of 1 wt % SDS in DI water, only for particles of diameter $\geq$ 30 nm.

9. Vortex tubes for about 5 seconds.

10. Sonicate tubes for 1 minute. Using pipe cleaners to suspend the tubes in the sonicator at the desired depth can be useful in this and future steps.

11. Put the tubes on a rotator at room temperature and begin slowly rotating.

12. **Let the tubes rotate for 1 - 2 hours**. During this time, repeat this process for gold nanoparticles of other sizes. Later we will add salt (but no additional buffer) to adjust the salt concentration. An orbital shaker can also be used for this process. In some groups, they wait much longer at this step (for example, **16 hours**) before proceeding to the next steps. This seems worth a try. For example, see the Supporting Information of [163].

13. Add salt gradually [164, 165, 166] by putting small amounts of concentrated NaCl in the lid of each microcentrifuge tube and then vortexing to mix it in.

    (a) First, centrifuge the tubes for a few seconds.

(b) The amount of salt to add depends on particle size:

- For 10 nm particles, add 20 μL of 2.5 M NaCl to bring overall concentration to approximately 0.05 M NaCl. (To prepare this, add 0.1461g NaCl to 1 mL of water.)
- For 20 nm particles and larger, add 10 μL of 2.5 M NaCl to bring overall concentration to approximately 0.025 M NaCl. Also add roughly 200 DNA strands per particle (about 0.2 μL) to the suspensions of these larger nanoparticles at this time (and more for larger particles).

(c) Vortex intermittently for a few seconds to mix in the salt.

(d) Centrifuge the tubes for a few seconds.

(e) Sonicate all the tubes for 10 seconds.

(f) Return the tubes to the rotator and **wait at least a half hour**.

(g) **Repeat this procedure, adding salt every half hour (or even less often)** to gradually increase the salt concentration to 0.25 M NaCl (could be a bit more for smaller particles and a bit less for larger particles). For larger particles ($\geq$ 50 nm), increase the salt concentration more slowly and also add more DNA solution. During the salting process, you may keep the thawed DNA solution in the refrigerator. In some protocols [167], this process occurs over a period of a few days for optimal DNA loading.

- For 10 nm particles, salting steps should be 20 μL, 20 μL, 40 μL, 40 μL. (4 steps total.)

- For 20 nm particles and larger, salting steps should be 10 μL, 10 μL, 10 μL, 10 μL, 10 μL, 10 μL, 20 μL, 20 μL. (8 steps total but roughly the same overall concentration in the end.) Also add approximately 0.2 μL of DNA solution each time (more for larger particles).
- You may also want to periodically use DLS to measure whether hydrodynamic diameter of particles is in fact increasing with the salting process.

14. When the salting process is finished, **leave the tubes on the rotator overnight**.

15. Return the DNA to the freezer for storage.

B.2.4 Wash Particles to Remove Excess DNA

1. The next morning, remove the tubes from the rotator.

2. Prepare buffer: 1 part 20X borate buffer stock (as before), 19 parts DI water, 0.1 M NaCl. (To make 40 mL of buffer, use 38 mL of DI water, 2 mL of 20X borate buffer stock, and 0.2338 g NaCl.) Filter the buffer through a 0.02 μm membrane. (To add 0.01 wt % SDS to this buffer later, use the more concentrated solution of 1 wt % SDS and add 1 part of this to 99 parts buffer. The SDS is to prevent the particles from sticking to the walls during washing. It's not needed for the assembly process, but also won't hurt the process if it's in the system at that point. Don't add the SDS to the buffer right away.)

3. Centrifuge briefly and then sonicate the tubes, holding them with pipe cleaners.

4. Wash the particles three times each, as follows:

   (a) Centrifuge the particles in order to form a pellet. If you don't see a pellet, repeat at higher speed.

   - For 10 nm particles, centrifuge at about $6600g$ for **1 hour**.
   - For 20 nm particles, centrifuge at about $3000g$ for **1 hour**.
   - For 50 nm particles, centrifuge at about $700g$ for **20 minutes**.
   - For 100 nm particles, centrifuge at about $250g$ for **20 minutes**.

   (b) Remove the supernatant.

   (c) Replace the supernatant with 1 mL of buffer prepared earlier (without SDS added). After the last centrifugation step, resuspend all tubes to 1/10 of the original volume to obtain 10x higher concentration in the end.

   - Note: Only add the SDS for particles $\geq$ 30 nm and only after the first wash step to prevent aggregation, using 10 uL of the 1% SDS solution at a time. Do not add SDS to these particles after resuspending the last time. If you add SDS, you shouldn't see gold particles floating at the top of the liquid after a centrifugation run.
   - If desired, after the last wash and resuspension, combine the contents of the original two tubes.

   (d) Vortex for about 5 seconds.

   (e) Centrifuge on bench for a few seconds.

   (f) Sonicate for about 10 seconds or as needed to make sure particles are redispersed.

(g) **Repeat this procedure for a total of three wash cycles.**

5. Store the particles in the refrigerator after the DNA functionalization and washing are complete.

B.2.5 Characterize Particles after DNA Functionalization

1. Use DLS to measure hydrodynamic radius, if desired, to confirm increase due to DNA functionalization.

2. Use UV-vis to measure concentrations of particles.

   (a) Blank with buffer first.

   (b) Dilute the particles by factors of 2, 4, and 6 for UV-vis measurements. Measure the extinction spectra.

   (c) Using extinction coefficient reported by Au NP vendor and equation $C = A_{\text{abs}}/\epsilon L$ (Beer-Lambert law), solve for C. Here A_{abs} is measured absorption, ϵ is the extinction coefficient reported by the vendor (or calculated using formulae [33]), L is the propagation length through the liquid in the cuvette, and C is the concentration. Remember to multiply by dilution ratio to get back to original concentration. Numbers for C will decrease as you do this because of the noise floor.

3. Return suspensions to refrigerator for storage after this is completed.

Bibliography

[1] V. G. Veselago. The electrodynamics of substances with simultaneously negative values of ε and μ. *Phys.-Usp.*, 10(4):509–514, 1968.

[2] S. A. Ramakrishna. Physics of negative refractive index materials. *Rep. Prog. Phys.*, 68(2):449, 2005.

[3] W. Cai and V. M. Shalaev. *Optical Metamaterials*. Springer, 2010.

[4] P. B. Johnson and R. W. Christy. Optical constants of the noble metals. *Phys. Rev. B*, 6(12):4370–4379, December 1972.

[5] A. Moores and F. Goettmann. The plasmon band in noble metal nanoparticles: an introduction to theory and applications. *New J. Chem.*, 30(8):1121–1132, 2006.

[6] J. B. Pendry, A. J. Holden, D. J. Robbins, and W. J. Stewart. Magnetism from conductors and enhanced nonlinear phenomena. *IEEE Trans. Microwave Theory Tech.*, 47(11):2075–2084, 1999.

[7] R. A. Shelby, D. R. Smith, and S. Schultz. Experimental verification of a negative index of refraction. *Science*, 292(5514):77–79, 2001.

[8] D. Schurig, J. J. Mock, B. J. Justice, S. A. Cummer, J. B. Pendry, A. F. Starr, and D. R. Smith. Metamaterial electromagnetic cloak at microwave frequencies. *Science*, 314(5801):977–980, 2006.

[9] C. Enkrich, F. Pérez-Willard, D. Gerthsen, J. F. Zhou, T. Koschny, C. M. Soukoulis, M. Wegener, and S. Linden. Focused-ion-beam nanofabrication of near-infrared magnetic metamaterials. *Adv. Mater.*, 17(21):2547–2549, 2005.

[10] N. Liu, H. Guo, L. Fu, S. Kaiser, H. Schweizer, and H. Giessen. Three-dimensional photonic metamaterials at optical frequencies. *Nat. Mater.*, 7(1):31–37, 2008.

[11] J. A. Fan, C. Wu, K. Bao, J. Bao, R. Bardhan, N. J. Halas, V. N. Manoharan, P. Nordlander, G. Shvets, and F. Capasso. Self-assembled plasmonic nanoparticle clusters. *Science*, 328(5982):1135–1138, May 2010.

[12] J. A. Fan, K. Bao, C. Wu, J. Bao, R. Bardhan, N. J. Halas, V. N. Manoharan, G. Shvets, P. Nordlander, and F. Capasso. Fano-like interference in self-assembled plasmonic quadrumer clusters. *Nano Lett.*, 10(11):4680–4685, November 2010.

[13] M. L. Mansfield, L. Rakesh, and D. A. Tomalia. The random parking of spheres on spheres. *J. Chem. Phys.*, 105(8):3245–3249, May 1996.

[14] A. Kwan, J. Dudley, and E. Lantz. Who really discovered Snell's law? *Phys. World*, 15(4):64, 2002.

[15] J. B. Pendry. A chiral route to negative refraction. *Science*, 306(5700):1353–1355, 2004.

[16] J. H. Poynting. On the transfer of energy in the electromagnetic field. *Philos. Trans. R. Soc. London*, pages 343–361, 1884.

[17] J. D. Jackson. *Classical Electrodynamics*. Wiley, 1999.

[18] N. Yu, P. Genevet, M. A. Kats, F. Aieta, J.-P. Tetienne, F. Capasso, and Z. Gaburro. Light propagation with phase discontinuities: generalized laws of reflection and refraction. *Science*, 334(6054):333–337, 2011.

[19] J. B. Pendry. Negative refraction makes a perfect lens. *Phys. Rev. Lett.*, 85(18):3966, 2000.

[20] E. Abbe. Beiträge zur theorie des mikroskops und der mikroskopischen wahrnehmung. *Arch. Mikroskop. Anat.*, 9(1):413–468, 1873.

[21] J. B. Pendry. Perfect cylindrical lenses. *Opt. Express*, 11(7):755–760, 2003.

[22] Z. Liu, H. Lee, Y. Xiong, C. Sun, and X. Zhang. Far-field optical hyperlens magnifying sub-diffraction-limited objects. *Science*, 315(5819):1686–1686, 2007.

[23] J. C. Maxwell Garnett. Colours in metal glasses, in metallic films, and in metallic solutions. ii. *Philos. Trans. R. Soc., A*, pages 237–288, 1906.

[24] D. A. G. Bruggeman. Calculation of various physics constants in heterogenous substances i dielectricity constants and conductivity of mixed bodies from isotropic substances. *Ann. Phys.*, 24(7):636–664, 1935.

[25] T. C. Choy. *Effective Medium Theory*. Clarendon Press, 1999.

[26] M. Rahm, S. A. Cummer, D. Schurig, J. B. Pendry, and D. R. Smith. Optical design of reflectionless complex media by finite embedded coordinate transformations. *Phys. Rev. Lett.*, 100(6):063903, 2008.

[27] E. E. Narimanov and A. V. Kildishev. Optical black hole: Broadband omnidirectional light absorber. *Appl. Phys. Lett.*, 95(4):041106, 2009.

[28] J. B. Pendry, A. Aubry, D. R. Smith, and S. A. Maier. Transformation optics and subwavelength control of light. *Science*, 337(6094):549–552, 2012.

[29] M. M. Alvarez, J. T. Khoury, T. G. Schaaff, M. N. Shafigullin, I. Vezmar, and R. L. Whetten. Optical absorption spectra of nanocrystal gold molecules. *J. Phys. Chem. B*, 101(19):3706–3712, 1997.

[30] N. W. Ashcroft and N. D. Mermin. *Solid State Physics*. Holt, Rinehart and Winston, New York, 1976.

[31] R. Lässer and N. V. Smith. Interband optical transitions in gold in the photon energy range 2–25 eV. *Solid State Commun.*, 37(6):507–509, 1981.

[32] S. J. Hurst, A. K. R. Lytton-Jean, and C. A. Mirkin. Maximizing DNA loading on a range of gold nanoparticle sizes. *Anal. Chem.*, 78(24):8313–8318, 2006.

[33] X. Liu, M. Atwater, J. Wang, and Q. Huo. Extinction coefficient of gold nanoparticles with different sizes and different capping ligands. *Colloids Surf., B*, 58(1):3–7, 2007.

[34] H. C. van de Hulst. *Light Scattering by Small Particles*. Dover Publications, 1981.

[35] M. A. Van Dijk, A. L. Tchebotareva, M. Orrit, M. Lippitz, S. Berciaud, D. Lasne, L. Cognet, and B. Lounis. Absorption and scattering microscopy of single metal nanoparticles. *Phys. Chem. Chem. Phys.*, 8(30):3486–3495, 2006.

[36] J. N. Anker, W. P. Hall, O. Lyandres, N. C. Shah, J. Zhao, and R. P. Van Duyne. Biosensing with plasmonic nanosensors. *Nat. Mater.*, 7(6):442–453, 2008.

[37] A. Alù and N. Engheta. The quest for magnetic plasmons at optical frequencies. *Opt. Express*, 17(7):5723–5730, March 2009.

[38] L. D. Landau, J. S. Bell, M. J. Kearsley, L. P. Pitaevskii, E. M. Lifshitz, and J. B. Sykes. *Electrodynamics of Continuous Media*, volume 8. Pergamon Press, 1984.

[39] V. M. Shalaev, W. Cai, U. K. Chettiar, H.-K. Yuan, A. K. Sarychev, V. P. Drachev, and A. V. Kildishev. Negative index of refraction in optical metamaterials. *Opt. Lett.*, 30(24):3356–3358, 2005.

[40] J. Valentine, S. Zhang, T. Zentgraf, E. Ulin-Avila, D. A. Genov, G. Bartal, and X. Zhang. Three-dimensional optical metamaterial with a negative refractive index. *Nature*, 455(7211):376–379, 2008.

[41] Y. A. Urzhumov, G. Shvets, J. A. Fan, F. Capasso, D. Brandl, and P. Nordlander. Plasmonic nanoclusters: a path towards negative-index metafluids. *Opt. Express*, 15(21):14129–14145, 2007.

[42] D. B. Wolfe, R. S. Conroy, P. Garstecki, B. T. Mayers, M. A. Fischbach, K. E. Paul, M. Prentiss, and G. M. Whitesides. Dynamic control of liquid-core/liquid-cladding optical waveguides. *Proc. Natl. Acad. Sci. U. S. A.*, 101(34):12434–12438, 2004.

[43] P. M. Moran, S. Dharmatilleke, A. H. Khaw, K. W. Tan, M. L. Chan, and I. Rodriguez. Fluidic lenses with variable focal length. *Appl. Phys. Lett.*, 88(4):041120, 2006.

[44] E. Prodan, C. Radloff, Naomi J. Halas, and P. Nordlander. A hybridization model for the plasmon response of complex nanostructures. *Science*, 302(5644):419–422, 2003.

[45] H. Wang, D. W. Brandl, P. Nordlander, and N. J. Halas. Plasmonic nanostructures: artificial molecules. *Acc. Chem. Res.*, 40(1):53–62, January 2007.

[46] M. Faraday. Experimental relations of gold (and other metals) to light. *Philos. Trans. R. Soc. London*, 147:145–181, 1857.

[47] J. Turkevich, P. C. Stevenson, and J. Hillier. A study of the nucleation and growth processes in the synthesis of colloidal gold. *Discuss. Faraday Soc.*, 11:55–75, 1951.

[48] G. Frens. Controlled nucleation for the regulation of the particle size in monodisperse gold suspensions. *Nature (London), Phys. Sci.*, 241(105):20–22, January 1973.

[49] S. J. Oldenburg, R. D. Averitt, S. L. Westcott, and N. J. Halas. Nanoengineering of optical resonances. *Chem. Phys. Lett.*, 288(24):243–247, May 1998.

[50] C. Radloff and N. J. Halas. Enhanced thermal stability of silica-encapsulated metal nanoshells. *Appl. Phys. Lett.*, 79(5):674–676, July 2001.

[51] V. N. Manoharan, M. T. Elsesser, and D. J. Pine. Dense packing and symmetry in small clusters of microspheres. *Science*, 301(5632):483–487, 2003.

[52] C. S. Wagner, Y. Lu, and A. Wittemann. Preparation of submicrometer-sized clusters from polymer spheres using ultrasonication. *Langmuir*, 24(21):12126–12128, 2008.

[53] R. J. Hinton and M. Dobrota. Density gradient centrifugation. In T. S. Work and E. Work, editors, *Laboratory Techniques in Biochemistry and Molecular Biology*, volume 6. Elsevier/North-Holland, New York, 1978.

[54] S. Sacanna, W. T. M. Irvine, P. M. Chaikin, and D. J. Pine. Lock and key colloids. *Nature*, 464(7288):575–578, 2010.

[55] Y. Wang, Y. Wang, D. R. Breed, V. N. Manoharan, L. Feng, A. D. Hollingsworth, M. Weck, and D. J. Pine. Colloids with valence and specific directional bonding. *Nature*, 491(7422):51–55, 2012.

[56] Y. Xia, Y. Yin, Y. Lu, and J. McLellan. Template-assisted self-assembly of spherical colloids into complex and controllable structures. *Adv. Funct. Mater.*, 13(12):907–918, 2003.

[57] J. A. Fan, K. Bao, L. Sun, J. Bao, V. N. Manoharan, P. Nordlander, and F. Capasso. Plasmonic mode engineering with templated self-assembled nanoclusters. *Nano Lett.*, 12(10):5318–5324, 2012.

[58] A. S. Urban, X. Shen, Y. Wang, N. Large, H. Wang, M. W. Knight, P. Nordlander, H. Chen, and N. J. Halas. Three-dimensional plasmonic nanoclusters. *Nano Lett.*, 13(9):4399–4403, 2013.

[59] S. Mühlig, A. Cunningham, S. Scheeler, C. Pacholski, T. Bürgi, C. Rockstuhl, and F. Lederer. Self-assembled plasmonic core-shell clusters with an isotropic magnetic dipole response in the visible range. *ACS Nano*, 5(8):6586–6592, 2011.

[60] S. N. Sheikholeslami, H. Alaeian, A. L. Koh, and J. A. Dionne. A metafluid exhibiting strong optical magnetism. *Nano Lett.*, 13(9):4137–4141, 2013.

[61] J. Fontana, W. J. Dressick, J. Phelps, J. E. Johnson, R. W. Rendell, T. Sampson, B. R. Ratna, and C. M. Soto. Nanoclusters: Virus-templated plasmonic nanoclusters with icosahedral symmetry via directed self-assembly. *Small*, 10(15):3196–3196, 2014.

[62] J. Zhou, J. An, B. Tang, S. Xu, Y. Cao, B. Zhao, W. Xu, J. Chang, and J. R. Lombardi. Growth of tetrahedral silver nanocrystals in aqueous solution and their SERS enhancement. *Langmuir*, 24(18):10407–10413, September 2008.

[63] C. Li, K. L. Shuford, M. Chen, E. J. Lee, and S. O. Cho. A facile polyol route to uniform gold octahedra with tailorable size and their optical properties. *ACS Nano*, 2(9):1760–1769, September 2008.

[64] M. R. Langille, J. Zhang, M. L. Personick, S. Li, and C. A. Mirkin. Stepwise evolution of spherical seeds into 20-fold twinned icosahedra. *Science*, 337(6097):954–957, August 2012.

[65] S. J. Tan, M. J. Campolongo, D. Luo, and W. Cheng. Building plasmonic nanostructures with DNA. *Nat. Nanotechnol.*, 6(5):268–276, 2011.

[66] F. Shafiei, F. Monticone, K. Q. Le, X.-X. Liu, T. Hartsfield, A. Alù, and X. Li. A subwavelength plasmonic metamolecule exhibiting magnetic-based optical Fano resonance. *Nat. Nanotechnol.*, 8(2):95–99, February 2013.

[67] Y. Wang, D. Wan, S. Xie, X. Xia, C. Z. Huang, and Y. Xia. Synthesis of silver octahedra with controlled sizes and optical properties via seed-mediated growth. *ACS Nano*, 7(5):4586–4594, May 2013.

[68] C. Noguez. Surface plasmons on metal nanoparticles: the influence of shape and physical environment. *J. Phys. Chem. C*, 111(10):3806–3819, March 2007.

[69] H.-X. Lin, J.-M. Li, B.-J. Liu, D.-Y. Liu, J. Liu, A. Terfort, Z.-X. Xie, Z.-Q. Tian, and B. Ren. Uniform gold spherical particles for single-particle surface-enhanced raman spectroscopy. *Phys. Chem. Chem. Phys.*, 15(12):4130–4135, February 2013.

[70] L. M. Liz-Marzán. Tailoring surface plasmons through the morphology and assembly of metal nanoparticles. *Langmuir*, 22(1):32–41, January 2006.

[71] J. B. Lassiter, J. Aizpurua, L. I. Hernandez, D. W. Brandl, I. Romero, S. Lal, J. H. Hafner, P. Nordlander, and N. J. Halas. Close encounters between two nanoshells. *Nano Lett.*, 8(4):1212–1218, April 2008.

[72] J. Henzie, S. C. Andrews, X. Y. Ling, Z. Li, and P. Yang. Oriented assembly of polyhedral plasmonic nanoparticle clusters. *Proc. Natl. Acad. Sci. U. S. A.*, 110(17):6640–6645, April 2013.

[73] C. M. Cobley, M. Rycenga, F. Zhou, Z.-Y. Li, and Y. Xia. Controlled etching as a route to high quality silver nanospheres for optical studies. *J. Phys. Chem. C*, 113(39):16975–16982, 2009.

[74] Y. Xiong. Morphological changes in ag nanocrystals triggered by citrate photoreduction and governed by oxidative etching. *Chem. Commun.*, 47:1580–1582, 2011.

[75] D.-K. Lim, K.-S. Jeon, J.-H. Hwang, H. Kim, S. Kwon, Y. D. Suh, and J.-M. Nam. Highly uniform and reproducible surface-enhanced raman scattering from DNA-tailorable nanoparticles with 1-nm interior gap. *Nat. Nanotechnol.*, 6(7):452–460, 2011.

[76] N. Engheta. Circuits with light at nanoscales: Optical nanocircuits inspired by metamaterials. *Science*, 317(5845):1698–1702, September 2007.

[77] J. W. Gibbs. *The collected works of J. Willard Gibbs*, volume 1. Longmans, Green and Co., 1928.

[78] G. Wulff. Zur frage der geschwindigkeit des wachstums und der auflösung der kristallflächen. *Z. kristallogr.*, 34:449–530, 1901.

[79] C. R. Li, N. P. Lu, J. Mei, W. J. Dong, Y. Y. Zheng, L. Gao, K. Tsukamoto, and Z. X. Cao. Polyhedral to nearly spherical morphology transformation of silver microcrystals grown from vapor phase. *J. Cryst. Growth*, 314(1):324–330, January 2011.

[80] S. L. Goodman, G. M. Hodges, L. K. Trejdosiewicz, and D. C. Livingston. Colloidal gold markers and probes for routine application in microscopy. *J. Microsc. (Oxford, U. K.)*, 123(2):201213, 1981.

[81] K. C. Grabar, K. R. Brown, C. D. Keating, S. J. Stranick, S.-L. Tang, and M. J. Natan. Nanoscale characterization of gold colloid monolayers: a comparison of four techniques. *Anal. Chem.*, 69(3):471–477, February 1997.

[82] C. Ciracì, R. T. Hill, J. J. Mock, Y. Urzhumov, A. I. Fernández-Domínguez, S. A. Maier, J. B. Pendry, A. Chilkoti, and D. R. Smith. Probing the ultimate limits of plasmonic enhancement. *Science*, 337(6098):1072–1074, August 2012.

[83] A. B. Tesler, L. Chuntonov, T. Karakouz, T. A. Bendikov, G. Haran, A. Vaskevich, and I. Rubinstein. Tunable localized plasmon transducers prepared by thermal dewetting of percolated evaporated gold films. *J. Phys. Chem. C*, 115(50):24642–24652, December 2011.

[84] S. Hong, K. L. Shuford, and S. Park. Shape transformation of gold nanoplates and their surface plasmon characterization: Triangular to hexagonal nanoplates. *Chem. Mater.*, 23(8):2011–2013, April 2011.

[85] Y. Xia, Y. Xiong, B. Lim, and S. E. Skrabalak. Shape-controlled synthesis of metal nanocrystals: Simple chemistry meets complex physics? *Angew. Chem., Int. Ed.*, 48(1):60103, 2009.

[86] S. M. Foiles, M. I. Baskes, and M. S. Daw. Embedded-atom-method functions for the fcc metals Cu, Ag, Au, Ni, Pd, Pt, and their alloys. *Phys. Rev. B*, 33(12):7983–7991, June 1986.

[87] M. A. Schmidt, D. Y. Lei, L. Wondraczek, V. Nazabal, and S. A. Maier. Hybrid nanoparticle-microcavity-based plasmonic nanosensors with improved detection

resolution and extended remote-sensing ability. *Nat. Commun.*, 3:1108, October 2012.

[88] F. Le, N. Z. Lwin, J. M. Steele, M. Käll, N. J. Halas, and P. Nordlander. Plasmons in the metallic nanoparticle–film system as a tunable impurity problem. *Nano Lett.*, 5(10):2009–2013, October 2005.

[89] J. A. Fan, K. Bao, J. B. Lassiter, J. Bao, N. J. Halas, P. Nordlander, and F. Capasso. Near-normal incidence dark-field microscopy: Applications to nanoplasmonic spectroscopy. *Nano Lett.*, 12(6):2817–2821, 2012.

[90] Y. Zhang, F. Wen, Y.-R. Zhen, P. Nordlander, and N. J. Halas. Coherent fano resonances in a plasmonic nanocluster enhance optical four-wave mixing. *Proc. Natl. Acad. Sci. U. S. A.*, 110(23):9215–9219, 2013.

[91] N. B. Schade, M. C. Holmes-Cerfon, E. R. Chen, D. Aronzon, J. W. Collins, J. A. Fan, F. Capasso, and V. N. Manoharan. Tetrahedral colloidal clusters from random parking of bidisperse spheres. *Phys. Rev. Lett.*, 110(14):148303, April 2013.

[92] G. Peng, U. Tisch, O. Adams, M. Hakim, N. Shehada, Y. Y. Broza, S. Billan, R. Abdah-Bortnyak, A. Kuten, and H. Haick. Diagnosing lung cancer in exhaled breath using gold nanoparticles. *Nat. Nanotechnol.*, 4(10):669–673, 2009.

[93] O. Neumann, A. S. Urban, J. Day, S. Lal, P. Nordlander, and N. J. Halas. Solar vapor generation enabled by nanoparticles. *ACS Nano*, 7(1):42–49, 2013.

[94] Z. Fang, Y.-R. Zhen, O. Neumann, A. Polman, F. J. García de Abajo, P. Nordlander, and N. J. Halas. Evolution of light-induced vapor generation at a liquid-immersed metallic nanoparticle. *Nano Lett.*, 13(4):1736–1742, 2013.

[95] N. Fan, Y. Yang, W. Wang, L. Zhang, W. Chen, C. Zou, and S. Huang. Selective etching induces selective growth and controlled formation of various platinum nanostructures by modifying seed surface free energy. *ACS Nano*, 6(5):4072–4082, May 2012.

[96] J. Rodríguez-Fernández, J. Pérez-Juste, P. Mulvaney, and L. M. Liz-Marzán. Spatially-directed oxidation of gold nanoparticles by au(III)CTAB complexes. *J. Phys. Chem. B*, 109(30):14257–14261, August 2005.

[97] K. Torigoe and K. Esumi. Preparation of colloidal gold by photoreduction of tetracyanoaurate(1-)-cationic surfactant complexes. *Langmuir*, 8(1):59–63, January 1992.

[98] D. Seo, J. C. Park, and H. Song. Polyhedral gold nanocrystals with oh symmetry: from octahedra to cubes. *J. Am. Chem. Soc.*, 128(46):14863–14870, November 2006.

[99] A. S. Barnard, X. M. Lin, and L. A. Curtiss. Equilibrium morphology of face-centered cubic gold nanoparticles >3 nm and the shape changes induced by temperature. *J. Phys. Chem. B*, 109(51):24465–24472, December 2005.

[100] N. Metropolis, A. W. Rosenbluth, M. N. Rosenbluth, A. H. Teller, and E. Teller. Equation of state calculations by fast computing machines. *J. Chem. Phys.*, 21(6):1087–1092, June 1953.

[101] D. Frenkel and B. Smit. *Understanding Molecular Simulation: From Algorithms to Applications*. Academic Press, San Diego, 2001.

[102] M. M. Mariscal, J. J. Velázquez-Salazar, and M. J. Yacaman. Growth mechanism of nanoparticles: theoretical calculations and experimental results. *CrystEngComm*, 14(2):544, 2012.

[103] A. Taflove and S. C. Hagness. *Computational Electrodynamics: The Finite-Difference Time-Domain Method*. Artech House, Boston, 2000.

[104] K. F. Kelton, G. W. Lee, A. K. Gangopadhyay, R. W. Hyers, T. J. Rathz, J. R. Rogers, M. B. Robinson, and D. S. Robinson. First x-ray scattering studies on electrostatically levitated metallic liquids: Demonstrated influence of local icosahedral order on the nucleation barrier. *Phys. Rev. Lett.*, 90(19):195504, May 2003.

[105] U. Gasser, E. R. Weeks, A. Schofield, P. N. Pusey, and D. A. Weitz. Real-space imaging of nucleation and growth in colloidal crystallization. *Science*, 292(5515):258–262, 2001.

[106] N. Arkus, V. N. Manoharan, and M. P. Brenner. Minimal energy clusters of hard spheres with short range attractions. *Phys. Rev. Lett.*, 103:118303, Sep 2009.

[107] R. S. Hoy and C. S. O'Hern. Minimal energy packings and collapse of sticky tangent hard-sphere polymers. *Phys. Rev. Lett.*, 105:068001, Aug 2010.

[108] G. Meng, N. Arkus, M. P. Brenner, and V. N. Manoharan. The free-energy landscape of clusters of attractive hard spheres. *Science*, 327(5965):560–563, 2010.

[109] P. J. Yunker, K. Chen, Z. Zhang, W. G. Ellenbroek, A. J. Liu, and A. G. Yodh. Rotational and translational phonon modes in glasses composed of ellipsoidal particles. *Phys. Rev. E*, 83:011403, Jan 2011.

[110] C. M. Soto, A. Srinivasan, and B. R. Ratna. Controlled assembly of mesoscale structures using DNA as molecular bridges. *J. Am. Chem. Soc.*, 124(29):8508–8509, 2002.

[111] T. W. Melnyk, O. Knop, and W. R. Smith. Extremal arrangements of points and unit charges on a sphere: equilibrium configurations revisited. *Can. J. Chem.*, 55(10):1745–1761, 1977.

[112] J. H. Conway and N. J. A. Sloane. *Sphere Packings, Lattices and Groups*. Springer-Verlag, New York, 1993.

[113] C. L. Phillips, E. Jankowski, M. Marval, and S. C. Glotzer. Self-assembled clusters of spheres related to spherical codes. *Phys. Rev. E*, 86:041124, Oct 2012.

[114] T. Egami. Universal criterion for metallic glass formation. *Mater. Sci. Eng., A*, 226228(0):261 – 267, 1997.

[115] D. B. Miracle. A structural model for metallic glasses. *Nat. Mater.*, 3(10):697–702, October 2004.

[116] D. A. Weitz and M. Oliveria. Fractal structures formed by kinetic aggregation of aqueous gold colloids. *Phys. Rev. Lett.*, 52:1433–1436, Apr 1984.

[117] M. Y. Lin, H. M. Lindsay, D. A. Weitz, R. C. Ball, R. Klein, and P. Meakin. Universality in colloid aggregation. *Nature*, 339:360–362, 1989.

[118] D. B. Miracle, W. S. Sanders, and O. N. Senkov. The influence of efficient atomic packing on the constitution of metallic glasses. *Philos. Mag.*, 83(20):2409–2428, 2003.

[119] R. Dreyfus, M. E. Leunissen, R. Sha, A. V. Tkachenko, N. C. Seeman, D. J. Pine, and P. M. Chaikin. Simple quantitative model for the reversible association of DNA coated colloids. *Phys. Rev. Lett.*, 102(4):048301, Jan 2009.

[120] R. Dreyfus, M. E. Leunissen, R. Sha, A. Tkachenko, N. C. Seeman, D. J. Pine, and P. M. Chaikin. Aggregation-disaggregation transition of DNA-coated colloids: Experiments and theory. *Phys. Rev. E*, 81(4):041404, Apr 2010.

[121] L. A. Rosen, N. A. Seaton, and E. D. Glandt. Random sequential adsorption onto the surface of small spheres. *J. Chem. Phys.*, 85(12):7359–7363, 1986.

[122] A. Wouterse, M. Plapp, and A. P. Philipse. On the caging number of two- and three-dimensional hard spheres. *J. Chem. Phys.*, 123(054507), 2005.

[123] J. Talbot, G. Tarjus, P. R. Van Tassel, and P. Viot. From car parking to protein adsorption: an overview of sequential adsorption processes. *Colloids Surf., A*, 165(1):287–324, 2000.

[124] N. J. A. Sloane, R. H. Hardin, and W. D. Smith. *Tables of Spherical Codes*. www.research.att.com/∼njas/packings/, 2011.

[125] D. He, N. N. Ekere, and L. Cai. Computer simulation of random packing of unequal particles. *Phys. Rev. E*, 60(6):7098–7104, Dec 1999.

[126] L. A. Lyon, J. D. Debord, S. B. Debord, C. D. Jones, J. G. McGrath, and M. J. Serpe. Microgel colloidal crystals. *J. Phys. Chem. B*, 108(50):19099–19108, 2004.

[127] Y. Wang, G. Chen, M. Yang, G. Silber, S. Xing, L. H. Tan, F. Wang, Y. Feng, X. Liu, S. Li, and H. Chen. A systems approach towards the stoichiometry-controlled hetero-assembly of nanoparticles. *Nat. Commun.*, 1:87, October 2010.

[128] D. W. Brandl, N. A. Mirin, and P. Nordlander. Plasmon modes of nanosphere trimers and quadrumers. *J. Phys. Chem. B*, 110(25):12302–12310, 2006.

[129] J. A. Fan, Y. He, K. Bao, C. Wu, J. Bao, N. B. Schade, V. N. Manoharan, G. Shvets, P. Nordlander, D. R. Liu, and F. Capasso. DNA-Enabled self-assembly of plasmonic nanoclusters. *Nano Lett.*, 11(11):4859–4864, 2011.

[130] M. S. Wheeler, J. S. Aitchison, J. I. L. Chen, G. A. Ozin, and M. Mojahedi. Infrared magnetic response in a random silicon carbide micropowder. *Phys. Rev. B*, 79:073103, Feb 2009.

[131] J. A. Schuller, R. Zia, T. Taubner, and M. L. Brongersma. Dielectric metamaterials based on electric and magnetic resonances of silicon carbide particles. *Phys. Rev. Lett.*, 99:107401, Sep 2007.

[132] Y.-J. Lee, N. B. Schade, L. Sun, J. A. Fan, D. R. Bae, M. M. Mariscal, G. Lee, F. Capasso, S. Sacanna, V. N. Manoharan, and G.-R. Yi. Ultrasmooth, highly spherical monocrystalline gold particles for precision plasmonics. *ACS Nano*, 7(12):11064–11070, 2013.

[133] Y. Pang and R. Gordon. Optical trapping of a single protein. *Nano Lett.*, 12(1):402–406, 2011.

[134] J. N. Zadeh, C. D. Steenberg, J. S. Bois, B. R. Wolfe, M. B. Pierce, A. R. Khan, R. M. Dirks, and N. A. Pierce. NUPACK: analysis and design of nucleic acid systems. *J. Comput. Chem.*, 32(1):170–173, 2011.

[135] M. Zuker. Mfold web server for nucleic acid folding and hybridization prediction. *Nucleic Acids Res.*, 31(13):3406–3415, 2003.

[136] D. Sun and O. Gang. Binary heterogeneous superlattices assembled from quantum dots and gold nanoparticles with DNA. *J. Am. Chem. Soc.*, 133(14):5252–5254, 2011.

[137] D. H. Sharp. An overview of Rayleigh-Taylor instability. *Phys. D (Amsterdam, Neth.)*, 12(1):3–18, 1984.

[138] G. G. Stokes. *On the effect of the internal friction of fluids on the motion of pendulums*, volume 9. Pitt Press, 1851.

[139] M. Hoffmann, C. S. Wagner, L. Harnau, and A. Wittemann. 3D Brownian diffusion of submicron-sized particle clusters. *ACS Nano*, 3(10):3326–3334, 2009.

[140] G. L. Hunter, K. V. Edmond, M. T. Elsesser, and E. R. Weeks. Tracking rotational diffusion of colloidal clusters. *Opt. Express*, 19(18):17189–17202, 2011.

[141] K. L. Baxter-Gabbard. A simple method for the large-scale preparation of sucrose gradients. *FEBS Lett.*, 20(1):117–119, 1972.

[142] R. D. Deegan, O. Bakajin, T. F. Dupont, G. Huber, S. R. Nagel, and T. A. Witten. Capillary flow as the cause of ring stains from dried liquid drops. *Nature*, 389(6653):827–829, 1997.

[143] S. Vial, I. Pastoriza-Santos, J. Pérez-Juste, and L. M Liz-Marzán. Plasmon coupling in layer-by-layer assembled gold nanorod films. *Langmuir*, 23(8):4606–4611, 2007.

[144] B. Wang and J.-I. Anzai. Redox reactions of ferricyanide ions in layer-by-layer deposited polysaccharide films: a significant effect of the type of polycation in the films. *Langmuir*, 23(13):7378–7384, 2007.

[145] W. B. Rogers and J. C. Crocker. Direct measurements of DNA-mediated colloidal interactions and their quantitative modeling. *Proc. Nat. Acad. Sci. U. S. A.*, 108(38):15687–15692, September 2011.

[146] R. A. L. Jones. *Soft Condensed Matter*. Oxford University Press, 2002.

[147] B. Tinland, A. Pluen, J. Sturm, and G. Weill. Persistence length of single-stranded DNA. *Macromolecules*, 30(19):5763–5765, 1997.

[148] J. Fritz, E. B. Cooper, S. Gaudet, P. K. Sorger, and S. R. Manalis. Electronic detection of DNA by its intrinsic molecular charge. *Proc. Natl. Acad. Sci. U. S. A.*, 99(22):14142–14146, 2002.

[149] X. Shen, C. Song, J. Wang, D. Shi, Z. Wang, N. Liu, and B. Ding. Rolling up gold nanoparticle-dressed DNA origami into three-dimensional plasmonic chiral nanostructures. *J. Am. Chem. Soc.*, 134(1):146–149, 2011.

[150] M. Comas-Garcia, R. F. Garmann, S. W. Singaram, A. Ben-Shaul, C. M. Knobler, and W. M. Gelbart. Characterization of viral capsid protein self-assembly around short single-stranded RNA. *J. Phys. Chem. B*, 118(27):7510–7519, 2014.

[151] M. N. OBrien, M. R. Jones, K. A. Brown, and C. A. Mirkin. Universal noble metal nanoparticle seeds realized through iterative reductive growth and oxidative dissolution reactions. *J. Am. Chem. Soc.*, 136(21):7603–7606, 2014.

[152] L. Arleth, X. Xia, R. P. Hjelm, J. Wu, and Z. Hu. Volume transition and internal structures of small poly(N-isopropylacrylamide) microgels. *J. Polym. Sci., Part B: Polym. Phys.*, 43(7):849–860, 2005.

[153] D. S. Sebba, J. J. Mock, D. R. Smith, T. H. LaBean, and A. A. Lazarides. Reconfigurable core-satellite nanoassemblies as molecularly-driven plasmonic switches. *Nano Lett.*, 8(7):1803–1808, 2008.

[154] G. V. Naik, J. Kim, and A. Boltasseva. Oxides and nitrides as alternative plasmonic materials in the optical range [invited]. *Opt. Mater. Express*, 1(6):1090–1099, 2011.

[155] G. V. Naik, J. L. Schroeder, X. Ni, A. V. Kildishev, T. D. Sands, and A. Boltasseva. Titanium nitride as a plasmonic material for visible and near-infrared wavelengths. *Opt. Mater. Express*, 2(4):478–489, 2012.

[156] J. B. Khurgin and A. Boltasseva. Reflecting upon the losses in plasmonics and metamaterials. *MRS Bull.*, 37(08):768–779, 2012.

[157] A. V. Kildishev, A. Boltasseva, and V. M. Shalaev. Planar photonics with metasurfaces. *Science*, 339(6125):1232009, 2013.

[158] S. Molesky, C. J. Dewalt, and Z. Jacob. High temperature epsilon-near-zero and epsilon-near-pole metamaterial emitters for thermophotovoltaics. *Opt. Express*, 21(101):A96–A110, 2013.

[159] J. Zheng, J. J. Birktoft, Y. Chen, T. Wang, R. Sha, P. E. Constantinou, S. L. Ginell, C. Mao, and N. C. Seeman. From molecular to macroscopic via the rational design of a self-assembled 3D DNA crystal. *Nature*, 461(7260):74–77, 2009.

[160] J. J. Storhoff, R. Elghanian, C. A. Mirkin, and R. L. Letsinger. Sequence-dependent stability of DNA-modified gold nanoparticles. *Langmuir*, 18(17):6666–6670, 2002.

[161] R. Jin, G. Wu, Z. Li, C. A. Mirkin, and G. C. Schatz. What controls the melting properties of DNA-linked gold nanoparticle assemblies? *J. Am. Chem. Soc.*, 125(6):1643–1654, 2003.

[162] P. K. Jain, K. S. Lee, I. H. El-Sayed, and M. A. El-Sayed. Calculated absorption and scattering properties of gold nanoparticles of different size, shape, and composition: applications in biological imaging and biomedicine. *J. Phys. Chem. B*, 110(14):7238–7248, 2006.

[163] Z. G. Estephan, Z. Qian, D. Lee, J. C. Crocker, and S.-J. Park. Responsive multidomain free-standing films of gold nanoparticles assembled by DNA-directed layer-by-layer approach. *Nano Lett.*, 13(9):4449–4455, 2013.

[164] L. M. Demers, C. A. Mirkin, R. C. Mucic, R. A. Reynolds, R. L. Letsinger, R. Elghanian, and G. Viswanadham. A fluorescence-based method for determining the surface coverage and hybridization efficiency of thiol-capped oligonucleotides bound to gold thin films and nanoparticles. *Anal. Chem.*, 72(22):5535–5541, 2000.

[165] W. J. Parak, T. Pellegrino, C. M. Micheel, D. Gerion, S. C. Williams, and A. P. Alivisatos. Conformation of oligonucleotides attached to gold nanocrystals probed by gel electrophoresis. *Nano Lett.*, 3(1):33–36, 2003.

[166] J. I. Cutler, E. Auyeung, and C. A. Mirkin. Spherical nucleic acids. *J. Am. Chem. Soc.*, 134(3):1376–1391, 2012.

[167] J. Liu and Y. Lu. Accelerated color change of gold nanoparticles assembled by DNAzymes for simple and fast colorimetric Pb^{2+} detection. *J. Am. Chem. Soc.*, 126(39):12298–12305, 2004.